Molten chloride salt technology for next generation concentrating solar power plants: corrosive impurity monitoring and corrosion mitigation

A thesis accepted by the Faculty of Energy-, Process- and Bio-Engineering of the University of Stuttgart to fulfill the requirements for the degree of Doctor of Engineering Sciences (Dr.-Ing.)

by

Gong, Qing

born in Jiangsu China

Main referee:	Prof. Dr. André Thess
Co-referee:	Prof. Dr. Yongliang Li
Chairman of exam:	Prof. Dr. Günter Scheffknecht
Co-supervisor:	Dr. Wenjin Ding
Date of the oral exam:	22.09.2023

Institute for Building Energetics, Thermotechnology and Energy Storage (IGTE) at the University of Stuttgart

2023

Declaration

I hereby certify that this dissertation is entirely my own work except where otherwise indicated. Passages and ideas from other sources have been clearly indicated.

Stuttgart, _____ _____

Gong, Qing

Preface and Acknowledgement

My doctoral research project started during the Covid-19 pandemic, without the support of my supervisors, colleagues, and family, it would have been challenging to carry out my research. Here, I would like to express my sincere gratitude to them.

First and foremost, I would like to thank Professor André Thess for his guidance during my doctoral studies. His mentorship reminded me of the critical link between scientific research and commercialization. I would also like to express my special thanks to Professor Yongliang Li, who kindly agreed to be the co-examiner of my thesis.

I would like to extend my heartfelt gratitude to my direct supervisor at the German Aerospace Center, Dr. Wenjin Ding. As a leading figure in the field of thermal energy storage based on chloride salt, he provided me with unrestricted supervision and discussion. The majority of the scientific achievements presented in this thesis were completed through detailed discussions with him, which also reflected his dedication.

I am grateful to Dr. Thomas Bauer and Dr. Alexander Bonk for their leadership in the TSF group during the Covid-19 pandemic, which enabled me to devote all my energy to scientific research in the group of TSF.

In the laboratory, I received tremendous support from Ms. Andrea Hanke, Mr. Markus Braun, and Mr. Ralf Hoffmann. Reliable chemical analysis is impossible without Ms. Hanke's meticulous work in the chemical laboratory. Mr. Braun and Mr. Hoffmann showed me the profound skills of German engineers in test-rig design, construction, and automatic control. My main experimental platform, HaloTES, was restarted and improved with their help.

In the doctoral office, my scientific discussions with Mr. Julian Steinbrecher and Mr. Sumit Kumar were unforgettable. Although our research focuses were different, we still shared our fresh experimental results with each other and received valuable feedback. We also argued and debated due to different viewpoints, but these discussions with peers were free, open, and effective.

Throughout all of my doctoral study, my family was by my side. My parents provided me with unwavering support, and my wife (who was my girlfriend), Ms. Yinxia Zhang, overcame the pandemic lockdown and traveled all the way from China to Germany to reunite with me and get married. The encouragement of my family gave me the courage to overcome difficulties, during my doctoral research. I express my sincere gratitude to them.

Contents

Abstract

In the next generation of concentrating solar power plants (Gen3 CSP), the envisaged higher thermal-to-electrical conversion efficiency requires high operating temperatures. However, the existing nitrate-based thermal storage system (nitrate-TES) is unable to meet the demand for operating temperatures above 700 °C, limiting the thermal-to-electrical conversion efficiency to around 40%. Molten chloride salts, such as the $MgCl_2$-KCl-NaCl-system, are considered promising thermal storage media. However, despite the potential advantages of low cost, large operating range, and high abundance, corrosion has been a century-long challenge for chloride salts, hindering their further development as high-temperature thermal storage media and heat transfer fluids (HTFs). For the $MgCl_2$-KCl-NaCl salt system, the MgOHCl species, has been identified as a main corrosive impurity, which is produced by a mix of the salts hygroscopicity nature and hydrolysis reactions. The implementation of quantitative analysis and subsequent removal of corrosive impurities is crucial for effective management of metal corrosion in molten chloride salts.

In this dissertation, chemical and electrochemical methods are developed that can monitor corrosive MgOHCl-impurities at concentrations down to tens of ppm (parts per million) in molten chloride salts. At such low analytical concentrations, the acceptable impurity level of MgOHCl in molten chloride salt can be discussed for cost-effective Fe-based alloy quantitatively.

In addition, purification methods to reduce the MgOHCl impurity concentration were developed to investigate their impact on the corrosion of commercially available and economically viable structural materials. A simple and effective magnesium-based corrosion mitigation strategy was developed to be effective in reducing the MgOHCl impurity concentration to allow the use of Fe-based alloys as structural materials. This corrosion mitigation strategy has been verified in long-term tests up to 2000 hours at 700 °C and has confirmed a potential service life of > 30 years for Fe-based alloys with corrosion rates of < 15 μm/year, which was not thought possible prior to this work. This conclusion is confirmed from several perspectives, including mass loss, microstructural analysis and concentration of corrosion products in salts. Considering the allowable stress of the material, this work indicates that Fe-based alloys, represented by austenitic stainless steels, can be the main structural materials for the hot part at 700 °C of the chloride-TES system.

Moreover, the magnesium-based chloride salt mitigation strategy is used in an isothermal exposure experiment at 500 °C, confirming that ferritic-martensitic steel can also achieve a corrosion rate below 15 μm/year at this temperature. Thus, ferritic-

martensitic steel can be a candidate for the structural material of the cold part in the chloride-TES system.

The corrosion test results indicate excellent compatibility between the low-cost Fe-based alloy and purified $MgCl_2$-KCl-NaCl, even at temperatures as high as 700 °C. This compatibility makes the chloride-TES system economically competitive with existing nitrate-TES systems, and opens up the possibility for integration into next-generation power cycles, such as the supercritical CO_2 Brayton power cycle. This integration will potentially increase the thermal-to-electrical conversion efficiency of Gen-3 CSP from the current 40% to ~55%, thereby further reducing its levelized cost of electricity (LCOE).

Kurzzusammenfassung in deutscher Sprache

In der nächsten Generation von konzentrierenden Solarkraftwerken (Gen3 CSP) erfordert die angestrebte höhere Wärme-Elektrizitäts-Umwandlungseffizienz höhere Betriebstemperaturen. Das vorhandene Nitrat-basierte Wärmespeichersystem (nitrate-TES) kann jedoch den Bedarf an Betriebstemperaturen über 700 °C nicht erfüllen und begrenzt die Wärme-Elektrizitäts-Umwandlungseffizienz auf etwa 40 %. Geschmolzene Chloridsalze wie das $MgCl_2$-KCl-NaCl-System gelten als vielversprechende Wärmespeichermedien. Trotz potenzieller Vorteile wie niedriger Kosten, großer Betriebsbereich und hoher Verfügbarkeit ist Korrosion ist jedoch jeher eine Herausforderung für Chloridsalze, die ihre weitere Entwicklung als Hochtemperatur-Wärmespeichermedium und Wärmeträgerfluid bisher behindert. Für das $MgCl_2$-KCl-NaCl-Salzsystem ist die kritischste korrosive Verunreinigung ein Hydroxychlorid (MgOHCl), welches durch hygroskopische Eigenschaften und Hydrolyse-Reaktionen des Salzes entsteht. Eine quantitative Analyse der korrosiven Verunreinigungen in Chloridsalzen ist ein entscheidender Weg zur Erkennung und Minimierung von möglichen Korrosionsreaktionen.

In dieser Dissertation werden chemische und elektrochemische Methoden zur Bestimmung von MgOHCl-Verunreinigungen in Konzentrationen im nahezu einstelligen ppm-Bereich entwickelt und untersucht. Bei solch niedrigen analytischen Konzentrationen kann das akzeptable Verunreinigungsniveau von MgOHCl in geschmolzenen Chloridsalzen quantitativ diskutiert werden, um eine kosteneffektive Fe-basierte Legierung zu erreichen.

Darüber hinaus wird eine Methode zur Reduzierung des Verunreinigungsgrades untersucht, um die Konzentration von MgOHCl zu senken, und damit die Korrosivität der Salz-schmelze zu minimieren. Es wurde eine einfache und effektive Korrosionsminderungsstrategie auf Magnesiumbasis entwickelt, um die MgOHCl-Verunreinigungskonzentration zu reduzieren und damit den Einsatz von Fe-basierten Legierungen als Strukturwerkstoffe zu ermöglichen. Diese Korrosionsminderungsstrategie wurde in Langzeittests bis zu 2000 Stunden bei 700 °C verifiziert und bestätigte eine potenzielle Lebensdauer von >30 Jahren für Fe-Legierungen mit Korrosionsraten von <15 µm/Jahr, was vor dieser Arbeit nicht für möglich gehalten wurde. Diese Schlussfolgerung wird aus verschiedenen Blickwinkeln bestätigt, einschließlich Massenverlust, Mikrostrukturanalyse und Konzentration von Korrosionsprodukten in Salzen. Unter Berücksichtigung der zulässigen Materialbeanspruchung zeigt diese Arbeit, dass Fe-Legierungen, repräsentiert durch austenitische Edelstähle, die Hauptstrukturwerkstoffe für den heißen Teil bei 700 °C des Chlorid-TES-Systems sein können.

Zusätzlich wurde die Mg-basierte Chloridsalzreinigungsmethode in einem isothermen Expositionsexperiment bei 500 °C eingesetzt und bestätigt, dass ferritisch-martensitischer Stahl auch bei dieser Temperatur eine Korrosionsrate von weniger als 15 μm/Jahr erreichen kann. Ferritisch-martensitischer Stahl ist daher ein Kandidat für den Strukturwerkstoff des kalten Teils im Chlorid-TES-System.

Die Ergebnisse der Korrosionstests zeigen eine ausgezeichnete Kompatibilität zwischen der kostengünstigen Fe-basierten Legierung und dem gereinigten MgCl2-KCl-NaCl, selbst bei Temperaturen bis zu 700 °C. Diese Kompatibilität macht das Chlorid-TES-System wirtschaftlich konkurrenzfähig zu bestehenden Nitrat-TES-Systemen und eröffnet die Möglichkeit der Integration in fortschrittlicheren Stromkreisläufen (z.B. sCO_2 Brayton-Cycle). Diese Integration könnte der thermisch-zu-elektrische Wirkungsgrad von 40% auf ~55% durch erhöht werden, was die Stromgestehungskosten (LCOE) reduziert und die Wettbewerbsfähigkeit von Solarkraftwerken signifikant erhöht.

Nomenclature

A	Surface area of metal samples	cm^2
$A_{chloride}$	Cost of alloy used in chloride-TES	USD
$A_{nitrate}$	Cost of alloy used in nitrate-TES	USD
$C_{chloride}$	Unit cost of chloride salt	USD/kg
$C_{chloride}$	Cost of the chloride salt inventory	USD
$C_{chloride\ tank}$	Cost of chloride tank	USD
$C_{nitrate\ tank}$	Cost of nitrate tank	USD
c_p	Heat capacity of molten salt	kJ/(°C·kg)
F_1	Volume factor	-
F_2	Cost factor of alloy	-
F_3	Stress factor	-
K	Factor to calculate corrosion rate with mass loss method: 8.76×10^7	$\mu m \cdot h \cdot cm^{-1} \cdot year^{-1}$
k_1	Factor to calculate corrosion rate with micro-analysis method: 8760	h/year
k_2	Factor to convert energy unit: 2.78×10^{-7}	MWh/kJ
m	Mass of the molten salt involved in two tanks	kg
Q	Heat storage capacity	MWh_{-th}
$S_{chloride}$	Maximum allow stress of alloy used in chloride-TES	MPa

S_{corr}	Thickness of the corrosion layer of the exposed alloy samples	μm
$S_{nitrate}$	Maximum allow stress of alloy used in chloride-TES	MPa
t	Immersion time	h
$V_{chloride}$	Volume of chloride salt	m^3
$V_{nitrate}$	Volume of nitrate salt	m^3
W	Mass loss of metal samples	g
ΔT	Temperature difference between cold and hot tank	°C
ϱ	Density of metal samples	g/cm^3

AAS	Atomic absorption spectroscopy
ASME	American Society of Mechanical Engineers
ASTM	American Society for Testing and Materials
CAPEX	Capital expenditure
CAS	Chinese Academic of Sciences
Chloride-TES	Thermal energy storage based on molten chloride salt medium
CR	Corrosion rate
CSP	Concentrating solar power plants
CV	Cyclic voltammetry
DOE	The US Department of Energy
EDX	Energy-dispersive X-ray spectroscopy

EN	European Standard
HTF	Heat transfer fluid
IRENA	International Renewable Energy Agency
LCOE	Levelized Cost of Electricity
MSR	Molten salt reactor
nitrate-TES	Thermal energy storage based on molten nitrate salt medium
NREL	US National Renewable Energy Laboratory
RSD	Relative standard deviation
sCO_2	Supercritical carbon-dioxide
SEM	Scanning electron microscopy
TES	Thermal energy storage
USD	US dollar
μm	Micrometer
GW_{el}	Gigawatt of electricity
mol.%	Molar percentage
MWh-th	Megawatt hour of heat
ppm O	parts per million oxygen
USD/kWh$_{-th}$	US dollar per kilowatt hour of heat
wt.%	Weight percentage

Al_2O_3	Aluminum oxide

Ar	Argon
Cl_2	Chlorine
Cr	Chromium
Cr^{2+}	Chromous ion
Cr^{3+}	Chromic ion
$CrCl_2$	Dichlorochromium
$CrCl_3$	Chromic trichloride
e^-	Electron
Fe	Iron
H^+	Hydrogen ion
H_2	Hydrogen
H_2O	Dihydrogen oxide
HCl	Hydrogen chloride
K_2CO_3	Dipotassium carbonate
KCl	Potassium chloride
KNO_3	Potassium nitrate
Li_2CO_3	Dilithium carbonate
Mg^{2+}	Magnesium ion
$MgCl_2$	Magnesium chloride
$MgCl_2 \cdot 6H_2O$	Magnesium dichloride hexahydrate
$MgCr_2O_4$	Dichromium magnesium tetraoxide
MgO	Magnesium oxide

$MgOH^+$	Magnesium hydroxide ion
MgOHCl	Magnesium chloride hydroxide
Na_2CO_3	Sodium carbonate
NaCl	Sodium chloride
$NaNO_3$	Sodium nitrate
Ni	Nickel
O_2	Oxygen

1 Introduction

This dissertation will focus on the most challenging issues of corrosion in the high-temperature molten chloride salt technology for next-generation concentrating solar power (CSP) plants.

The molten-salt based thermal energy storage (TES) is a significant system in the CSP plants, allowing the flexible and continuous electricity generation from intermittent solar energy [1,2]. In state-of-the-art commercial CSP plants, the TES system with $NaNO_3$-KNO_3 (60-40 wt.%) mixture (called Solar Salt) operates at temperatures of < 565 °C, which limited by the thermal decomposition of the nitrate ion at high temperatures [1,3-5]. In the next-generation CSP, the TES system with ≥ 700 °C operating temperature and the advanced power cycle, such as the supercritical carbon-dioxide (sCO_2) Brayton cycle, are required to increase the thermoelectric conversion efficiency to > 50% and reduce the levelized-cost-of-electricity (LCOE) [1,2]. In the Section 1.1, an overview of commercial and next-generation molten salt TES will be summarized.

The molten chloride salt is a promising TES medium and heat transfer fluid (HTF) for next-generation CSP, due to excellent thermophysical properties and low material costs [1,2,6]. In addition to the CSP, the molten chloride salt technology can be used extensively in Carnot Battery [7], industrial thermal management [3], and molten salt reactor [8-10], where high temperature TES/HTF are required. The $MgCl_2$-NaCl-KCl mixture (47.1-30.2-22.7 mol.%, 56.5-22.2-21.3 wt.%) is a selected mixture with the advantages of low melting point (~383 °C), high thermal stability (stable at > 800 °C), low vapor pressure (~1 kPa at 800 °C), and low cost (~0.22 USD/kg) [11]. However, the corrosion issue is a primary impediment to the application of molten chloride salts, including the $MgCl_2$-NaCl-KCl mixture [1,2,12]. Without corrosion mitigation strategies, the molten $MgCl_2$-NaCl-KCl mixture has been reported to cause a corrosion rate (CR) of 1752 µm/year on stainless steel 310 (SS 310) at 700 °C under argon atmosphere in previous work of German Aerospace Center (DLR) [13]. This CR is far from the standard of < 15 µm/year, which is required for a 30-year life-time of the CSP/TES system [14]. Since as early as the 1950s, the corrosion issues of molten chloride salts plagued researchers developing nuclear molten salt reactors (MSRs)

[15,16]. In recent years, molten chloride salt corrosion has received renewed attention with the launch of the Gen-3 CSP projects by the US Department of Energy (DOE) [1,2]. To solve the problem of corrosion, the corrosion mechanism of molten chloride salt should be investigated and understood. Only with a comprehensive understanding of the corrosion mechanisms, affective anti-corrosion strategies can be proposed. Hence, a systematic overview on the corrosion in molten chloride is presented in the Section 1.2.

Corrosion issues are often relegated to the issue of compatibility between molten chloride salt and structural materials. Thus, both the attacking molten salt medium with its impurity and the attacked structural material must be considered. In addition to the corrosion issues, mechanical properties and costs should also be considered when choosing structural materials. For instance, the oxide based ceramics such as alumina (Al_2O_3) show good compatibility with the molten chloride salts at high temperatures [17], but the poor fracture toughness limits the machining of this material as a complex component. Furthermore, the unit cost of structural materials should be considered when designing molten salt tanks that require significant amounts of material to manufacture tanks containing 10 to 100 thousand tons of molten chloride salt in a commercial CSP plant. The corrosion issues, mechanical properties, and the cost of structural materials should be comprehensively considered, leading to the trilemma of material selection for molten chloride salt TES, as summarized in the Section 1.3.

In order to overcome the trilemma, a comprehensive corrosion mitigation methodology is proposed and investigated in this dissertation. With such corrosion mitigation methodology, the low-cost commercial steel with excellent mechanical properties can be selected as the structural materials of chloride-TES, thus effectively overcoming the trilemma.

1.1 Molten salt thermal energy storage

According to a report published by the International Renewable Energy Agency (IRENA) at 2020 [18], the low-cost TES integrated in CSP is one of the only low-cost, long-duration, and large-scale energy storage solutions available, along with pumped hydro storage. By the end of 2019, the global power generation capacity of CSP plants with molten salt storage amounted to 21 GWh_{el} [3]. Incorporating TES into CSP has proven to be an effective method for stabilizing the grid and reducing electricity abandonment.

A previous report on the SunShot initiative by the Department of Energy (DOE) in the US [19] emphasized that CSP with 6 hours of TES could play a critical role in

stabilizing the grid, by generating approximately 1% of total electricity but reducing marginal electricity curtailment from 30% to ~10%. This percentage of curtailment reduction could be further reduced by incorporating higher amounts of TES [19]. Recently, the application of cost-effective molten salt TES in a hybrid power plant with CSP, PV and/or wind energy (e.g., in Mohammed bin Rashid Al Maktoum Solar Park, Dubai [18]) was reported. In 2022, about 30 CSP plants (approx. 3 GW_{el} in total) have been announced to be built in China together with photovoltaic and wind energy [20].

During the operation of GW-level energy storage, the molten salt TES has demonstrated the following major advantages, comparing with other running or potential long-duration and large-scale energy storage solutions.

- **Low cost and long service life**. Molten salt TES has a capital cost as low as 20-33 USD/kWh_{-th} with a designed service life of 30 years, making it a cost-effective and long-term solution for energy storage that is easily scalable into the GWh-capacity range [1,21].
- **Safety**. Molten salt TES systems are considered safe due to the low toxicity and non-flammable nature of the salt [3]. In the event of a catastrophic accident, there is no risk of the accident escalating to a larger scale, such as flaming and explosion.
- **Low system complexity**. In the CSP, the molten salt system is used as both TES and HTF medium. This advantage reduces the number of heat exchanges, increasing the overall efficiency of the system [22].

In the following sections, the commercial and next generation molten salt TES will be introduced, providing a comprehensive understanding of commercial molten salt TES and insights into the motivation and directions of next generation molten salt TES.

1.1.1 Commercial molten nitrate salt thermal energy storage

The parameters of commercial molten nitrate TES are significant references for next-generation CSP, including the main structural materials of tanks, operating temperature, cost breakdown, and properties of molten salt. In the report published by the US National Renewable Energy Laboratory (NREL) [1], there is a case study of commercial TES with nitrate salt (nitrate-TES) based on the Abengoa project for a tower CSP plant, where the costs breakdown and some key parameters are available, as summarized in the Table 1. For a nitrate-TES with 2703 MWh_{-th}, the total capital expenditure (CAPEX) is about 53 million US dollar (USD), i.e., 20 USD/kWh_{-th}. In this report [1], as can be known from the Table 1, three key parts account for 84% of total cost: hot tank (19%), cold tank (8%), and nitrate salt (57%).

The salt mixture used in commercial TES systems is Solar Salt ($NaNO_3$-KNO_3 60-40 wt.%) with a maximum operating temperature of 565 °C. The unit material cost of such nitrate salt mixture is about 1.1 USD/kg, according to the cost available in ref. [1] published in 2017. For a 100 MW CSP plant with 10-hour TES storage, the mass of salt required is about 27,000 tons. The main structural material of the hot tank is SS 347, while that of the cold tank is ASTM A 516 Grade 70 carbon steel. The structural materials have a maximum allowable stress of about 115 MPa at their serving temperatures, which is available in the ASME Boiler and Pressure Vessel Code 2010 [23].

Table 1. A case study on commercial nitrate salt TES, the data are summarized from Ref. [1].

	Material	**Price USD thousands**	**TES cost USD/kWh-th**	**Percentage %**
Hot tank	SS 347	10 016	3.71	19
Cold tank	ASTM A 516 70	4361	1.61	8
Salt inventory	$NaNO_3$-KNO_3 (60-40 wt.%)	30 122	11.14	57
Structural steel	-	666	0.25	1
Tank insulation	-	3 724	1.38	7
Electrical	-	481	0.18	1
Foundations	-	3 050	1.13	6
Site work	-	347	0.13	1
Total		52 767	20	100

1.1.2 Next generation molten salt thermal energy storage

As shown in **Fig. 1** [24], the thermal-to-electrical efficiency in next-generation CSP can be increased to over 50% by operating at temperatures of ≥ 700 °C and combining with e.g., the sCO_2 power cycle. Molten chloride and molten carbonate have been selected by DOE as TES/HTF candidates for next-generation CSP due to their higher thermal stability compared to commercial nitrate salts [1].

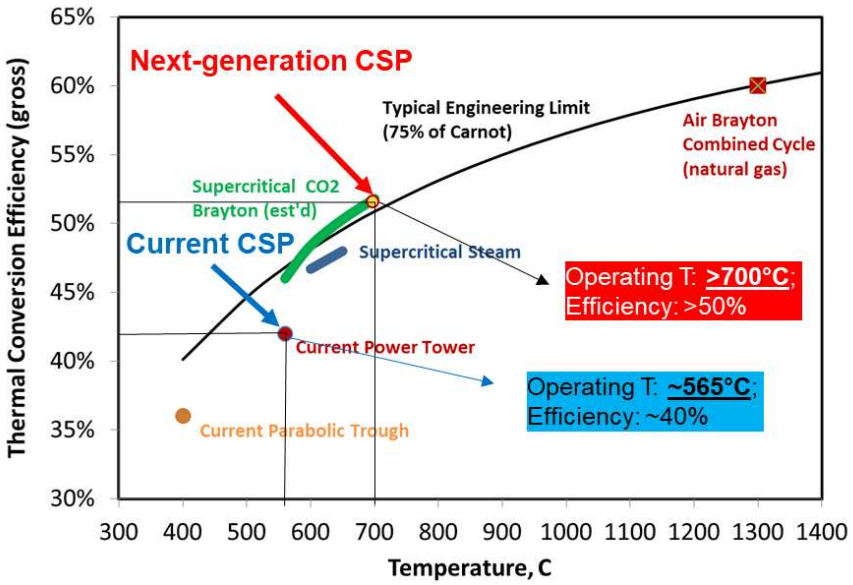

Fig. 1. The relationship between thermal conversion efficiency and operating temperature with different power cycles. The plot is adapted from Ref [24].

In addition to the thermal stability, some properties (melting point, max. working temperature, density, heat capacity, and viscosity) of molten nitrate, chloride, and carbonate are summarized in Table 2 based on the literature [1,2,5,11,25]. Besides the properties of molten salt, the price is a significant parameter for the selection of next generation molten salt for TES. As summarized in Table 2, the $MgCl_2$-KCl-NaCl has the lowest price which is about one-tenth that of Li_2CO_3-Na_2CO_3-K_2CO_3 and one-third of $NaNO_3$-KNO_3, with a cost of around 0.22 USD/kg [25].

Table 2. Selected concerned properties of typically considered molten nitrate, chloride and carbonate salt mixture [1,2,5,11,25].

Molten salt (wt.%)	**$NaNO_3$-KNO_3 (60-40)**	**$MgCl_2$-NaCl-KCl (56.5-22.2-21.3)**	**Li_2CO_3-Na_2CO_3-K_2CO_3 (32.1-33.4-34.5)**
Melting point (°C)	240	383	397
Maximum working temperature (°C)	565	>800	800
Density (g/cm³)	1.8 (400 °C)	~1.7 (600 °C)	2 (600 °C)
Heat capacity (kJ/(kg·K))	1.5 (400 °C)	1.14 (600 °C)	1.8 (600 °C)
Unit price (USD/kg)	0.8-1.1	0.22-0.35	2.5-3

Viscosity (mPa s)	1.03	~3.2 (600 °C)	10.7 (600 °C)

The cost breakdown of each component of TES systems reported in [1] is presented in **Fig. 2**. For carbonate-TES, the cost of K_2CO_3-Li_2CO_3-Na_2CO_3 salt is over 30 USD/kWh, which is higher than the cost of the entire nitrate-TES system. This is primarily due to the high cost of Li_2CO_3. In contrast, the cost of the $MgCl_2$-KCl salt in chloride-TES is lower than that of nitrate and carbonate TES. The ternary system of $MgCl_2$-KCl-NaCl demonstrates even lower cost than the binary $MgCl_2$-KCl mixture since NaCl is the cheapest salt in the $MgCl_2$-KCl-NaCl system [11]. However, the cost of the hot and cold tanks in chloride-TES is significantly higher than that in nitrate-TES, mainly due to the selection of nickel-based alloy Haynes 230 and stainless steel 347 as the primary structural materials for the hot and cold tanks, respectively [1]. This material selection strategy is primarily driven by the high corrosiveness of molten chloride salt. In general, higher Ni content in Fe-Cr-Ni alloys translates to better corrosion resistance but also a higher unit cost. Alloys with >60 wt.% Ni content can be up to ten times more expensive than stainless steel with 10-30 wt.% Ni [26], while stainless steel is typically more expensive than low alloy steel and carbon steel. Therefore, if the compatibility issues between molten chloride salt and structural materials, especially corrosion, can be addressed, the cost of chloride-TES can be reduced to a similar or even lower level than nitrate-TES.

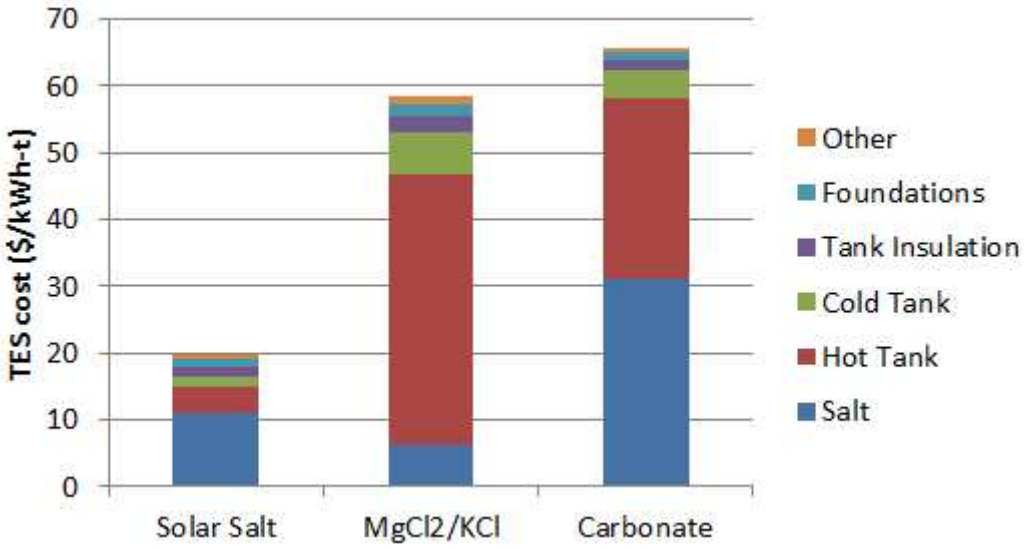

Fig. 2. Breakdown of TES costs with different molten salts [1].

Once corrosion issues with molten chloride salt are resolved, the next-generation CSP plant could benefit from using an advanced power cycle (such as sCO_2 Brayton) at higher operating temperatures, resulting in significantly higher energy conversion

efficiency and lower Levelized Cost of Electricity (LCOE) than current commercial CSP plants. In the next section 1.2, the critical corrosion issues related to molten chloride salt and structural materials will be systematically introduced.

1.2 Corrosion of molten chloride salt

For the application in the next-generation CSP with thousand-ton scale, the $MgCl_2$-NaCl-KCl is recommended as one of the most promising compositions, with the advantages of cost-effective (~0.22 USD/kg [1,25]), low-melting-point (~383 °C [11,27]) high thermal stability (stable above 800 °C [6,11]) and low vapor pressure (~1kPa at 800 °C [11]) [6,11,28]. Some of the concerned properties can be found in the Table 2. In this dissertation, the corrosion investigation is based on the mixtures of $MgCl_2$-KCl-NaCl (47.1–30.2–22.7 mol.%, 56.5–22.2–21.3 wt.%) for a focused exploration, according to the previous study [11,27].

Since the corrosion of molten chloride salt has been a long-standing problem, there are numerous references available, including summarizing of corrosion rate at different temperature [6,10,12,13,16,29-36], exploration of corrosion mechanism[8,13,16,37-43], and proposing of corrosion strategies [8,16,31,44-46]. However, there are clear research gaps for large-scale (ten-thousand scale) and long-lifetime (up to 30 years) application of molten chloride salt technology due to the corrosivity. The following sections provide an overview of the corrosion issues and identify the research gaps around which the research covered in this thesis revolves.

1.2.1 Corrosion rate of Fe-Cr-Ni alloy in molten chloride salt

The corrosion rate (CR) of an alloy in a corrosive environment can be quantitatively evaluated in micrometers per year (μm/year). Two primary methods can be used to measure the CR of steel in molten salt.

The first approach for measuring CR involves comparing the mass of alloy samples before and after exposure tests, as shown in Eq. 1 [47].

$$CR\ (\mu m/year) = \frac{K \times W}{A \times t \times \rho} \qquad \text{Eq. 1}$$

where,

K is a constant 8.76×10^7 in $\mu m \cdot h \cdot cm^{-1} \cdot year^{-1}$;

W is the mass loss of samples in g;

A is the sample's surface area in cm^2,

t is immersion time in hour;

ρ is the density of samples in g/cm^3.

Another approach for measuring the CR is through microanalysis. After the immersion test of an alloy in the molten salt, the cross-section of the alloy samples can be analyzed using scanning electron microscopy (SEM), typically coupled with energy-dispersive X-ray spectroscopy (EDX) methods. By considering the immersion time and thickness of the corrosion layer, the CR can be calculated using Eq. 2.

$$CR\ (\mu m/year) = S_{corr} \times \frac{k_1}{t} \qquad \text{Eq. 2}$$

where,

S_{corr} is the thickness of the corrosion layer of the exposed alloy samples in μm;

t is the immersion time in hour (h).

k_1 is a constant indication 8760 hours per year (h/year).

The targeted corrosion rate for structural materials used in CSP plants is to be < 15 μm/year for a 30-year lifespan [14]. Achieving this target is considered extremely ambitious.

Some representative CRs of typical materials in chloride salt are summarized in the Table 3. According to available literature [6,35,48,49], Fe-Cr-Ni alloys in molten chloride exhibit CRs > 1000 μm/year at temperatures ≥ 700 °C, even in inert atmospheres. For example, Ding et al. reported that at 700 °C, SS 310, In 800H, and C-276 had CRs of approximately 1752, 876, and 526 μm/year, respectively, in molten $MgCl_2$-KCl-NaCl salt, as determined by microanalysis [13]. Zhao et al. found that the CR of the nickel-based alloy Haynes 230 was > 3200 μm/year in molten $MgCl_2$-KCl salt at 800 °C, based on mass-loss analysis [6,48]. In this experiment, the furnace vessel made of Ni was damaged by the untreated molten chloride salt [48]. In other words, even expensive nickel-based alloys cannot achieve a CR target of < 15 μm/year at ≥ 700 °C without corrosion mitigation strategies.

Table 3. Representative data from molten chloride salt corrosion experiments.

Molten salt (mol. %)	Temper-ature °C	Material (Ni wt.%)	Atmos-phere	Test time h	CRs µm/year	Ref.
$MgCl_2$-KCl-NaCl (45.5-21.5-33)	500	SS 347 (9-12)	Vacuum	1000	~120	[12,35]
$MgCl_2$-KCl-NaCl (45.5-21.5-33)	500	SS 316 (10-14)	Vacuum	1000	~10	[12,35]
$MgCl_2$-KCl-NaCl (45.5-21.5-33)	500	Ha N (~71)	Vacuum	1000	50	[12,35]
$MgCl_2$-KCl-NaCl (60-20-20)	700	SS 310 (19-22)	Argon	500	1752	[13]
$MgCl_2$-KCl-NaCl (60-20-20)	700	In 800H (30.52)	Argon	500	876	[13]
$MgCl_2$-KCl-NaCl (60-20-20)	700	C 276 (~60)	Argon	500	526	[13]
$MgCl_2$-KCl (50-50)	800	Ha 230 (~60)	Nitrogen	100	>3200	[6,48]

To address the issue of strong corrosivity, it is necessary to systematically understand the corrosion mechanism of molten chloride salt (see Section 1.2.2). Based on this understanding, effective corrosion mitigation strategies can be developed (see Section 1.2.3).

1.2.2 Corrosion mechanism and MgOHCl measurement

One positive aspect is that pure $MgCl_2$-KCl-NaCl mixtures are theoretically non-corrosive to Fe-Cr-Ni alloys at high temperatures. Zhang et al. determined through redox potential research that pure $MgCl_2$-KCl-NaCl mixture do not cause corrosion to Ni and Cr metals [38]. This conclusion can be extended to most Fe-Cr-Ni alloys since Fe metal activity is lower than Cr.

It is well accepted that the corrosion of Fe-Cr-Ni alloys in molten $MgCl_2$-KCl-NaCl is primarily driven by the presence of corrosive impurities with high redox potentials [13,32,33,48]. The high hygroscopicity of molten chloride salt leads to the adsorption of moisture from the air and the formation of crystalline hydrates, such as $MgCl_2 \cdot xH_2O$

(where x = 1 to 6), which can subsequently generate the corrosive impurity MgOHCl through hydrolysis [50-53].

The reactions of $MgCl_2 \cdot xH_2O$ during heating, including dehydration and hydrolysis, have been studied intensively in the magnesium electrolytic production process [50,51,53,54]. It has been shown, as indicated by Eq. 3 and Eq. 4 [50,51], that at temperatures ranging from 240 to 400 °C, the hydrolysis reaction occurs simultaneously with dehydration, producing the corrosive MgOHCl and HCl in the molten chloride salt. In addition to the heating process, the presence of H_2O impurities in the inert gas phase during the operation of chloride-TES at 420 °C to 800 °C can also increase the concentrations of MgOHCl and HCl, leading to the high corrosiveness of molten $MgCl_2$-KCl-NaCl.

$$MgCl_2 \cdot 6H_2O_{(s/l)} \rightarrow MgCl_{2\,(s/l)} + 6H_2O_{(g)} \qquad \text{Eq. 3}$$

(Dehydration at temeprature from 117 to 400 °C)

$$MgCl_2 \cdot H_2O_{(s/l)} \rightarrow MgOHCl_{(s/l)} + HCl_{(g)} \qquad \text{Eq. 4}$$

(Hydrolysis at temperature of > 240 °C)

Ding et al. constructed the corrosion mechanism of $MgCl_2$-KCl-NaCl to Fe-Cr-Ni alloy and pointed out that the MgOHCl is the main corrosive impurities in this molten salt system, due to its high solubility in molten chloride salt, high redox potential to Fe-Cr-Ni alloy, and relatively high thermal stability [13,31,45,52]. As shown in **Fig. 3**, the dissolved corrosive MgOHCl impurity in molten chloride salt can react with Cr or other metals in structural materials, resulting in the continuous corrosion of Fe-Cr-Ni alloy. This corrosion mechanism is widely accepted by molten chloride salt community and has been validated in other laboratories [6,8,33,37,40,46,55].

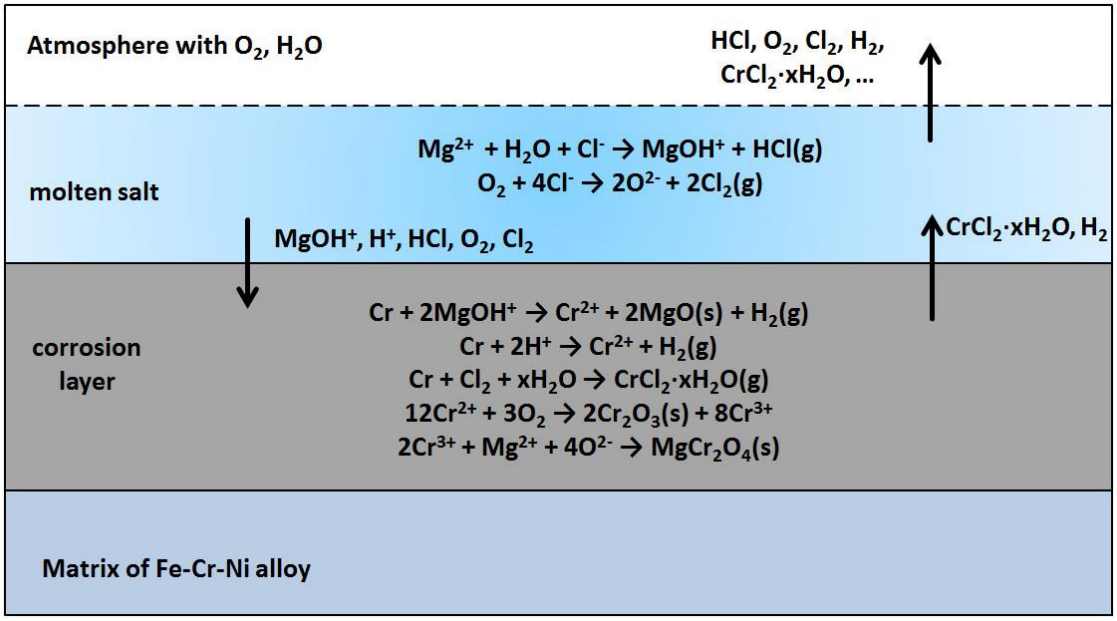

Fig. 3. Schematic diagram of the corrosion mechanism of Fe-Ni-Cr based alloys in molten $MgCl_2$-KCl-NaCl under inert atmosphere [13,31].

It is believed that there are acceptable concentrations of MgOHCl for Fe-Cr-Ni alloys with different nickel contents at a constant temperature condition (e.g., 700 °C) to achieve a CR target of 15 μm/year [6,13,31]. However, the quantitative measurement of the concentration of MgOHCl in molten chloride samples is a challenging task that involves two main aspects.

Firstly, Fe-based alloys, such as stainless steel, are less expensive than nickel-based alloys but have a lower acceptable concentration of MgOHCl at high temperatures of $\geqslant$ 700 °C [31,32]. To establish a quantitative relationship between MgOHCl concentration and the CR of Fe-Cr-Ni alloys, the concentration of MgOHCl needs to be measured at the level of tens of ppm [31,32].

Secondly, the non-corrosive MgO and the corrosive MgOHCl are often coexist in the molten chloride salt at high temperatures, as shown in Eq. 5 [50,56]. Due to their similar physicochemical properties and significantly low concentrations, it is difficult to obtain accurate concentration of the corrosive impurity MgOHCl.

$$MgOHCl_{(s/l)} \rightarrow MgO_{(s)} + HCl_{(g)} \quad (> 555\ °C) \qquad \text{Eq. 5}$$

Klammer et al. used water and methanol to extract MgOHCl and MgO based on the solubility difference, which can separately measure the concentration of MgOHCl

down to 0.1 wt.% (~1000 ppm) by a typical ethylenediaminetetraacetic acid (EDTA) titration [55]. However, this method showed a large standard deviation of ~40% at the measurement limit of 0.1 wt.% in the following MgOHCl measurement study [46].

In addition to the measurement based on chemical analysis, MgOHCl can be measured in-situ using electrochemical method, such as cyclic voltammetry (CV) [45,52,53,57]. As illustrated in **Fig. 4**, Ding et al. reported that the current density of peak B (as shown in **Fig. 4** (a)) is linearly related to the concentration of MgOHCl at a fixed temperature [45,52]. Therefore, the slope of the proportional function between the concentration of MgOHCl measured by titration and the current density of peak B can be calculated, as shown in **Fig. 4** (b). In practice, the electrical signal obtained from CV is sufficient to determine the concentration of MgOHCl, enabling in-situ measurement of this impurity. However, measurements based on electrochemical methods should be calibrated and validated by the results of chemical analysis such as titration. In other words, a more accurate chemical and ex-situ measurement of MgOHCl is the prerequisite of the electrochemical and in-situ measurement.

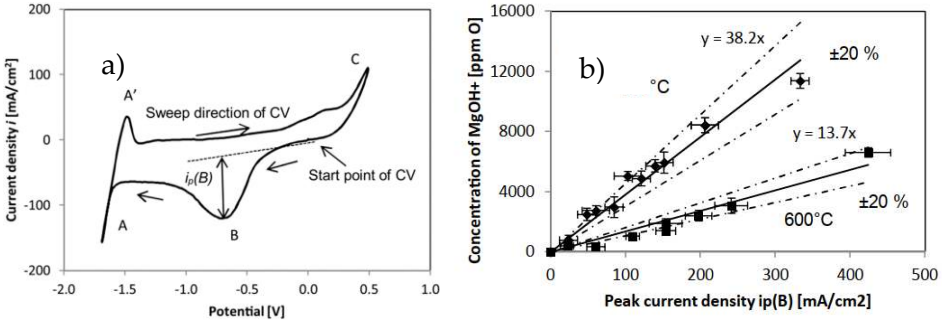

Fig. 4. a) Cyclic voltammogram in the $MgCl_2$-KCl-NaCl at 500 °C obtained by tungsten working electrode. Peak B is the feature peak for the concentration of MgOHCl in molten chloride salt b) The linear relationship between concentration of MgOHCl and current density of peak B.

1.2.3 Corrosion control strategy and salt purification

Typically, the mitigation of high-temperature corrosion in molten chloride salts involves two fundamental aspects: optimization of the structural materials and reduction of molten salt corrosivity. Optimization of structural materials encompasses a diverse range of methods, including metallic coatings [58,59] and pre-oxidation techniques [31,60] as well as the use of non-metallic materials with excellent corrosion resistance such as oxide ceramics [17], composite materials [61], and insulating firebrick [49,62]. However, thermal shock concerns may arise with coating and pre-oxidation techniques. Furthermore, non-metallic structural materials, such as oxide

ceramics, often exhibit inferior fracture toughness and/or intricate shape limitations when compared to metallic materials. Hence, based on the impurity-driven corrosion mechanism of molten chloride salt to Fe-Cr-Ni alloys, the corrosive impurity MgOHCl should be strictly monitored and suppressed.

Several different methods have been investigated to reduce the corrosive impurity in molten chloride salts. These methods include electrochemical techniques [44,63,64], thermal approaches[6,13,46,48], the addition of active metals (such as Mg) [10,16,31,36,46,48,49,65-67], carbochlorination [10,32,68], and chlorination processes [10,69].

Kashani-Nejad et al. investigated the thermal decomposition of MgOHCl by thermal gravimetric analysis (TGA) [50,56]. It shows that the corrosive MgOHCl decomposes to MgO and HCl at the temperature of > 555 °C, as shown in Eq. 5. The MgO is non-corrosive to the Fe-Cr-Ni alloys while the HCl has limited solubility in the molten chloride salt [12,70]. However, the thermal decomposition of MgOHCl is relatively slow. According to the investigation by Zhao et al. in the National Renewable Energy Laboratory (NREL) [48], the Ha 230 nickel-based alloy shows a CR of about 953 μm/year at 800 °C in the $MgCl_2$-KCl treated by thermal purification. Compared to the CR of > 3200 μm/year in untreated chloride salt [48], the CR of 953 μm/year is significantly reduced, but it is still far from the target of 15 μm/year.

Some chemical methods have been developed to purify the molten chloride salt in depth. Kurley et al. from the Oak Ridge National Laboratory (ORNL) reported a purification method of carbochlorination [32,68]. Approximately600 g $MgCl_2$-KCl salt was purified by sparging with CCl_4 gas at 850 °C for over 100 hours. Samples of SS 316L and Alloy N (a type of nickel-based alloy) samples were then exposed to the purified salt at 700 °C for 100 hours. The exposure results show that the stainless steel and the nickel-based alloy have comparable CRs of ~ 18 μm/year in the purified molten $MgCl_2$-KCl salt at 700 °C. However, due to its high cost and toxicity, the CCl_4-sparging purification method may be a challenge for large-scale purification.

Another method of chemical purification is Mg-additive, which is regarded as a low-cost, low-complexity, and effective method of treating large-scale molten chloride salt [10,46,49]. The reaction between Mg and MgOHCl is shown in Eq. 6. The Mg metal can reduce the MgOHCl to non-corrosive MgO and H_2, while itself is oxidized to $MgCl_2$.

$$Mg_{(s/l)} + 2MgOHCl_{(l)} \rightarrow MgCl_{2\,(l)} + 2MgO_{(s)} + H_{2(g)} \qquad \text{Eq. 6}$$

Zhao et al. added 0.75 wt.% Mg in molten $MgCl_2$-KCl-NaCl at 650 °C for 3 hours, reducing the concentration of MgOHCl from ~0.9 wt.% to ~0.3 wt.% [6,46,48]. The following exposure experiment of Ha 230 samples in purified salt shows that this nickel-based alloy has ~27 μm/year CR at 800 °C, which is much better than that in non-treated salt (> 3200 μm/year) and thermally treated salt (953 μm/year).

Some studies have also been carried out on the compatibility of Mg-purified chloride salts with Fe-based alloys (e.g., stainless steel) [31,66]. Ding et al. from DLR mixed 1 wt.% Mg, $MgCl_2$-KCl-NaCl, and metal samples in a crucible and heated it to 700 °C. After 500 hours, the immersed samples of SS 310, In 800H, and C-276 were obtained analysis by mass loss and SEM-EDX. According to the SEM-EDX analysis, the CRs of SS 310, In 800H, and C-276 are 298, 262, and 29.8 μm/year, respectively. Although the CR of the nickel-based alloy C-276 is close to the target of 15 μm/year, the CRs of the Fe-based alloys (SS 310 and In 800H) are still far from the target.

Ren et al. in the Chinese Academic of Sciences (CAS) purified the molten $MgCl_2$-KCl-NaCl with a Mg rod at 600 °C for 24 hours [66]. After the pre-treatment, standard SS 316 and carburized SS 316 samples were immersed in purified salt containing 1 wt.% Mg at 700 °C for 400 hours. The mass loss results indicate that the CRs of samples is ~ 51 μm/year, but the cross-section analyzed by SEM shows that the corrosion depths of the samples are 20 – 40 μm, i.e., the CRs based on microstructural analysis are 350 – 700 μm/year.

The above examples show that chemical purification methods, such as the addition of Mg, can significantly reduce the CRs of Fe-Cr-Ni alloys in molten chloride salts. However, there is no literature that experimentally demonstrates that a Fe-based alloy in Mg-purified $MgCl_2$-KCl-NaCl at 700 °C achieves the target of 15 μm/year.

1.2.4 Cost estimation of chloride-TES

As a next-generation TES system, the chloride-TES is expected to be superior or at least not inferior to the nitrate-TES in most key indicators, including operating temperature, lifetime, system stability, and cost. In other words, nitrate-TES is a natural reference for chloride-TES. In the roadmap of next generation CSP published by NREL [1], the cost of TES is clearly in the consideration of roadmap developers, as shown in **Fig. 2**.

The costs of each component of nitrate-TES are available in Table 1, which plays a role of baseline and reference. Extra attention is given on three variables in calculation of chloride-TES: costs of salt, hot tank, and cold tank. These three items account for 84 % of the total cost of nitrate-TES, while the costs of these parts in chloride-TES vary

significantly from those in nitrate-TES due to the different molten salt systems and operating temperatures.

Cost of the chloride salt can be estimated by multiplying mass of total chloride to unit cost, as shown in Eq. 7. The mass of chloride salt used in TES can be calculated to achieve the same heat storage capacity of nitrate-TES combining with heat capacity of chloride salt and the temperature difference between hot and cold salt, as shown in Eq. 8.

$$C_{chloride} = c_{chloride} \cdot m \quad \text{Eq. 7}$$

$$m = \frac{Q}{k_2 \cdot c_p \cdot \Delta T} \quad \text{Eq. 8}$$

where,

$C_{chloride}$ is the cost of the chloride salt inventory in USD.

$c_{chloride}$ is unit cost of chloride salt in USD/kg.

Q is the heat storage capacity of a molten salt TES in MWh$_{th}$,

m is the mass of the molten salt involved in two tanks in kg,

c_p is the heat capacity of molten salt in kJ/(°C·kg),

ΔT is the temperature difference between cold and hot tank in °C,

k_2 is a constant of 2.78×10^{-7} MWh/kJ,

The cold/hot tank costs of chloride-TES can be estimated by three factors: F_1 (volume factor), F_2 (cost factor of alloy) and F_3 (stress factor), as shown in Eq. 9, Eq. 10, Eq. 11, and Eq. 12 [1].

$$C_{chloride\ tank} = C_{nitrate\ tank} \cdot F_1 \cdot F_2 \cdot F_3 \quad \text{Eq. 9}$$

$$F_1 = (V_{chloride}/V_{nitrate})^{0.8} \quad \text{Eq. 10}$$

$$F_2 = (A_{chloride}/A_{nitrate}) \quad \text{Eq. 11}$$

$$F_3 = (S_{nitrate}/S_{chloride}) \quad \text{Eq. 12}$$

where,

$C_{chloride\ tank}$ is cost of chloride tank in USD,

$C_{nitrate\ tank}$ is cost of nitrate tank in USD,

F_1 is equal to the ratio between volume of chloride salt ($V_{chloride}$) and nitrate salt ($V_{nitrate}$) with 0.8 scaling exponent,

F_2 is equal to the ratio between unit cost of alloy used in chloride-TES ($A_{chloride}$) and nitrate-TES ($A_{nitrate}$),

F_3 is equal to the ratio between maximum allow stress of alloy used in chloride-TES ($S_{chloride}$) and nitrate-TES ($S_{nitrate}$). The maximum allowable stress is available in the standard of ASME Boiler & Pressure Vessel code [23].

As shown in **Fig. 2**, based on such estimation model, the NREL has estimated the cost of chloride-TES with Ha 230 hot tank and SS 347 cold tank. In this case, the cost of chloride-TES is 58 USD/kWh$_{-th}$, which is much expensive than nitrate-TES (20-33 USD/kWh$_{-th}$). Currently, there is no estimation of chloride-TES cost with stainless steel or other in-expensive Fe-based alloy tanks, due to the doubts of researchers about the compatibility of Fe-based alloys with highly corrosive chloride salts. Hence, it is meaningful to establish cost estimation of chloride-TES with Fe-based alloys as main structural materials based on the results of corrosion experiments.

1.3 Breaking the trilemma of material selection for chloride-TES

The following paragraph discusses the aim and scope of the presented work in a broader context. The current trilemma of structural material selection for chloride-TES can be summarized in a triangle as shown in **Fig. 5** (a). Three key parameters for structural metals are placed at the vertex of a triangle as corrosion resistance in molten chloride salt (compatibility), cost-effective compared with main structural materials of nitrate-TES, and mechanical properties. On each of the three sides of the triangle are three different types of material, one material can only satisfy the requirements of the two attached vertexes but not the opposite vertex. As can be seen, nickel-based alloy is too expensive to be selected as the main structural material. Some non-metallic materials (e.g., ceramics) show acceptable corrosion resistance in molten chloride salt, but their poor mechanical properties (e.g., low ductility) limit their use in complex components such as tanks, pipes, valves, pumps, etc. Fe-based alloy is widely used in nitrate-TES, as shown in Table 1. However, the compatibility issues, especially corrosion issue, of Fe-based alloy with $MgCl_2$-KCl-NaCl at high temperature is still a challenging problem, hindering the further development of chloride-TES with Fe-based alloy.

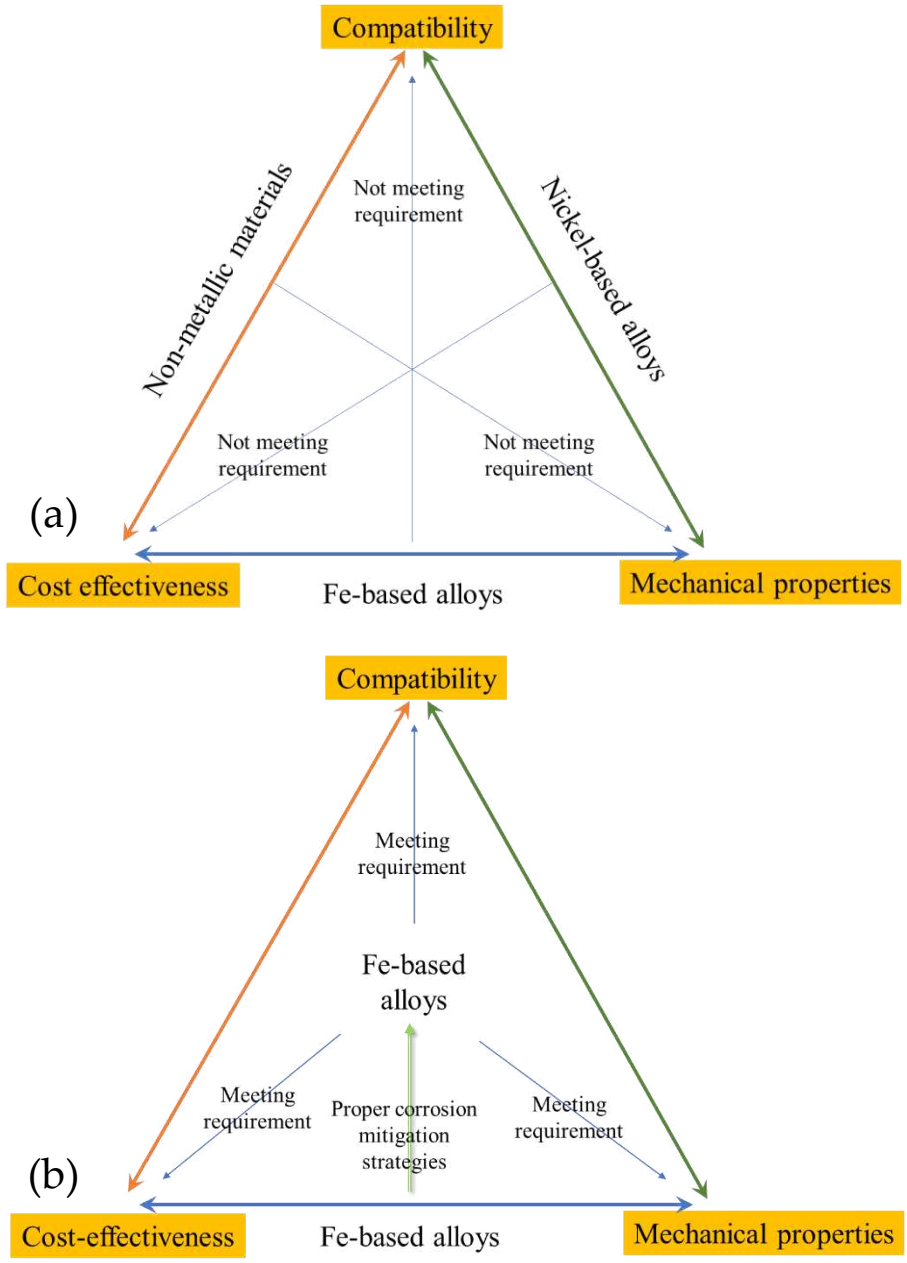

Fig. 5. (a) the trilemma of material selection for chloride-TES. (b) with proper corrosion mitigation strategies, the Fe-based alloy could meet all requirements of compatibility, cost-effectiveness, and mechanical properties.

Breaking the trilemma of molten chloride salt TES is a key step in advancing molten chloride salt technology. One promising approach to break this trilemma could involve achieving a CR of < 15 μm/year for Fe-based alloys through proper corrosion mitigation strategies, as shown in Fig. 5 (b). However, there is no experimental evidence that the Fe-based alloy can achieve such a target in a cost-effective way (e.g.,

Mg-additive). One possible reason is that the existing measurements of MgOHCl have the limits above the acceptable level for stainless steel in molten chloride salt. Another possible reason is that the salt purification process needs to be optimized to meet the acceptable concentration of MgOHCl.

A potential route to achieve the CR target of Fe-based alloys in molten chloride salt is to develop an optimized purification method for molten chloride salt, based on a lower limit MgOHCl monitoring method. Then the compatibility of such purified salt with Fe-based alloys should be investigated. The CRs of alloy samples in molten chloride salt should be studied by both mass loss and microstructural analysis, with the expectation of achieving a CR < 15 μm/year at ≥ 700 °C.

During this study, some research gaps in this direction were filled and summarized in three journal papers, which are listed in Chapter 2.

In the work presented in Paper I, a direct titration technique was developed to measure the concentration of MgOHCl at the level of < 0.01 wt.% (< 100 ppm). The reliable MgOHCl concentration data obtained by titration were used to calibrate the electrochemical data of the CV to develop an in-situ monitoring technique for MgOHCl at the tens of ppm level.

In the work presented in Paper II, the exposure test procedure was optimized by immersing the steel samples in the molten salt, which had been purified with liquid Mg. The SS 310 (EN 1.4845) and In 800H (EN 1.4876) were exposed in $MgCl_2$-KCl-NaCl for up to 2000 h (~2.8 months) at 700 °C with 2.8 wt.% Mg under an inert atmosphere. After the exposure test, the corrosion behavior of the metal samples was characterized via microscopic and mass loss methods. In parallel, corrosion impurity (MgOHCl) and corrosion products (e.g., Cr^{x+}, Fe^{x+}, and Ni^{x+}) in the salt samples were also quantitatively analysed separately with the direct titration presented in Paper I and atomic absorption spectroscopy (AAS).

In the work presented in Paper III, the P91 (EN 1.4903) and SS 304 (EN 1.4301) were selected as the candidates for the cold tank structural materials. The $MgCl_2$-KCl-NaCl were purified with liquid Mg at 700 °C, according to the procedure described in Paper II. The P91 and SS 304 samples were then exposed to the $MgCl_2$-KCl-NaCl melts at 500 °C for up to 1400 h. Then, the extracted salt samples of this series of experiments were analysed by direct titration and AAS, as in Paper II. The CR of the alloy samples was determined by microscopic and mass loss methods. Finally, the cost of the P91 cold tank for chloride-TES was estimated based on the corrosion test and data available in the literature [1,23].

2 Publications

2.1 Papers and contribution report

I. Monitoring of Extremely Low-Concentration Corrosive Impurity MgOHCl in Molten $MgCl_2$–KCl–NaCl

Gong Q, Ding W, Chai Y, Bonk A, Steinbrecher J, Bauer T. Chemical Analysis and Electrochemical Monitoring of Extremely Low-Concentration Corrosive Impurity MgOHCl in Molten $MgCl_2$–KCl–NaCl. Frontiers in Energy Research. 2022;10.https://doi.org/10.3389/fenrg.2022.811832

Qing Gong contributed to the conception and design of the study, performed the statistical analysis, wrote the first draft of the manuscript.

II. Compatibility of Fe-based alloys with purified molten $MgCl_2$-KCl-NaCl salt at 700 °C

Gong Q, Shi H, Chai Y, Yu R, Weisenburger A, Wang D, Bonk A, Bauer T, Ding W. Molten chloride salt technology for next-generation CSP plants: Compatibility of Fe-based alloys with purified molten $MgCl_2$-KCl-NaCl salt at 700 °C. Applied Energy. 2022;324:119708.https://doi.org/10.1016/j.apenergy.2022.119708

Qing Gong contributed to the conceptualization, methodology, investigation, writing – original draft, and visualization.

III. Selection of cold tank structural material utilizing corrosion control at 500 °C

Gong Q, Hanke A, Kessel F, Bonk A, Bauer T, Ding W. Molten chloride salt technology for next-generation CSP plants: Selection of cold tank structural material utilizing corrosion control at 500 °C. Solar Energy Materials and Solar Cells. 2023;253. https://doi.org/10.1016/j.solmat.2023.112233

Qing Gong contributed to the writing – original draft, visualization, methodology, investigation, and conceptualization.

2.2 International conferences

Some of the research results in this thesis have been published in the following international conferences:

- Gong Q, Ding W, Chai Y, Shi H, Bonk A, Bauer T: Molten Chloride Salts for Thermal Energy Storage in Next Generation CSP: Mg Inhibitory Effect in Corrosion Control System (CCS) for $MgCl_2$-KCl-NaCl, **IRES 2021**, Oral presentation, 2021.03, online
- Gong Q, Ding W, Shi H, Chai Y, Yu R, Weisenburger A, Wang D, Bonk A, Bauer T: Molten chloride salt technology for next-generation CSP plants: Compatibility of cost-effective Fe-based alloys with Mg-purified molten $MgCl_2$-KCl-NaCl at 700°C, **ICAE 2021**, Oral presentation, 2021.11, online.
- Gong Q, Ding W, Bonk A, Bauer T: In- and ex-situ monitoring of extremely low MgOHCl in molten chloride salt for next-generation CSP, **EUCHEMSIL 2022**, Oral presentation, 2022.06, Patras, Greece.
- Gong Q, Ding W, Bonk A, Bauer T: Molten Chloride Salt Technology for Next-generation CSP Plants: An Economically Competitive Future Scenario Using Fe-based Alloys with Corrosion Control, **SolarPaces 2022**, Oral presentation, 2022.09, Albuquerque, NM, USA.

Paper I: Monitoring of Extremely Low-Concentration Corrosive Impurity MgOHCl in Molten $MgCl_2$–KCl–NaCl

Gong Q, Ding W, Chai Y, Bonk A, Steinbrecher J, Bauer T. Chemical Analysis and Electrochemical Monitoring of Extremely Low-Concentration Corrosive Impurity MgOHCl in Molten $MgCl_2$–KCl–NaCl. Frontiers in Energy Research. 2022;10.https://doi.org/10.3389/fenrg.2022.811832

Publications

frontiers | Frontiers in Energy Research

ORIGINAL RESEARCH
published: 22 June 2022
doi: 10.3389/fenrg.2022.811832

Chemical Analysis and Electrochemical Monitoring of Extremely Low-Concentration Corrosive Impurity MgOHCl in Molten $MgCl_2$–KCl–NaCl

Qing Gong[1], Wenjin Ding[1]*, Yan Chai[1], Alexander Bonk[1], Julian Steinbrecher[1] and Thomas Bauer[2]*

[1]Institute of Engineering Thermodynamics, German Aerospace Center (DLR), Stuttgart, Germany, [2]Institute of Engineering Thermodynamics, German Aerospace Center (DLR), Cologne, Germany

$MgCl_2$–KCl–NaCl is a promising thermal energy storage (TES) material and heat transfer fluid (HTF) with high operating temperatures of >700°C for next-generation concentrating solar power (CSP) plants. One major challenge for future implementation of the molten chloride TES/HTF technology arises from the presence of some corrosive impurities, especially MgOHCl, a hydrolysis product of hydrated $MgCl_2$. Even extremely low-concentration MgOHCl (tens of ppm O in weight) can cause unneglectable corrosion of commercial Fe–Cr–Ni alloys, which limits their service time as the structural materials in the molten chloride TES/HTF system. Thus, the chemical analysis and monitoring techniques of MgOHCl at the tens of ppm O level are vital for corrosion control. In this work, a chemical analysis technique based on direct titration and a high-precision automatic titrator was developed for an exact measurement of MgOHCl at the tens of ppm O level. It shows a standard deviation below 5 ppm O and an average error below 7 ppm O when the concentration of MgOHCl is 36 ppm O. Moreover, compared to other methods available in some literature reports, it can exclude the influence of co-existing MgO on the MgOHCl concentration measurement. This chemical analysis technique was used to calibrate the previously developed electrochemical method based on cyclic voltammetry (CV) to achieve reliable *in situ* monitoring of MgOHCl in the $MgCl_2$–KCl–NaCl molten salt at a concentration as low as the tens of ppm O level. The *in situ* monitoring technique shows a monitoring limitation of <39 ppm O. The two techniques for MgOHCl measurement developed in this work could be used to develop an *in situ* corrosion control system to ensure the long service time of the molten chloride TES/HTF system in next-generation CSP plants.

Keywords: MgOHCl concentration measurement, direct titration, cyclic voltammetry, corrosion control, next-generation concentrating solar power

OPEN ACCESS

Edited by:
Xiaohui She,
University of Birmingham,
United Kingdom

Reviewed by:
Yafei Wang,
University of Wisconsin-Madison,
United States
Brenda Garcia-Diaz,
Savannah River National Laboratory
(DOE), United States
Zhu Jiang,
Southeast University, China
Zhongfeng Tang,
Shanghai Institute of Applied Physics
(CAS), China

****Correspondence:***
Qing Gong
qing.gong@dlr.de
Wenjin Ding
wenjin.ding@dlr.de

Specialty section:
This article was submitted to Process and Energy Systems Engineering, a section of the journal Frontiers in Energy Research

Received: *09 November 2021*
Accepted: *10 May 2022*
Published: *22 June 2022*

Citation:
Gong Q, Ding W, Chai Y, Bonk A, Steinbrecher J and Bauer T (2022) Chemical Analysis and Electrochemical Monitoring of Extremely Low-Concentration Corrosive Impurity MgOHCl in Molten $MgCl_2$–KCl–NaCl. Front. Energy Res. 10:811832. doi: 10.3389/fenrg.2022.811832

INTRODUCTION

$MgCl_2$–KCl–NaCl molten chloride salt has received much attention in recent years due to its wide working temperature range (420–800°C), low vapor pressure, low material cost, and good heat capacity (Mehos et al., 2017; Ding et al., 2018a; Turchi et al., 2018; Villada et al., 2021). It has potential use in the next-generation concentrating solar power (CSP) plants as thermal energy storage (TES) material and heat transfer fluid (HTF), allowing the operating temperature of the CSP plant to be increased from about 560°C to >700°C. With such a high operating temperature, the energy efficiency of the power cycle in the CSP plant can rise from 40% to >50% when integrated with the supercritical carbon dioxide (sCO_2) Brayton power cycle, which would significantly reduce the levelized cost of electricity (LCOE) of CSP (Mehos et al., 2017). However, the molten $MgCl_2$–KCl–NaCl mixture is strongly corrosive to commercial Fe-Cr-Ni alloys even under a protective inert atmosphere (Ding et al., 2018c; Sun et al., 2018), which greatly limits its application.

Numerous studies have shown that the corrosion in molten $MgCl_2$–KCl–NaCl salt is caused by corrosive impurities, especially MgOHCl (Ding et al., 2018c; Choi et al., 2019; Grégoire et al., 2020; Sun et al., 2020; Zhao, 2020), not by the molten chloride salt itself (Zhang et al., 2020). As a consequence of the strong hygroscopicity of $MgCl_2$, some moisture is inevitably absorbed in $MgCl_2$–KCl–NaCl in practical applications. Subsequently, the main corrosive impurity MgOHCl is generated as a hydrolysis product during heating in the melting process, resulting in the strong salt corrosivity to the metallic structural materials, such as Fe–Cr–Ni alloys (Kipouros and Sadoway, 2001; Kashani-Nejad, 2005; Ding et al., 2018c). To represent the concentration of MgOHCl (*C(MgOHCl)*)in the molten salt, the unit parts per million oxygen (*ppm O*) is defined as the mass fraction of oxygen ($m_{O\ in\ MgOHCl}$) in the total mass of the salt sample (m_{sample}), as shown in **Eq. 1** (Skar, 2001).

$$C(MgOHCl)[ppm\ O] = m_{O\ in\ MgOHCl} \Big/ m_{sample} \times 10^6 \quad (1)$$

The estimated acceptable impurity level of MgOHCl for the different types of alloys based on the literature (Ding et al., 2018c; Ding et al., 2019a; Ding et al., 2019b; Kurley et al., 2019) and their relative cost factors (Gilardi et al., 2006) are summarized in **Table 1**. To allow the use of inexpensive alloys (e.g. stainless steels) for TES/HTF with molten $MgCl_2$–KCl or $MgCl_2$–KCl–NaCl at ≥700°C, the salt impurity needs to be controlled at the tens of ppm O level by monitoring and salt purification to control the salt corrosivity (Ding et al., 2019b; Kurley et al., 2019). As shown in **Figure 1**, a corrosion control system (CCS) integrated into the molten chloride TES/HTF system has been proposed in the previous work, which contains the main parts—part of online corrosion monitoring and part of corrosion mitigation (Villada et al., 2021). For CCS, reliable *in situ* and *ex situ* monitoring techniques of MgOHCl at the tens of ppm level are vital to ensure its effectiveness, efficiency, and economics.

To measure the oxygen-containing impurity concentration or redox potential of molten salts, electrochemical methods including cyclic voltammetry (CV) (Skar, 2001; Ding et al., 2017; 2018b; Choi et al., 2019; Gonzalez et al., 2020; Guo et al., 2021), square wave voltammetry (SWV) (Song et al., 2018), chronopotentiometry (CP) (Zhang et al., 2020), and open-circuit potentiometry (OCP) (Choi et al., 2019; Gonzalez et al., 2020) have been employed in molten chloride salts (Williams et al., 2021). Among them, an approach combining *in situ* and *ex situ* measurement of $MgOH^+Cl^-$ was investigated, in which cyclic voltammetry (CV) was employed as the *in situ* measurement of MgOHCl (Skar, 2001; Ding et al., 2018b; Guo et al., 2021), while *ex situ* methods of titration (Skar, 2001; Ding et al., 2018b) and carbothermal reduction (Skar, 2001) were used for the *ex situ* measurement to calibrate the *in situ* CV measurement. The reduction peak in the cyclic voltammogram—peak *B*, shown in **Figure 2**, represents the reaction of $MgOH^+$ to MgO, as shown in **Eq. 2** (Skar, 2001; Ding et al., 2018b; Guo et al., 2021). Moreover, the current density of peak B in the cyclic voltammogram is linearly linked to the concentration of $MgOH^+$.

$$MgOH^+ + e^- \rightarrow MgO(s) + \frac{1}{2}H_2(g) \quad (2)$$

It was pointed out in the work of Skar (2001) and Ding et al. (2018b) that the *ex situ* measurements based on titration and carbothermal reduction could result in an over-measurement of the $MgOH^+$ concentration and biased calibration of CV since

TABLE 1 | Comparison of the Ni content, cost of the alloys, and their estimated acceptable impurity level with a target corrosion rate of 15 μm/year at ≥700°C for molten $MgCl_2$-KCl or $MgCl_2$-KCl-NaCl under inert atmosphere.

Alloy	Example	Ni (wt%)	Relative cost factor (compared to 3-series stainless steel)	Acceptable MgOHCl level	Data source
3-series stainless steel	SS 310 and SS 316	<30	1	Tens of ppm O	Ding et al. (2019b) Kurley et al. (2019)
Incoloy	In 800 H	30–50	~2.5	Tens of ppm O	Ding et al. (2019a) Ding et al. (2019b)
Hastelloy	Ha 276, Ha 230, and Ha N	>50	~10	Hundreds of ppm O	Ding et al. (2018c) Ding et al. (2019b) Kurley et al. (2019)

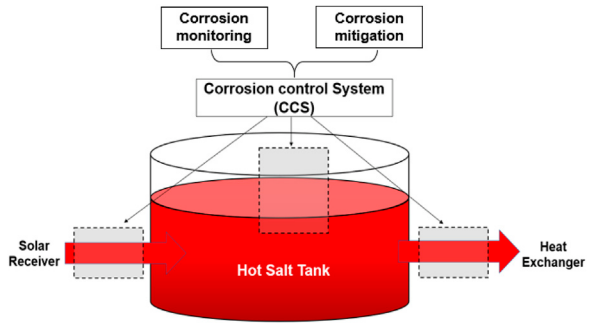

FIGURE 1 | Corrosion control system (CCS) integrated into the molten chloride TES/HTF system, which contains the online corrosion monitoring and mitigation parts, and has been proposed in the previous work (Villada et al., 2021).

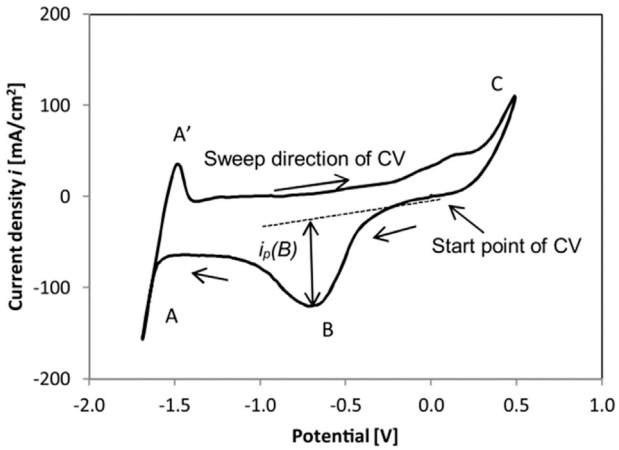

FIGURE 2 | Cyclic voltammogram in eutectic $MgCl_2$/KCl/NaCl at 500°C obtained by a tungsten working electrode with a sweep rate of 200 mV/s (Ding et al., 2017; 2018b).

other impurities (e.g. MgO or H_2O) cannot be quantitatively excluded in these *ex situ* measurements. In the $MgCl_2$-KCl-NaCl molten salt, non-corrosive MgO and corrosive MgOHCl commonly co-exist. When the temperature is >555°C, MgOHCl can be decomposed into MgO and HCl, as shown in **Eq. 3** (Kipouros and Sadoway, 2001; Kashani-Nejad et al., 2005).

$$MgOHCl \rightarrow MgO(s)+HCl(g) \quad (3)$$

To measure non-corrosive MgO and corrosive MgOHCl separately, Klammer et al. (2020) used water and methanol to extract MgOHCl/MgO based on the solubility difference (Klammer et al., 2020). This method can measure the concentration of MgOHCl down to 0.1 wt% (~200 ppm O) by a typical ethylenediaminetetraacetic acid (EDTA) titration technique and has been used to measure the purity of $MgCl_2$-containing chloride mixtures after pre-purification. However, due to the solubility of MgOHCl in methanol, this method cannot measure the extremely low-concentration MgOHCl.

In general, it was proposed that the *in situ* electrochemical CV measurement of MgOHCl calibrated by a reliable *ex situ* chemical analysis method is a promising approach to monitor MgOHCl (i.e., salt corrosivity) in molten $MgCl_2$–KCl–NaCl. However, existing electrochemical and chemical measurement methods of MgOHCl have minimum measurement limits above the acceptable MgOHCl level. For corrosion control, the MgOHCl concentration should be controlled at tens of ppm O to allow inexpensive alloys (e.g., stainless steel) to withstand the corrosion of molten $MgCl_2$–KCl–NaCl at ≥700°C. In this experiment, aiming to develop reliable chemical analysis and *in situ* monitoring techniques for MgOHCl at the tens of ppm O level, the following experiments were designed and carried out:

- Different concentrations of MgOHCl from thousands to tens of ppm O level were obtained by electrolysis at 500°C and thermal decomposition at 600 and 700°C.
- A chemical analysis technique based on direct titration and a high-precision automatic titrator was developed to measure MgOHCl concentration at the tens of ppm O level.
- The reliable concentration data on MgOHCl obtained by titration were used to calibrate the CV data to develop an *in situ* monitoring technique for MgOHCl at tens of ppm O.

EXPERIMENTAL

Materials and Experimental Setup

KCl (purity >99 wt%) and NaCl (purity >99 wt%) were purchased from Alfa Aesar, Germany, while anhydrous $MgCl_2$ (purity >99 wt%) was supplied by Magnesia, Germany. They were used to synthesize the eutectic salt mixture of $MgCl_2$-NaCl-KCl (47.1-30.2-22.7 mol%) for the experiments. This eutectic salt composition is suggested by the previous work (Villada et al., 2021).

Figure 3 shows the setup of electrochemical experiments. A chemically stable glassy carbon crucible purchased from HTW Germany (Sigradur® G) was used in this work to prevent the reaction of the strongly corrosive molten chloride salt with the crucible. The 250 g chloride salts were heated in an argon atmosphere (purity ≥99.999%, H_2O ≤ 0.5 ppm, 10 nL/h, and pressure above atmospheric pressure of about 0.1 bar) to 500°C, 600°C, or 700°C. As shown in **Figure 3**, an alumina plate was used under the glassy carbon crucible to electrically insulate the glassy carbon and the autoclave system made of steel from each other.

As shown in **Figure 3**, five electrodes were used for electrolysis and cyclic voltammetry (CV). All the electrochemical experiments were conducted using a ZENNIUM electrochemical workstation from Zahner GmbH (Germany). **Table 2** summarizes the electrodes used in different electrochemical experiments and the material composition of these electrodes. Three tungsten electrodes (1 mm diameter, purity >99.5%, purchased from Alfa Aesar) were used as working (~32 mm^2), counter (~100 mm^2), and quasi reference electrodes (~100 mm^2) for CV, while two graphite electrodes

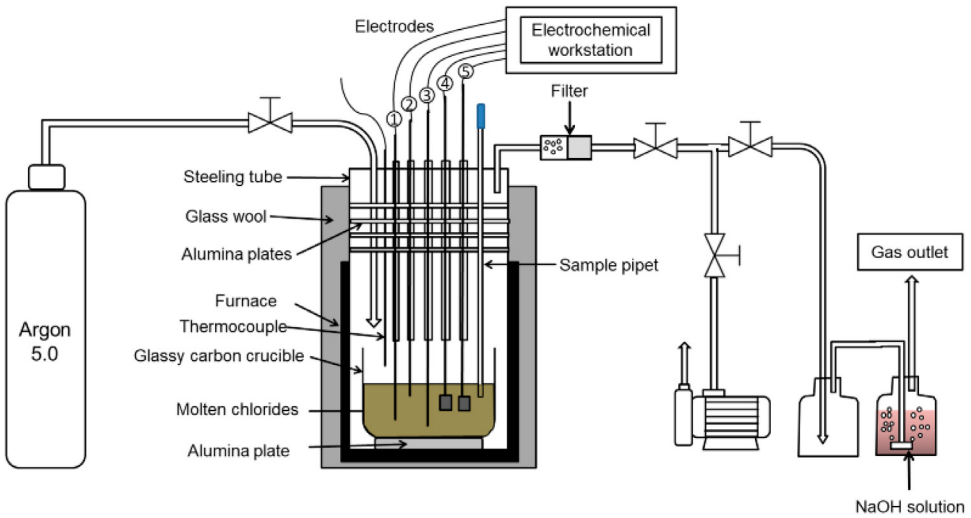

FIGURE 3 | Schematic representation of the experimental setup for electrochemical salt purification and CV experiments.

TABLE 2 | Electrodes used for electrochemical purification *via* electrolysis and monitoring the impurity concentration *via* CV.

Experiment	Application	Electrodes shown in Figure 3		
		Working	Counter	Reference
Electrolysis	Electrochemical purification	4	5	—
Cyclic voltammetry (CV)	Monitoring impurity concentration	2	3	1

1: tungsten quasi-reference electrode (~100 mm^2). 2: tungsten working electrode (~32 mm^2). 3: tungsten counter electrode (~100 mm^2). 4: graphite anode (10 mm × 40 mm) + tungsten wire for salt purification. 5: graphite cathode (10 mm × 40 mm) + tungsten wire for salt purification

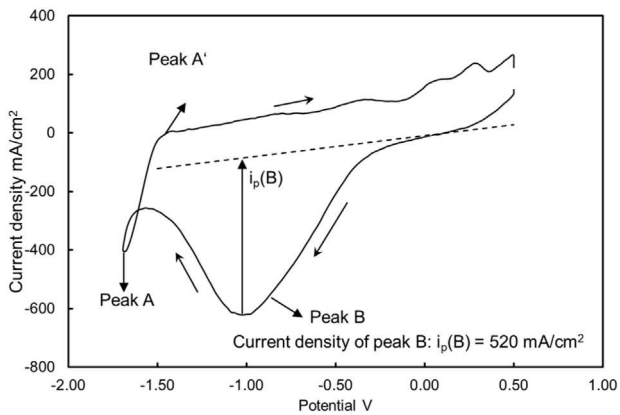

FIGURE 4 | Example of a cyclic voltammogram for molten $MgCl_2$-KCl-NaCl salt with impurity ion $MgOH^+$ at 500°C. The current density of peak B in this case was 520 mA/cm^2. The working, reference, and counter electrodes of CV were tungsten. Sweep rate: 200 mV/s.

(size: 40 mm × 10 mm x 2 mm) were used for electrochemical purification. Due to their larger surface area compared with tungsten electrodes used in our previous work (Ding et al., 2017; 2018b), graphite electrodes with a 4 cm^2 area were used to have a fast purification rate and be able to purify more salt before electrode passivation.

CV Experiments

Three groups of CV experiments at different temperatures (500°C, 600°C, and 700°C) were conducted. Once the temperature of the salt reached the target temperature, the counter electrode, reference electrode of CV, and the two graphite electrodes of electrolysis were inserted into the molten salts but without touching the crucible bottom, while the immersion depth of the working electrode of CV was fixed to 10 mm (i.e., the contact area of the tungsten electrode with the melt is about 31.4 mm^2). A sweep rate of 200 mV/s was used in all CV experiments as in the previous work (Ding et al., 2017; 2018b), while the potential voltage of CV was from 0.5 V to −1.7 V *vs.* reference.

Figure 4 is an example cyclic voltammogram of the eutectic $MgCl_2$-NaCl-KCl salt before electrolysis treatment at 500°C, in which peak B represents the reduction reaction in **Eq. 2** and is in line with the previous work (Ding et al., 2018b).

Skar (2001) and Guo et al. (2021) discovered that the peak current density of the peak B (i_p(B)) is proportional to the concentration of MgOHCl (C(MgOHCl)) in molten $MgCl_2$-NaCl or (-KCl) salts(Skar, 2001; Guo et al., 2021), which is in

accordance with the Randles–Sevcik equation (Randles, 1948; Ševčík, 1948):

$$i_p(B) = 0.4463\ \frac{(nF)^{\frac{3}{2}}}{(RT)^{\frac{1}{2}}} C^{\infty}(MgOHCl) D^{\frac{1}{2}} v^{\frac{1}{2}} \quad (4)$$

where $i_p(B)$ represents the current density of peak B in A/m^2, n is the number of electrons transferred in the reaction (n = 1 for the reduction reaction in **Eq. 2**), F is the Faraday's constant (F = 96,485.3 C/mol), R is the universal gas constant (R = 8.314 J/(Kmol)), T is the temperature of the molten salt in K, C^{∞} (MgOHCl) is the bulk concentration of MgOHCl in mol/m^3, D is the diffusion coefficient of the reacting species (here $MgOH^+$) in m^2/s, which is a function of temperature, and v is the potential sweep rate in V/s. In this study, sweep rate v is a fixed value of 0.2 V/s (200 mV/s). However, considering the limit of MgO solubility in molten $MgCl_2$-containing chloride salts (Boghosian et al., 1991), MgO was habitually saturated in this work. Hence, the equation is amended to the soluble-insoluble model of the Berzins–Delahay equation (Berzins and Delahay, 1953), as shown in **Eq. 5**.

$$i_p(B) = 0.6105\ \frac{(nF)^{\frac{3}{2}}}{(RT)^{\frac{1}{2}}} C^{\infty}(MgOHCl) D^{\frac{1}{2}} v^{\frac{1}{2}} \quad (5)$$

Eq. 5 can be simplified to **Eq. 6**, where the concentration of *C(MgOHCl) [ppm O]* is proportional to $i_p(B)$. Thus, the current density of peak B obtained from CV can be used to monitor the concentration of $MgOH^+$ impurities *in situ* in the molten chloride salts (Skar, 2001). The $k(T, D)$ in **Eq. 5** is related to the temperature, sweep rate, and diffusion coefficient of the CV measurement, as shown in **Eq. 7**, where $c_2 = 3.3 \times 10^{-2}$ (ppm Ocm^3·mV ^{½})/(mAK^{½}·s) is calculated with a fixed sweep rate of 200 mV/s, *R, F,* and n in **Eq. 5**.

$$C(MgOHCl)\ [ppm\ O] = k(T, D).i_p(B) \quad (6)$$

$$k(T, D) = c_2\left(\frac{T}{Dv}\right)^{\frac{1}{2}} \quad (7)$$

In the CV experiments, all current densities of peak B were read with a tangent at the starting point of peak B as the baseline (see **Figure 4**). The current densities of peak B would then be calibrated using an advanced titration process (see *Titration Experiments* section) to improve the measurement accuracy and precision of CV.

In order to study the relationship between the current density of peak B and the concentration of MgOHCl in the molten salt (i.e., calculating the $k(T, D)$ in **Eq. 6**), the different concentrations of MgOHCl were achieved by electrolysis and thermal decomposition. In this work, different concentrations of MgOHCl at 600 and 700°C were obtained through thermal decomposition during a certain waiting time since MgOHCl decomposes to MgO and HCl at temperature >555°C, as shown in **Eq. 3** (Kipouros and Sadoway, 2001; Kashani-Nejad et al., 2005). As the heating time increased, the concentration of MgOHCl in the molten salt gradually decreased. At 500°C, different MgOHCl concentrations were obtained through electrolysis. For electrolysis, the voltage between the working electrode and counter electrode was 1.7 V, preventing the formation of Mg at a voltage higher than 1.7 V (see Peak A in **Figure 4**). The corrosive MgOHCl impurity was decomposed by electrolysis:

$$Cathode\ (Reduction):\ 2MgOH^+ + 2e^- \rightarrow 2MgO(s) + H_2(g) \quad (8)$$

$$Anode\ (Oxidation):\ Cl^- \rightarrow Cl_2(g) + 2e^- \quad (9)$$

Figures 5A,B show the flowchart of CV experiments at 500, 600, and 700°C. Cyclic voltammograms were obtained at different temperatures and different MgOHCl concentrations. After each CV experiment, 1–2 g chloride salts, as shown in **Figure 5C**, were taken out from the crucible using a sample pipet (see **Figure 3**) for further titration experiments. During the short sample extraction, the system remained under an Ar (purity: 99.999%) atmosphere all the time to avoid air leakage into the autoclave. Combining the data on titration and CV experiments, $k(T, D)$ is determined.

Titration Experiments

The acid consumption method based on titration was used for the quantitative measurement of the total amount of MgOHCl in a salt sample. A high-precision automatic titration instrument, *905 Titrando,* purchased from *Metrohm Germany,* was employed. The titration method is as follows: first, about 500 mg sample was weighed by using an analytical balance. Then, the solid samples were dissolved in a beaker with 150 ml of ultrapure water (HiPerSolv, VWR, Germany). After installation of the beaker with samples, the standard titrant (0.01 M HCl) was charged into a 20 ml cylinder from the reagent bottle and then dripped into the salt solution through the rotation of the gear at an average rate of 0.2 ml/min (slower at pH values near 7). Meanwhile, a stirrer homogenized the solution. The titration was performed under a nitrogen purge to exclude any interference from carbon dioxide/carbonic acid. Hydrochloric acid solution (0.01 M) purchased from Merck KGaA was used to prepare the standard titrant. The titer of the HCl solution was calibrated with sodium carbonate (Na_2CO_3). The pH value and the amount of the consumed titrant were plotted by the computer, as shown in **Figure 6**. The equivalence point (EP) is marked out, where moles of acid (HCl) and moles of base (MgOHCl) neutralize each other, as shown in **Eq. 10**.

$$MgOH^+(aq.) + H^+(aq.) \rightarrow Mg^{2+}(aq.) + H_2O(l) \quad (10)$$

$$C(MgOHCl)[ppm\ O] = ti \times C_{HCl} \times V_{HCl} / m_{sample} \times M_O \times 1000 \quad (11)$$

The concentration of MgOHCl in samples in ppm O is calculated according to **Eq. 11**, where *ti* is the titer of HCl, i.e., the ratio of actual concentration to theoretical concentration (0.01 M); V_{HCl} is the volume of HCl at EP in mL; C_{HCl} is 0.01 mol/L; m_{sample} is the mass of the salt sample in g, M_O is the molar mass of oxygen, i.e., 16 g/mol.

Error Analysis for Titration and CV

For *ex situ* direct titration to measure the concentration of MgOHCl in 500 mg samples, there are two main sources of error: one caused by the co-existing MgO impurity in the salt

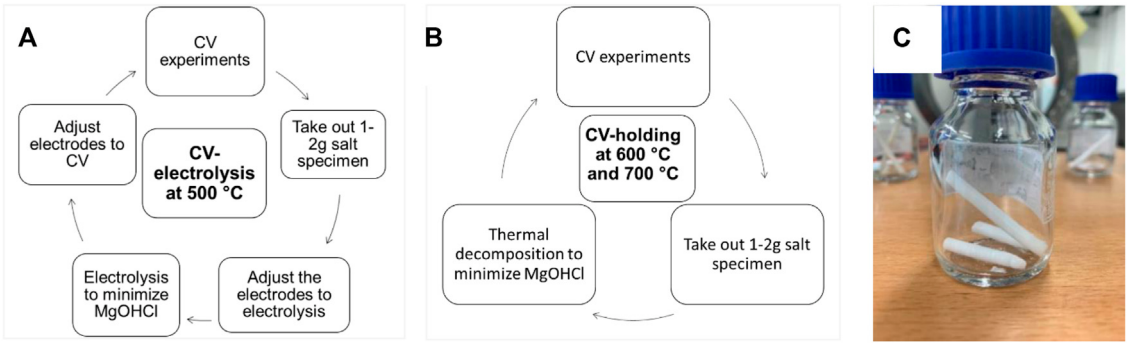

FIGURE 5 | Flowchart of CV experiments at **(A)** 500°C, **(B)** 600, and 700°C; **(C)** salt specimen taken from the glassy carbon crucible for titration.

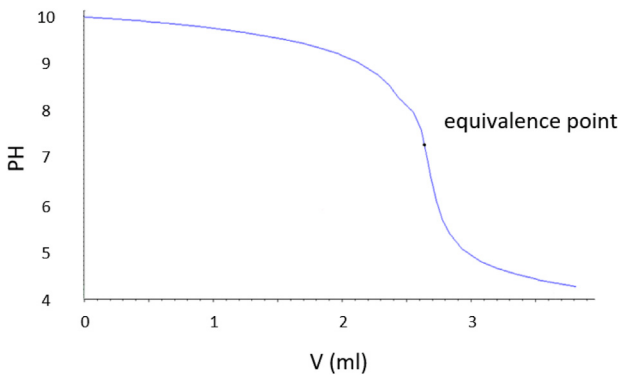

FIGURE 6 | Typical pH change curve of a direct titration of a salt sample containing MgOHCl with the 0.01 M HCl titrant recorded by using the high-precision titrator.

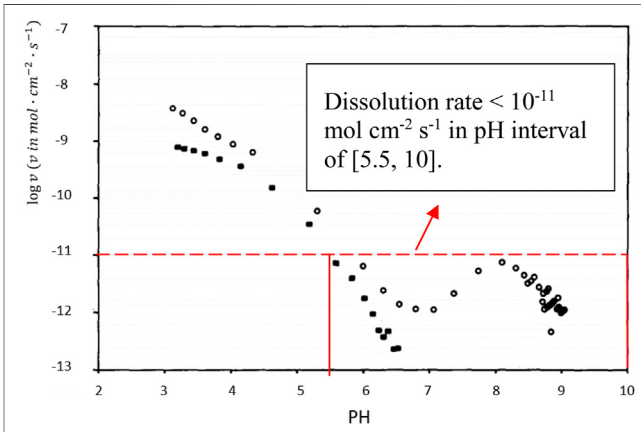

FIGURE 7 | pH *vs*. the rate of dissolution of MgO powder (°) and a (100) MgO crystal (■) at 25°C in aqueous solution (Fruhwirth et al., 1985). The dissolution rate is smaller than 10^{-11} mol cm^{-2} s^{-1} in the pH interval of [5.5, 10].

sample and another caused by the titration experiment (i.e., titration conditions and equipment).

For the first error, once the $MgCl_2$-KCl-NaCl-(MgO-MgOHCl) sample is placed in water, two types of impurities will dissolve in the water or react with water, as shown in **Eq. 12** and **Eq. 13** (Chen et al., 2018; Klammer et al., 2020).

$$MgOHCl \rightarrow Mg^{2+} + OH^{-} + Cl^{-} \quad (12)$$

$$MgO + H_2O \rightarrow Mg^{2+} + 2OH^{-} \quad (13)$$

Empirically, the dissolution of MgOHCl in water (see **Eq. 12**) occurs rapidly, when the aqueous solution is not saturated with $Mg(OH)_2$ (i.e., pH < 10.4) (Dong et al., 2010). In this work, the pH value of the salt solution for titration was smaller than 10 because of the low MgOHCl concentration (<4000 ppm O in salt samples), as shown in **Figure 6**. Unlike the rapid dissolution of MgOHCl shown in **Eq. 12**, the reaction between MgO and H_2O shown in **Eq. 13** has been experimentally proved slow in an alkali or a neutral environment, as shown in **Figure 7** (Fruhwirth et al., 1985). As can be seen, in the pH range of 6–9, the dissolution rate of MgO is less than 10^{-11} mol cm^{-2} s^{-1}. Thus, when we know the diameter and concentration of MgO particles in the system, the amount of HCl consumed by MgO can be estimated. Taking the highest concentration of MgOHCl (4000 ppm O) as a reference, the maximum mass fraction of MgO was 1 wt% (assuming that all MgOHCl was converted to MgO) (Zhao, 2020). We measured the diameter of MgO in $MgCl_2$-KCl-NaCl and found that the broad peak of the laser-based particle-size analyzer was 10–30 μm. Using the parameters mentioned earlier and the density of MgO (3.58 g/cm^3), the total surface area (A) in 250 g of chloride salt can be calculated, as shown in **Table 3**. Then, the maximum dissolution rate of MgO in this direct titration experiment can be calculated according to **Eq. 14**.

$$E = \frac{k.A.M_o}{m_s} \times 60 \times 2 \times 10^6 \quad (14)$$

where E is the error caused by MgO in ppm O/min; k is the MgO dissolution rate, adopting 10^{-11} mol cm^{-2} s^{-1}; A is total MgO surface area in cm^2, listed in **Table 3**; M_O is the molar mass of oxygen, i.e., 16 g/mol; m_s is the total salt mass, 250 g; *60* is the factor of second to minute; *2* means one MgO equivalent to two MgOHCl in titration; and 10^6 is the factor of ppm.

TABLE 3 | Error caused by the dissolution of MgO with different particle sizes in an aqueous solution with pH 5.5–10.4.

Salt mass in g	Maximum MgO fraction in wt%	MgO particle diameter (D) in μm	Total MgO surface area (A) in cm^2	Dissolution rate (k) in mol/(Cm^2 s)	Maximum error (E) in ppm O/min
250	1	10	4190	10^{-11}	0.32
250	1	20	2095	10^{-11}	0.16
250	1	30	1397	10^{-11}	0.10

TABLE 4 | Thirteen times direct titration experiments with the standard $Mg(OH)_2$ solution to determine RSD and relative error at a concentration equivalent 36 ppm O in 500-mg salt sample.

C($MgOH_2$) in mol/L	Volume in ml	V (0.01 M HCl) in ml (theoretical)	V (0.01 M HCl) in ml (titration)	Equivalent MgOHCl ppm O in 500 mg salt sample (theoretical)	Equivalent MgOHCl ppm O in 500 mg salt sample (titration)	Relative error %
1.13×10^{-5}	50	0.11	0.1381	36	44	23.15
1.13×10^{-5}	50	0.11	0.1363	36	44	21.54
1.13×10^{-5}	50	0.11	0.1522	36	49	35.72
1.13×10^{-5}	50	0.11	0.1291	36	42	15.12
1.13×10^{-5}	50	0.11	0.1418	36	46	26.45
1.13×10^{-5}	50	0.11	0.1244	36	40	10.93
1.13×10^{-5}	50	0.11	0.1285	36	41	14.59
1.13×10^{-5}	50	0.11	0.1583	36	51	41.16
1.13×10^{-5}	50	0.11	0.1246	36	40	11.11
1.13×10^{-5}	50	0.11	0.1384	36	45	23.42
1.13×10^{-5}	50	0.11	0.1090	36	35	−2.80
1.13×10^{-5}	50	0.11	0.12	36	38	4.06
1.13×10^{-5}	50	0.11	0.1280	36	41	14.14

The calculated error caused by MgO in ppm O/min is listed in **Table 3**. In the direct titration, the time required for the titration to reach EP was not exceeded by 5 min for neutralization of 50 ppm O MgOHCl by 0.01 M HCl, which means that the titration error due to co-existing MgO is less than 1.6 ppm O (0.32 × 5) for the MgOHCl concentration measurement.

The second error source of the measurement based on direct titration in this work was the experimental error, which could be caused by the dissolved carbon dioxide (i.e. carbonic acid) and the fluctuation of the HCl amount injected by gear etc. An experiment was carried out to determine the relative standard deviation (RSD) and percentage error of direct titration. An amount of 1.308 mg of $Mg(OH)_2$ was weighed and dissolved in 2 L distilled water as the 1.13×10^{-5} mol/L $Mg(OH)_2$ standard solution. Then, about 50 ml of standard solution was extracted and measured by direct titration, whose HCl consumption is equivalent to 36 ppm O MgOHCl in the 500 mg salt sample. The titration of the standard solution was repeated 13 times to obtain sufficient data for statistical analysis (see **Table 4**). It was found that the average standard deviation was 4.35 ppm O (RSD = 10.2%), and the average error was +6.62 ppm O (average relative error = +18%) for measuring the equivalent of 36 ppm O MgOHCl in 500 mg samples by direct titration using the titrator. Compared to this error, the titration error due to MgO is much smaller and thus neglectable.

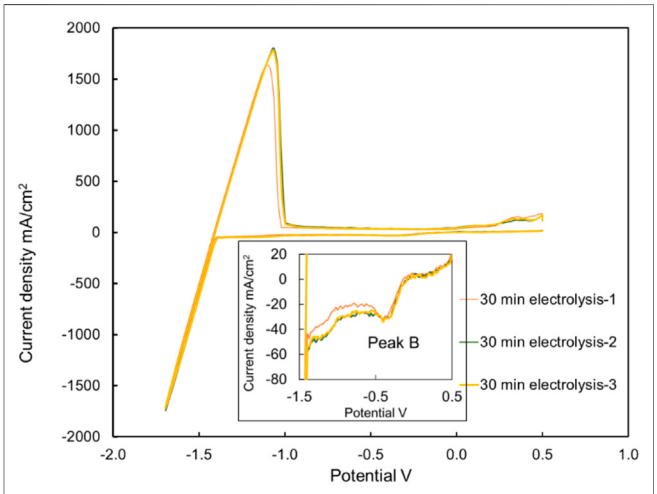

FIGURE 8 | Three cyclic voltammograms with the same molten salt batch were carried out directly and immediately after each other. The current densities of peak B were 43, 39, and 44 mA/cm^2 in three measurements, respectively. Temperature: 500°C, after 30 min electrolysis. Working, reference, and counter electrodes of CV: tungsten. Sweep rate: 200 mV/s.

For *in situ* measurement by CV, the repeatability of cyclic voltammograms is significant to determine the current density of peak B and link it to the concentration of MgOHCl. **Figure 8**

TABLE 5 | Summary of the precision and accuracy for direct titration and CV. Data on direct titration come from repeated titration of 36 ppm O equivalent MgOHCl; data on CV come from repeated scanning of 500°C salts after 30-min electrolysis.

Measurement method	Absolute error	Relative error (accuracy) %	Standard deviation	Relative standard deviation (RSD, precision) %
Direct titration	+6.62 ppm O	+18 (at 36 ppm O)	4.35 ppm O	10.2 (at 36 ppm O)
CV	Calibrated by direct titration	Calibrated by direct titration	2.65 mA/cm^2	6.3 (at 42 mA/cm^2)

displays three times the CV curves in molten chloride salt at 500°C after 30 min of electrolysis at 1.7 V. The difference of $i_p(b)$ in the same situation is the deviation of the current density. The average height of peak B is 42 mA/cm^2, while the relative standard deviation (RSD) is 6.3%, showing good stability at the low current density of $i_p(b)$. Generally, the closer to the detection limit, the greater will be the relative standard deviation. The 42 mA/cm^2 height of peak B is the smallest current density obtained at 500°C. Due to the thermal decomposition of MgOHCl (**Eq. 3**), the CV voltammograms at 600 and 700°C are not suitable for error analysis. The MgOHCl concentration changed during several CV measurements at 600 and 700°C. Hence, for all the CV measurements in this work, the relative standard errors are set at 6.3%.

Both precision and accuracy data in this work are summarized in **Table 5**. To determine the MgOHCl concentrations in salt samples and their errors, three titrations were carried out for each sample. When the standard deviation of one batch of samples was higher than 6.62 ppm O (the average error), the standard deviation of three titrations was adopted as the main error source. When the standard deviation was smaller than 6.62 ppm O, the average error (6.62 ppm O) was adopted as the domination error for the direct titration.

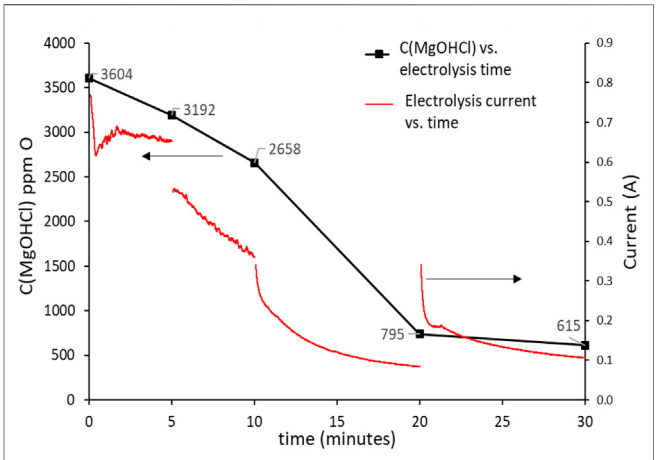

FIGURE 9 | Concentration of MgOHCl at 500°C decreases with the increasing electrolysis time. The black line using the left *y*-axis shows the concentration of MgOHCl in ppm O; the red line using the right *y*-axis shows the electrolysis current in A.

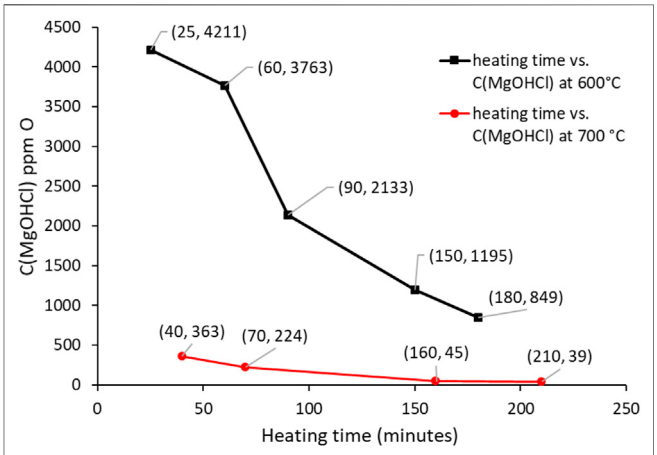

FIGURE 10 | Concentration of MgOHCl decreases with increasing holding time at 600 and 700°C.

RESULTS AND DISCUSSION

In previous work, some efforts have been made to understand the relation between the height of peak B (in **Figure 2**) and the concentration of MgOHCl in the $MgCl_2$-containing chloride salts (Skar, 2001; Ding et al., 2017; 2018b; Choi et al., 2019; Gonzalez et al., 2020; Guo et al., 2021). It was found that adding NaOH can increase the height of peak B because of the reaction shown in **Eq. 15**. In addition, the potential difference between peak B and peak A is comparable ~1.5 V. The reactions corresponding to peak A and peak A' are seen as the typical peaks of Mg^{2+} reduction and its reverse reaction of Mg oxidation, as shown in **Eq. 16** and **Eq. 17**, respectively, which can be seen as a marker. This evidence suggests that the peak at the potential of about 0 V in this work can be seen as the peak B corresponding to the reaction shown in **Eq. 2**. Different from the previous work (Ding et al., 2018b; Guo et al., 2021), the gradient of the MgOHCl concentration in this work was not obtained by adding NaOH but was obtained by electrolysis and thermo-decomposition to decrease the concentration of MgOHCl. Hence, the concentration of MgOHCl in this work was reduced to tens of ppm O since this level was interesting for corrosion control.

$$Mg^{2+}+OH^- \rightarrow MgOH^+ \quad (15)$$

$$\text{Peak A}: Mg^{2+}+2e^- \rightarrow Mg \quad (16)$$

$$\text{Peak A}': Mg \rightarrow Mg^{2+}+2e^- \quad (17)$$

Concentration of MgOHCl Measured by Titration

The decrease in the MgOHCl concentration with electrolysis time at 500°C is shown in **Figure 9**, while the decrease in the MgOHCl concentration by thermal decomposition at 600 and 700°C with enhanced holding time is displayed in **Figure 10**. All the concentration data in **Figures 9**, **10** were obtained by the direct titration method.

Figure 9 shows the relationship between the concentration of MgOHCl and electrolysis time. Generally, the concentration of MgOHCl decreased with the increasing electrolysis time at 500°C. However, as can be seen from the red line in **Figure 9**, the first two electrolysis experiments were carried out for 5 min, with the decrease in current from ~700 to ~400 mA, while the last two electrolysis experiments were conducted for 10 min with the decrease in current from ~400 to ~100 mA because of the MgO passivation. During the running of electrolysis, the poor electrical conductivity of MgO was generated, as shown in **Eq. 8**, which covered the surface of the graphite electrode and hindered electronic transmission, leading to the low efficiency of MgOHCl removal (Ding et al., 2019a). Two methods were carried out in order to mitigate the problem of the passive MgO film on the electrode and increase the efficiency of electrolysis. First, the positive and negative electrodes of electrolysis were reversed after each electrolysis. Once reversing the cathode and anode, an instantaneous recovery was displayed on the current curve, which could be attributed to the disruption of the MgO film by the generated chlorine gas (Ding et al., 2021). The reversing electrodes did not completely solve the problem of electrode passivation. Hence, second, after the first two times of 5-min electrolysis, the duration of electrolysis time was expanded to 10 min to obtain a measurable reduction of MgOHCl at lower currents.

Compared to our previous work (Ding et al., 2017), the electrolysis electrodes were improved. The tungsten wire electrodes were replaced by 10 mm × 40 mm graphite foils. After 30 min of electrolysis, the MgOHCl concentration decreased from 3603 ppm O to 415 ppm O, i.e., the concentration of MgOHCl was reduced to about 17% of the original concentration. In our previous work (Ding et al., 2017), after 25 min of electrolysis with a tungsten wire electrode, the concentration of $MgOH^+$ was reduced to only 69% of the original $MgOH^+$ concentration (from 10,400 ppm O to 7200 ppm O).

At 600 and 700°C, the reason for the decrease of MgOHCl with increasing heating time is the thermal decomposition of MgOHCl (Kipouros and Sadoway, 2001). Furthermore, the impurity level at 600°C was significantly higher than at 700°C because MgOHCl decomposes faster at 700°C than at 600°C, which compares well with that reported in some literature reports (Kashani-Nejad, 2005; Kashani-Nejad et al., 2005). In addition, before molten chloride salt reached 700°C, thermal decomposition had already occurred at the temperature range between 600 and 700°C during heating with a 5 K/min rate.

For comparison, **Table 6** lists different measurement methods of MgOHCl in molten $MgCl_2$-containing chlorides (Skar, 2001; Ding et al., 2017, 2018b; Kurley et al., 2019; Klammer et al., 2020). Kurley et al. (2019) carried out the method of direct titration to measure oxygen-containing impurities in the salt samples, which were purified by CCl_4 bubbling with as low as 1.6 ppm O impurity. This indicates that direct titration is suitable for the low concentration impurity determination of the molten chloride salt. However, the authors did not discuss the error based on their results nor did they explain the principle of direct titration to measure MgOHCl in $MgCl_2$-containing salt. In this study, it was confirmed that direct titration can measure the tens of ppm O level MgOHCl with acceptable errors. In addition, this method can exclude the interference of MgO with a relatively uncomplicated method, compared with the method published by Ding et al. (2018b) and Klammer et al. (2020). Therefore, it has relatively higher precision than the back-titration employed in our previous work (Ding et al., 2017; 2018b).

CV Results

As shown in **Figures 11–13**, the cyclic voltammograms in this work show similar features to those in the literature (Ding et al., 2018b; Choi et al., 2019; Guo et al., 2021). For example, the potential of peak B is about 1.5 V higher than that of peak A at 500–700°C. Although the height of peak A′ is not relevant to the MgOHCl concentration, it is still noticeable that the heights of oxidation peaks are different from each other. Peak A′ corresponds to the oxidation of Mg to Mg^{2+}, as shown in **Eq. 17**. This can be explained by the fact that the amount of deposition Mg on the tungsten electrodes increased as the experiment proceeded, resulting in reaction enhancement at peak A'. When the MgOHCl concentration in melts was relatively high, the deposition Mg can react with MgOHCl rapidly, as shown in **Eq. 18**. After electrolysis or decomposition, the MgOHCl concentration decreased significantly, resulting in a slower reaction of **Eq. 18** and more Mg deposition on the electrodes. This deposition of Mg could cause the high peak A'.

$$MgOHCl(l)+Mg(s/l) \rightarrow MgO(s)+MgCl_2(l)+H_2(g) \quad (18)$$

Comparing the concentrations shown in **Figure 9** and the heights of peak B shown in **Figure 11**, it is clearly visible that the height of peak B decreases from 453 to 42 mA/cm^2, with the decreasing concentration of MgOHCl from 3640 to 615 ppm O at 500°C with 30-min electrolysis at 1.7 V. Similarly, comparing the heights of peak B in **Figures 12**, **13**, with the decomposition of MgOHCl, the heights of peak B decreased significantly at 600 and 700°C as well. After 180 min of holding in the furnace under an argon atmosphere at 600°C, the current density of peak B decreased from 507 to 69 mA/cm^2, corresponding to the concentration of MgOHCl decreasing from 4211 to 894 ppm O as seen from the black line in **Figure 10**. At 700°C, after 210 min of holding, the current density of peak B decreased from 166 to 24 mA/cm^2, which corresponds to 363 and 39 ppm O MgOHCl (the red line in **Figure 10**). In general, the height of peaks B in this work always decreases with the decline in the MgOHCl concentration measured by titration.

It is a promising method to measure the MgOHCl concentration *in situ* with the current density of peak B on

TABLE 6 | Comparison with measurement methods of MgOHCl in molten chlorides.

Measurement method	Separate measurement of MgOHCl and MgO	Minimum detection limit	Measurement accuracy ppm O	Data source
Carbothermal reduction–acid consumption–iodometric titration	Yes	>70 ppm O	±20	Skar, (2001)
Extraction-EDTA titration	Yes	>200 ppm O	±40 (0.02 wt% MgOHCl)	Klammer et al. (2020)
Direct titration	Yes	~1.6 ppm O	(not analyzed)	Kurley et al. (2019)
Back titration	No	>200 ppm O	~200	Ding et al. (2017) Ding et al. (2018b)
Direct titration using a high-precision automatic titrator	Yes	~36 ppm	~6.62	This work

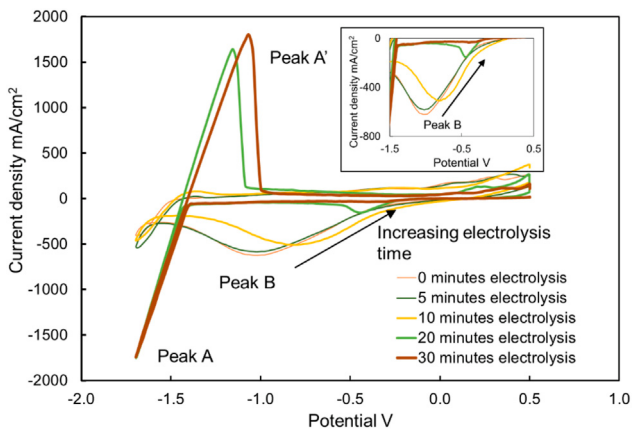

FIGURE 11 | Cyclic voltammograms of chloride molten salt before electrolysis (i.e., 0 min), after 5, 10, 20, and 30 min of electrolysis at 500°C. The working, counter, and reference electrodes of CV with a sweep rate of 200 mV/s were tungsten. The working and counter electrodes of electrolysis were graphite. The voltage on the working and counter electrodes of electrolysis was kept at −1.7 V.

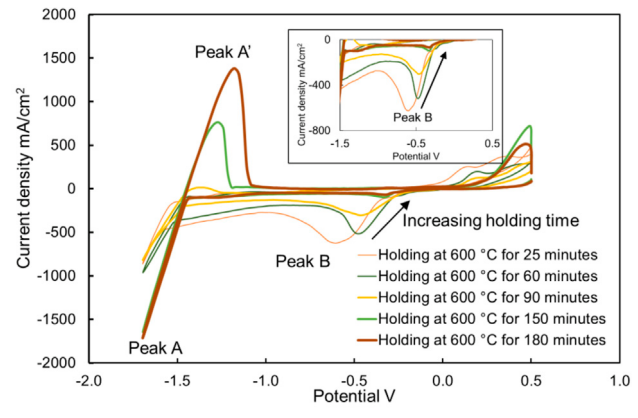

FIGURE 12 | Cyclic voltammograms of chloride molten salt, holding at 600°C for 25, 60, 90, 150, and 180 min. The working, reference, and counter electrodes of CV were tungsten. Sweep rate: 200 mV/s.

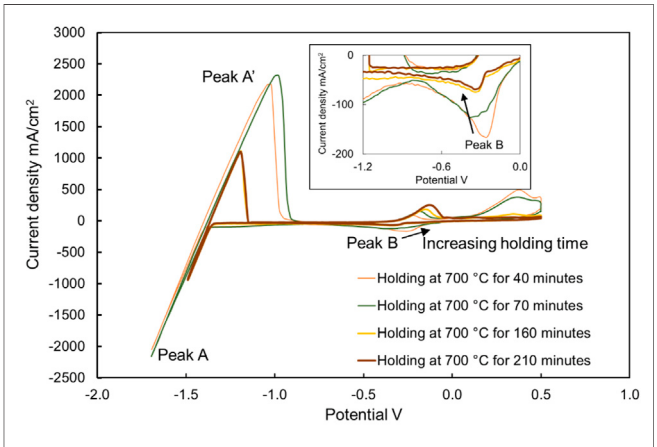

FIGURE 13 | Cyclic voltammograms of chloride molten salt, holding at 700°C for 40, 70, 160, and 210 min. The working, reference, and counter electrodes of CV were tungsten. Sweep rate: 200 mV/s. There is a correlation between the current density and impurity concentration.

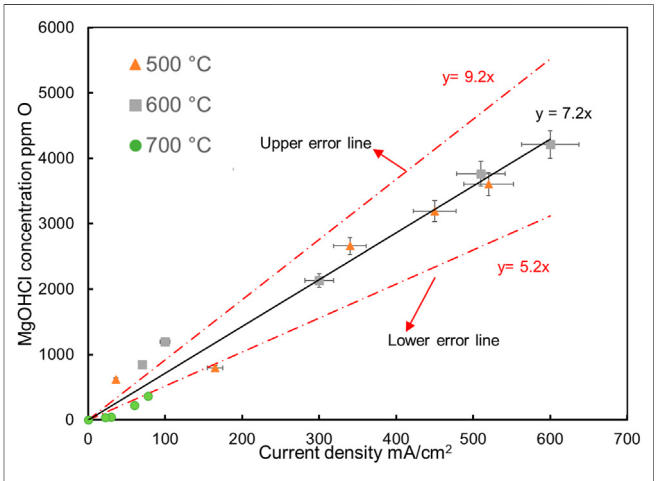

FIGURE 14 | Peak B current densities *vs*. concentrations of MgOHCl in molten $MgCl_2$-NaCl-KCl (47.1-30.2-22.7 mol%) at 500°C (▲), 600°C (■) and 700°C (●). Error bars in this plot are from section (Error analysis for titration and CV). The solid lines are the linear regressions.

TABLE 7 | Comparison of slopes of peak current densities *vs*. concentrations of $MgOH^+$(k(T, D)) in molten chlorides determined in this work and reported in the literature (Skar, 2001; Ding et al., 2018b).

T (°C)	k (T, D) (ppm O)/(mA/Cm^2)	Molten chlorides	Data sources
500–700	7.2 ± 2	$MgCl_2$-KCl-NaCl (47/30/23 mol%)	This work
500	38.2 ± 7.6	$MgCl_2$-KCl-NaCl (60/20/20 mol%)	Ding et al. (2018b)
600	13.7 ± 2.7	$MgCl_2$-KCl-NaCl (60/20/20 mol%)	
700	9.4 ± 1.9	$MgCl_2$-KCl-NaCl (60/20/20 mol%)	
728–848	37 ± 8	$MgCl_2$-NaCl (90/10 mol%)	Skar, (2001)
741–842	28 ± 6	$MgCl_2$-NaCl (80/20 mol%)	
730–848	22 ± 4	$MgCl_2$-NaCl (41.5/58.5 mol%)	
730–850	21 ± 6	$MgCl_2$-NaCl (30/70 mol%)	

CV (an electrochemical signal) when it can be calibrated by the *ex situ* measurement. In previous work, it has been repeatedly demonstrated that the density of peak B is linearly related to the concentration of MgOHCl in $MgCl_2$-containing molten chloride salts (Skar, 2001; Ding et al., 2017, 2018b; Choi et al., 2019; Gonzalez et al., 2020; Guo et al., 2021). This work attempted to extend this linear relationship to the tens of ppm O level MgOHCl impurities. All the titration and CV data obtained with *ex situ* and *in situ* measurements are summarized and shown in **Figure 14**, which show the linear relationship between the MgOHCl concentration and the current density of peak B even when the concentration of MgOHCl is low to 39 ppm O. When all the data were between the two error lines, the slope k(T, D) in **Eq. 6** for MgOHCl at 500–700°C was between 5.2 and 9.2 (i.e., 7.2 ± 2) (ppm O)/(mA/cm^2).

Although the linear relationship between MgOHCl and current density in this work is consistent with the literature, the slope k(T, D) obtained in this work is smaller than that in the literature (Skar, 2001; Ding et al., 2017; 2018b) with the same sweep rate of 200 mV/s, as summarized in **Table 7**. This difference may be explained as follows: first, according to **Eq. 6**, the overmeasurement of the MgOHCl concentration, which has been discussed earlier, leads to a larger slope k(T, D). In our previous work (Ding et al., 2017; 2018b), in back titration with 0.1 M HCl (pH = 1), MgO unavoidably reacted with HCl, leading to over-measured concentrations of MgOHCl. In the work of Skar (2001), the concentration of MgOHCl was obtained by combining carbothermal reduction and iodometric titration. The impurities of O_2 or H_2O contained in the salt could also lead to overmeasurement of the O element in carbothermal reduction, further leading to overmeasurement of MgOHCl. Second, according to **Eq. 7**, $k(T, D)$ decreases with the increasing diffusion coefficient (D). As pointed out by Skar (2001), with the increasing $MgCl_2$ content in molten chloride salt, the diffusion coefficient of $MgOH^+$ decreases. The molar fraction of $MgCl_2$ in this work was 47.1 mol%, which is smaller than that in our previous work, which was 60 mol%. Thus, the diffusion coefficient of $MgOH^+$ in this work could be larger than that of our previous work, resulting in a smaller k(T, D). These overlapping factors lead to the difference in the slopes between this work and previous work.

In our previous work, the value of k(T, D) was given separately at the temperatures of 500°C, 600°C, and 700°C. However, in this study, the same value of k(T, D) was obtained at 500–700°C (the key operating temperature range of the molten chloride TES/HTF system), being in line with that of Skar (2001). There are two reasons for giving the same value of k(T, D) in this work. First, when the k(T, D) values were calculated separately, the difference between these values was small. The k(T, D) values were ~7, ~7.5, and ~4 at 500°C, 600°C, and 700°C, respectively. Second, the *in situ* monitoring technique of MgOHCl by CV would be employed as a warning system in the corrosion control system (Villada et al., 2021). Under this condition, the lowest measurable value of MgOHCl concentration is of interest, regardless of the temperature.

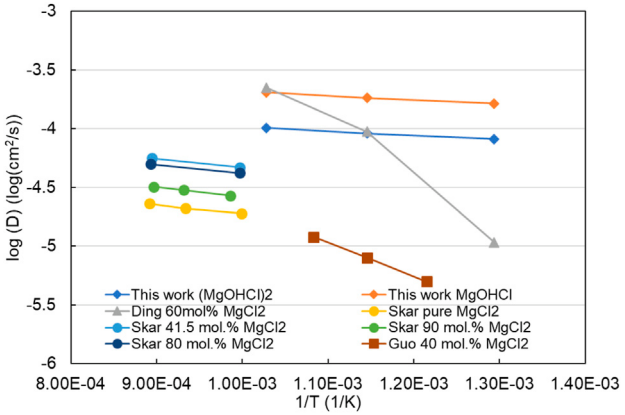

FIGURE 15 | $\log_{10}$(D) *vs*. 1/T of this work and the literature in the melts with different concentrations of $MgCl_2$. "This work MgOHCl and $(MgOHCl)_2$" means that the diffusion coefficients are calculated based on the dissolution form as MgOHCl and $(MgOHCl)_2$ in molten $MgCl_2$-KCl-NaCl with 47.1 mol% $MgCl_2$, respectively.

The diffusion coefficient (D) of MgOHCl can be estimated with the known k(T, D) value and the fixed sweep rate (200 mV/s in this work), according to **Eq. 4** (Berzins–Delahay equation). The estimated diffusion coefficients of MgOHCl in $MgCl_2$-KCl-NaCl at 500°C, 600°C, and 700°C were 1.64 × 10^{-4} cm^2/s, 1.83 × 10^{-4} cm^2/s, and 2.04 × 10^{-4} cm^2/s, respectively. In addition, it was pointed out in the literature (Schenin-King and Picard, 1993; Skar, 2001) that the dissolved MgOHCl in molten chloride salt could be a dimer, i.e., $(MgOHCl)_2$. When the calculation is based

on the dimer $(MgOHCl)_2$, the estimated diffusion coefficients at 500°C, 600°C, and 700°C were 8.20×10^{-5} cm^2/s, 9.14×10^{-5} cm^2/s, and 1.02×10^{-4} cm^2/s, respectively. The Arrhenius relationship ($\log_{10}$(D) *vs*. 1/T) of this work and published data are summarized in a plot, as shown in **Figure 15**. The estimated diffusion coefficients of this work are higher than those in the literature (Skar, 2001; Ding et al., 2018b; Guo et al., 2021), which is mainly caused by the relatively higher k(D, T) adopted in the calculation. Moreover, when the dissolved impurity is considered as the dimer $(MgOHCl)_2$ with two electrons transferred at peak B, the calculated diffusion coefficients are lower than those based on the monomer MgOHCl. In addition, the published diffusion coefficients are estimated by the soluble-soluble Randles–Sevcik equation, while the estimation in this work is based on the soluble-insoluble Berzins–Delahay equation.

CONCLUSION

The $MgCl_2$-KCl-NaCl molten salt shows low corrosivity to the metallic structural materials (i.e., alloys) at ≥700°C when the concentration of the main corrosive impurity MgOHCl is as low as tens of ppm O. To allow the use of inexpensive alloys (e.g. stainless steels) for TES/HTF with $MgCl_2$-KCl-NaCl molten salt at ≥700°C, the salt impurity needs to be controlled at the tens of ppm O level by using the corrosion control system (CCS), including the online corrosion monitoring subsystem and corrosion mitigation subsystem. Thus, reliable chemical analysis and monitoring techniques of MgOHCl at the tens of ppm O level are vital in CCS to ensure its effectiveness, efficiency, and economics.

This work developed a chemical analysis technique based on direct titration and a high-precision automatic titrator, which can measure MgOHCl at the tens of ppm O level, e.g., 36 ppm O MgOHCl with a measurement error of about 7 ppm O. This chemical analysis technique was used to calibrate the *in situ* monitoring technique based on the CV developed in our previous work. The obtained CV data (i.e., peak current density) for 500–700°C shows good linearity with the data on direct titration (i.e., MgOHCl concentration) in the range from 39 to 4211 ppm O. The slope of the concentration of MgOHCl vs. the peak current density in CV was 7.2 ±2 (ppm O)/(mA/cm^2) at 500–700°C. Using the calibrated CV technique and the slope in CCS, the corrosive impurity of MgOHCl low to tens of ppm O could be monitored *in situ* with quick response and cost-effectively. With the slope value, the estimated diffusion coefficients of MgOHCl in $MgCl_2$-KCl-NaCl at 500–700°C were 1.64×10^{-4}–2.04×10^{-4} cm^2/s, when it is assumed that the existing form of MgOHCl is the monomer $MgOH^+$.

The two techniques for MgOHCl measurement developed in this work could be used to develop an *in situ* corrosion control system to ensure the long service time of the molten chloride TES/HTF system in next-generation CSP plants. Some future work is suggested to realize the commercial application of these techniques:

- the design of the *in situ* monitoring subsystem based on CV including the electrodes and their material selection,
- building a molten chloride test loop and testing the CV technique and subsystem under dynamic conditions of molten chlorides close to the real application conditions,
- testing the chemical analysis technique for the salt samples from the loop test, and
- development and testing of the corrosion mitigation techniques studied in our previous work or available in the literature in the molten chloride test loop.

DATA AVAILABILITY STATEMENT

The original contributions presented in the study are included in the article/supplementary material; further inquiries can be directed to the corresponding authors.

AUTHOR CONTRIBUTIONS

WD, QG, and YC contributed to the conception and design of the study. QG, WD, and JS performed the statistical analysis. QG wrote the first draft of the manuscript. All authors contributed to manuscript revision, read, and approved the submitted version.

ACKNOWLEDGMENTS

This research has been performed within the DLR-DAAD fellowship program (Nr. 57540125). The authors would like to thank the colleagues M. Braun, R. Hoffmann, and A. Hanke for technical support in the different laboratories.

REFERENCES

Berzins, T., and Delahay, P. (1953). Oscillographic Polarographic Waves for the Reversible Deposition of Metals on Solid Electrodes. *J. Am. Chem. Soc.* 75 (3), 555–559. doi:10.1021/ja01099a013

Boghosian, S., Godø, A., Mediaas, H., Ravlo, W., and Østvold, T. (1991). Oxide Complexes in Alkali--Alkaline-Earth Chloride Melts. *Acta Chem. Scand.* 45, 145–157. doi:10.3891/acta.chem.scand.45-0145

Chen, Y., An, Z., and Chen, M. (2018). Competition Mechanism Study of Mg+H2O and MgO+H2O Reaction. *IOP Conf. Ser. Mat. Sci. Eng.* 394, 022015. doi:10.1088/1757-899x/394/2/022015

Choi, S., Orabona, N. E., Dale, O. R., Okabe, P., Inman, C., and Simpson, M. F. (2019). Effect of Mg Dissolution on Cyclic Voltammetry and Open Circuit Potentiometry of Molten MgCl2-KCl-NaCl Candidate Heat Transfer Fluid for Concentrating Solar Power. *Sol. Energy Mater. Sol. Cells* 202, 110087. doi:10.1016/j.solmat.2019.110087

Ding, W., Bonk, A., and Bauer, T. (2018a). Corrosion Behavior of Metallic Alloys in Molten Chloride Salts for Thermal Energy Storage in Concentrated Solar Power Plants: A Review. *Front. Chem. Sci. Eng.* 12 (3), 564–576. doi:10.1007/s11705-018-1720-0

Ding, W., Bonk, A., Gussone, J., and Bauer, T. (2017). Cyclic Voltammetry for Monitoring Corrosive Impurities in Molten Chlorides for Thermal Energy Storage. *Energy Procedia* 135, 82–91. doi:10.1016/j.egypro.2017.09.489

Ding, W., Bonk, A., Gussone, J., and Bauer, T. (2018b). Electrochemical Measurement of Corrosive Impurities in Molten Chlorides for Thermal Energy Storage. *J. Energy Storage* 15, 408–414. doi:10.1016/j.est.2017.12.007

Ding, W., Gomez-Vidal, J., Bonk, A., and Bauer, T. (2019a). Molten Chloride Salts for Next Generation CSP Plants: Electrolytical Salt Purification for Reducing Corrosive Impurity Level. *Sol. Energy Mater. Sol. Cells* 199, 8–15. doi:10.1016/j.solmat.2019.04.021

Ding, W., Shi, H., Jianu, A., Xiu, Y., Bonk, A., Weisenburger, A., et al. (2019b). Molten Chloride Salts for Next Generation Concentrated Solar Power Plants: Mitigation Strategies against Corrosion of Structural Materials. *Sol. Energy Mater. Sol. Cells* 193, 298–313. doi:10.1016/j.solmat.2018.12.020

Ding, W., Shi, H., Xiu, Y., Bonk, A., Weisenburger, A., Jianu, A., et al. (2018c). Hot Corrosion Behavior of Commercial Alloys in Thermal Energy Storage Material of Molten MgCl2/KCl/NaCl under Inert Atmosphere. *Sol. Energy Mater. Sol. Cells* 184, 22–30. doi:10.1016/j.solmat.2018.04.025

Ding, W., Yang, F., Bonk, A., and Bauer, T. (2021). Molten Chloride Salts for High-Temperature Thermal Energy Storage: Continuous Electrolytic Salt Purification with Two Mg-Electrodes and Alternating Voltage for Corrosion Control. *Sol. Energy Mater. Sol. Cells* 223, 110979. doi:10.1016/j.solmat.2021.110979

Dong, C., Cairney, J., Sun, Q., Maddan, O. L., He, G., and Deng, Y. (2010). Investigation of Mg(OH)2 Nanoparticles as an Antibacterial Agent. *J. Nanopart Res.* 12 (6), 2101–2109. doi:10.1007/s11051-009-9769-9

Fruhwirth, O., Herzog, G. W., Hollerer, I., and Rachetti, A. (1985). Dissolution and Hydration Kinetics of MgO. *Surf. Technol.* 24 (3), 301–317. doi:10.1016/0376-4583(85)90080-9

Gilardi, T., Rodriguez, G., Gomez, A., Leybros, J., Borgard, J., Carles, P., et al. (2006). "Influence of Material Choice on Cost Estimation of Some Key Components of the Sulfur Iodine Thermochemical Process," in Proc. of 16th World Hydrogen Energy Conference (WHEC), 13-16 June 2006 (Lyon, France: Association Francaise pour l'Hydrogene et les Piles a Combustible AFHYPAC), 13–16.

Gonzalez, M., Faulkner, E., Zhang, C., Choi, S., and Simpson, M. F. (2020). Electrochemical Methods for Analysis of Hydroxide and Oxide Impurities in Li, Mg/Na, and Ca Based Molten Chloride Salts. *ECS Trans.* 98 (10), 161–169. doi:10.1149/09810.0161ecst

Grégoire, B., Oskay, C., Meißner, T. M., and Galetz, M. C. (2020). Corrosion Mechanisms of Ferritic-Martensitic P91 Steel and Inconel 600 Nickel-Based Alloy in Molten Chlorides. Part II: NaCl-KCl-MgCl2 Ternary System. *Sol. Energy Mater. Sol. Cells* 216, 110675. doi:10.1016/j.solmat.2020.110675

Guo, J., Hoyt, N., and Williamson, M. (2021). Multielectrode Array Sensors to Enable Long-Duration Corrosion Monitoring and Control of Concentrating Solar Power Systems. *J. Electroanal. Chem.* 884, 115064. doi:10.1016/j.jelechem.2021.115064

Kashani-Nejad, S., Ng, K.-W., and Harris, R. (2005). MgOHCl Thermal Decomposition Kinetics. *Metall Materi Trans B* 36 (1), 153–157. doi:10.1007/s11663-005-0015-2

Kashani-Nejad, S. (2005). Oxides in the Dehydration of Magnesium Chloride Hexahydrate. Montreal, Canada: McGill University. Thesis.

Kipouros, G. J., and Sadoway, D. R. (2001). A Thermochemical Analysis of the Production of Anhydrous MgCl2. *J. Light Metals* 1 (2), 111–117. doi:10.1016/S1471-5317(01)00004-9

Klammer, N., Engtrakul, C., Zhao, Y., Wu, Y., and Vidal, J. (2020). Method to Determine MgO and MgOHCl in Chloride Molten Salts. *Anal. Chem.* 92 (5), 3598–3604. doi:10.1021/acs.analchem.9b04301

Kurley, J. M., Halstenberg, P. W., McAlister, A., Raiman, S., Dai, S., and Mayes, R. T. (2019). Enabling Chloride Salts for Thermal Energy Storage: Implications of Salt Purity. *RSC Adv.* 9 (44), 25602–25608. doi:10.1039/c9ra03133b

Mehos, M., Turchi, C., Vidal, J., Wagner, M., Ma, Z., Ho, C., et al. (2017). *Concentrating Solar Power Gen3 Demonstration Roadmap*. Golden, CO (United States): United States: National Renewable Energy Lab.NREL.

Randles, J. E. B. (1948). A Cathode Ray Polarograph. Part II.-The Current-Voltage Curves. *Trans. Faraday Soc.* 44, 327–338. doi:10.1039/tf9484400327

Schenin-King, J., and Picard, G. (1993). "Oxoacidity Effect on Metallic Oxide Dissolution Reactions in Fused Chlorides," in Retrospective Collection*: Trans Tech Publ)* (Durnten, Switzerland: Publisher and Materials Science and Enginerring), 13–24.

Ševčík, A. (1948). Oscillographic Polarography with Periodical Triangular Voltage. *Collect. Czechoslov. Chem. Commun.* 13, 349–377.

Skar, R. A. (2001). *Chemical and Electrochemical Characterisation of Oxide/hydroxide Impurities in the Electrolyte for Magnesium Production*. Trondheim, Norway: Norwegian University of Science and Technology Fakultet for naturvitenskap og teknologi.

Song, J., Huang, X., Fan, Y., Yi, J., Shu, Y., and He, J. (2018). *In Situ* Monitoring of O2–Concentration in Molten NaCl-KCl at 750°C. *J. Electrochem. Soc.* 165 (5), E245–E249. doi:10.1149/2.1101805jes

Sun, H., Wang, J.-Q., Tang, Z., Liu, Y., and Wang, C. (2020). Assessment of Effects of Mg Treatment on Corrosivity of Molten NaCl-KCl-MgCl2 Salt with Raman and Infrared Spectra. *Corros. Sci.* 164, 108350. doi:10.1016/j.corsci.2019.108350

Sun, H., Wang, J., Li, Z., Zhang, P., and Su, X. (2018). Corrosion Behavior of 316SS and Ni-Based Alloys in a Ternary NaCl-KCl-MgCl2 Molten Salt. *Sol. Energy* 171, 320–329. doi:10.1016/j.solener.2018.06.094

Turchi, C. S., Vidal, J., and Bauer, M. (2018). Molten Salt Power Towers Operating at 600-650 °C: Salt Selection and Cost Benefits. *Sol. Energy* 164, 38–46. doi:10.1016/j.solener.2018.01.063

Villada, C., Ding, W., Bonk, A., and Bauer, T. (2021). Engineering Molten MgCl2-KCl-NaCl Salt for High-Temperature Thermal Energy Storage: Review on Salt Properties and Corrosion Control Strategies. *Sol. Energy Mater. Sol. Cells* 232, 111344. doi:10.1016/j.solmat.2021.111344

Williams, T., Shum, R., and Rappleye, D. (2021). Review-Concentration Measurements in Molten Chloride Salts Using Electrochemical Methods. *J. Electrochem. Soc.* 168 (12), 123510. doi:10.1149/1945-7111/ac436a

Zhang, M., Ge, J., Yin, T., and Zhang, J. (2020). Redox Potential Measurements of Cr(II)/Cr Ni(II)/Ni and Mg(II)/Mg in Molten MgCl2-KCl-NaCl Mixture. *J. Electrochem. Soc.* 167 (11), 116505. doi:10.1149/1945-7111/aba15a

Zhao, Y. (2020). *Molten Chloride Thermophysical Properties, Chemical Optimization, and Purification*. Golden, CO (United States): National Renewable Energy Lab.NREL.

Conflict of Interest: The authors declare that the research was conducted in the absence of any commercial or financial relationships that could be construed as a potential conflict of interest.

Publisher's Note: All claims expressed in this article are solely those of the authors and do not necessarily represent those of their affiliated organizations, or those of the publisher, the editors, and the reviewers. Any product that may be evaluated in this article, or claim that may be made by its manufacturer, is not guaranteed or endorsed by the publisher.

Paper II: Compatibility of Fe-based alloys with purified molten $MgCl_2$-KCl-NaCl salt at 700 °C

Gong Q, Shi H, Chai Y, Yu R, Weisenburger A, Wang D, et al. Molten chloride salt technology for next-generation CSP plants: Compatibility of Fe-based alloys with purified molten $MgCl_2$-KCl-NaCl salt at 700 °C. Applied Energy. 19708.https://doi.org/10.1016/j.apenergy.2022.119708

Applied Energy 324 (2022) 119708

Contents lists available at ScienceDirect

Applied Energy

journal homepage: www.elsevier.com/locate/apenergy

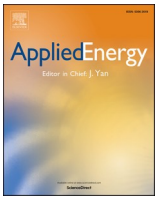

Molten chloride salt technology for next-generation CSP plants: Compatibility of Fe-based alloys with purified molten $MgCl_2$-KCl-NaCl salt at 700 °C☆

Qing Gong [a,*], Hao Shi [b], Yan Chai [a], Rui Yu [b,c], Alfons Weisenburger [b], Dihua Wang [c], Alexander Bonk [a], Thomas Bauer [d], Wenjin Ding [a]

[a] Institute of Engineering Thermodynamics, German Aerospace Center (DLR), Stuttgart, Germany
[b] Institute for Pulsed Power and Microwave Technology, Karlsruhe Institute of Technology (KIT), Eggenstein-Leopoldshafen, Germany
[c] School of Resources and Environmental Science, Wuhan University (WHU), Wuhan, PR China
[d] Institute of Engineering Thermodynamics, German Aerospace Center (DLR), Cologne, Germany

HIGHLIGHTS

- The molten $MgCl_2$-KCl-NaCl salt was purified with an optimized Mg-additive method.
- The corrosion rates of Fe-based alloys were controlled under 15 μm/year in molten chloride salt at 700 °C.
- The corrosion development of Fe-based alloy was displayed during the 2000 h exposure test.

ARTICLE INFO

Keywords:
Concentrating solar power (CSP)
Thermal energy storage (TES)
Fe-based alloy
Salt purification
Mg corrosion inhibitor

ABSTRACT

Molten chlorides, such as $MgCl_2$-KCl-NaCl, are promising advanced high-temperature (up to 800 °C) thermal energy storage (TES) materials in next-generation concentrating solar power (CSP) plants. However, their high corrosivity to commercial Fe-Cr-Ni alloys impedes the commercial applications of chloride-TES. In this work, we investigated the corrosion of two selected commercial Fe-based alloys (SS 310 and In 800H) in molten $MgCl_2$-KCl-NaCl salt, aiming to study the feasibility of affordable Fe-based alloys instead of expensive Ni-based alloys in the chloride-TES system. The alloy samples were immersed in the liquid-Mg-purified molten salt at 700 °C for 2000 h under a protective inert gas atmosphere. After the corrosion test, SEM-EDX microstructural analysis and mass loss analysis showed that corrosion rates of the immersed alloy samples were lower than 15 μm/year, and the corrosion rates had a decreasing tendency with increasing immersion time during the 2000-hour test. To our best knowledge, this is the first experimental demonstration that corrosion rates of the Fe-based alloys in molten $MgCl_2$-KCl-NaCl salt at 700 °C can be controlled below the target (15 μm/year) proposed by the US Department of Energy (DOE). Using affordable Fe-based alloys as main structural materials, the cost of chloride-TES (27 USD/kWh) could be comparable to that of commercial nitrate-TES (20–33 USD/kWh). Taking advantage of chloride-TES with higher operating temperature, the next-generation CSP plant could use an advanced power cycle (e.g., sCO_2 Brayton) to have a much higher energy conversion efficiency, leading to a significantly lower Levelized Cost of Electricity (LCOE) than the current commercial CSP plant.

1. Introduction

In order to use the advanced supercritical carbon dioxide Brayton power cycle with high thermal to electric energy conversion efficiency, next-generation (Gen3) concentrating solar power plants require operating temperatures above 700 °C for TES materials and heat transfer fluids (HTFs) [1,2]. However, the nitrate salt mixtures (e.g., Solar Salt: $NaNO_3$-KNO_3 60–40 wt%) for heat storage and transfer in the current

☆ The short version of the paper was presented at ICAE2021, Nov 29 - Dec 5, 2021. This paper is a substantial extension of the short version of the conference paper.

* Corresponding author.
E-mail address: qing.gong@dlr.de (Q. Gong).

https://doi.org/10.1016/j.apenergy.2022.119708
Received 8 April 2022; Received in revised form 19 June 2022; Accepted 17 July 2022

CSP plants have limited operating temperatures of < 565 °C due to thermal decomposition [1,3,4]. Molten chlorides are promising high-temperature TES/HTF materials for the next-generation CSP plants due to high thermal stability (>800 °C) and low cost [5–8]. In addition, the molten chloride coolant is of interest in the nuclear field for next-generation molten salt reactors (MSRs) [9–13]. The $MgCl_2$-KCl-NaCl mixture is one of the most noticeable mixtures with the advantages of low melting point (~383 °C) [14], high thermal stability (stable above 800 °C) [7], low vapor pressure (~1 kPa at 800 °C) [7,14,15] and low cost (~0.22 USD/kg) [16]. In our previous work, eutectic $MgCl_2$-NaCl-KCl (47.1–30.2–22.7 mol.%, 56.5–22.2–21.3 wt%) is recommended as one of the most promising compositions, satisfying both cost-effective and low-melting-point requirements [7,17].

However, the compatibility issues, especially the severe corrosion of structural materials, make chloride salts challenging for high-temperature applications [1–2]. Molten unpurified $MgCl_2$-KCl-NaCl is strongly corrosive to Fe-Cr-Ni alloys even under an inert gas atmosphere [18–20], due to hydrolysis products, e.g., HCl and MgOHCl[15,21–28]. More about corrosion mechanisms and behaviours of alloys in molten chlorides could be found in our previous review paper [18]. In contact with the unpurified molten chloride salts, few Fe-Cr-Ni alloy can reach the target corrosion rate (CR) of <15 μm/year at 700 °C. This CR-target of 15 μm/year was proposed by the US Department of Energy (DOE) to achieve a service life of at least thirty years for structural materials in next-generation CSP [29].The CRs of Ni-based alloys in unpurified molten chloride salts are generally>100 μm/year at 700–800 °C, while CRs of Fe-based alloys (e.g., stainless steels) are even ten times higher than CRs of Ni-based alloys [13,18,30].

In addition to the high corrosivity of molten chlorides, the high costs of the Ni-based alloys limit their further application. The National Renewable Energy Laboratory (NREL) in the US estimated that if Haynes 230 (a commercial Ni-based alloy) is used as the main structural material of hot salt tank, the chloride-TES system would cost $58/kWh-th (US dollar per kWh in thermal), which is 2–3 times of that of the commercial nitrate-TES system ($20–33/kWh-th) [1]. The Ha 230 hot tank costs 70 % of the total cost ($41/kWh-th). It was pointed out that when stainless steel could be used as the main structural material of the hot tank, the cost of chloride-TES could be reduced to $27 /kWh-t. This cost would be similar to that of the commercial nitrate-TES [1]. Overall, a challenging but feasible way to achieve this cost target is to use Fe-based alloys as the main structural materials of chloride-TES under corrosion control.

One positive note is that the pure $MgCl_2$-KCl-NaCl mixture theoretically displays no spontaneous reactions (i.e., chemical corrosion) with Fe-Cr-Ni alloys even at high temperatures, based on thermodynamic data [31]. Hence, if the corrosive impurities, mainly MgOHCl, could be controlled at a low concentration level, the corrosivity of molten chloride salts to Fe-Cr-Ni alloys would be significantly mitigated [23,30,32–34]. A variety of methods have been explored to reduce the corrosive impurities in $MgCl_2$-containing chloride salts, including electrochemical methods [35,36], thermal methods [15,30,37,38], active-metal additive (e.g., Mg) [9,15,24,32,37–39], carbochlorination [9,40,41], and chlorination approaches [9,42]. Among them, Mg-additive is regarded as a low-cost and powerful way for purification of industrial salts on the 30 000-metric-ton scale [9,19,38], which is in line with the amount of nitrate salt in commercial 100 MW CSP plants [1,2]. In the previous work, with the removal of the main corrosive impurity MgOHCl by Mg addition, the CRs of some Ni-based alloys in $MgCl_2$-KCl (-NaCl) at > 700 °C can be tens of microns per year, which is close to the DOE's target (CR < 15 μm/year) [24,37,39,43]. The reaction of Mg with the main corrosive impurity in $MgCl_2$-KCl-NaCl is shown in **Eq. (1)**.

$$Mg_{(s/l)} + 2\ MgOHCl_{(l)} \rightarrow 2\ MgO_{(s)} + MgCl_{2(l)} + H_{2(g)} \quad (1)$$

On the other hand, active metal (e.g., Mg) can play the role of a corrosion inhibitor in chloride-TES. According to Ellingham Diagram [9,11,31], the Mg metal is more reactive than the main alloying elements in the Fe-Cr-Ni alloy in molten chloride salts. Thus, it could act as the sacrificial anode and react with corrosive impurities generated during operation. Our previous work shows that equilibrium concentrations of Cr^{2+}, Fe^{2+}, and Ni^{2+} in molten $MgCl_2$-KCl-NaCl with excessive Mg are extremely low, with values of 2.3×10^{-10}, 1.5×10^{-12}, and 8.5×10^{-15} mol.% at 700 °C, respectively [39]. In other words, the Fe-based alloys like stainless steels could theoretically exhibit acceptable low CRs in purified molten $MgCl_2$-KCl-NaCl with the Mg corrosion inhibitor.

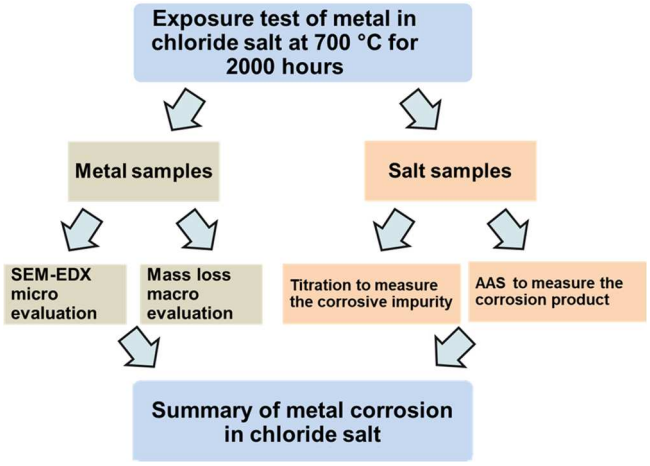

Fig. 1. Flowchart of the series experiments in this work. The corrosivity of salts and the corrosion of metal samples were evaluated separately.

Some austenitic alloys are of interest due to their relatively low costs and outstanding high-temperature mechanical properties, which make them promising candidates structural materials at > 700 °C [44–46]. Incoloy (In) 800H (EN 1.4876) and stainless steel (SS) 310 (EN 1.4845) are two commercial austenitic steels. Gilardi et al. reported that the cost of In 800H is about one-fourth of Ni-based alloys, while the cost of SS 310 is about the one-tenth cost of Ni-based alloys [47]. Therefore, if the CR of the Fe-based alloys in molten chloride salts can be controlled within the target (<15 μm/year) by an affordable means, the cost of chloride-TES will be comparable to the commercial nitrate-TES [1,16]. To our best knowledge, there is no literature experimentally demonstrating that a Fe-based alloy in $MgCl_2$-KCl-NaCl at 700 °C reaches the DOE's target (CR < 15 μm/year [29]), although this is theoretically possible. In the available literature [15,32,39], exposure experiments show that CRs of stainless steel are still > 50 μm/year even with the addition of excessive Mg.

This work aims to investigate if the Mg additive method can control the CRs of the commercial Fe-based alloys in molten $MgCl_2$-KCl-NaCl at 700 °C to reach the DOE's target (CRs < 15 μm/year). Fig. 1 presents the flowchart of the series of experiments in this work. Based on available literature and our previous work [15,32,39], the exposure test procedure was optimized by immersing the steel samples in the molten salt, which had been purified with liquid Mg. The SS 310 (1.4845) and In 800H (1.4876) were exposed in $MgCl_2$-KCl-NaCl for up to 2000 h (~2.8 months) at 700 °C with 2.8 wt% Mg under an inert atmosphere. After the exposure test, as can be seen in Fig. 1, the corrosion behavior of the metal samples was characterized via microscopic and macroscopic methods. The microscopic methods were scanning electron microscope (SEM), Energy-dispersive X-ray spectroscopy (EDX), and X-ray diffraction analysis (XRD), while the macroscopic method was mass-loss measurement. In parallel, corrosion impurity (MgOHCl) and corrosion products (e.g. Cr^{x+}, Fe^{x+}, Ni^{x+}) in the salt samples were also quantitatively analysed separately with acid titration and atomic absorption spectroscopy (AAS).

Table 1
Chemical compositions of the studied alloys (wt. %).

Alloy	Fe	Ni	Cr	C	Mn	Si	P	S	Al	Ti
SS 310	Bal.	19.00–22.00	24.00–26.00	0.25	2.00	1.50	0.045	0.030	–	–
In 800H	39.5	30.00–35.00	19.00–23.00	0.05–0.10	1.50	1.00	0.045	0.015	0.15–0.60	0.15–0.60

Data source: https://www.sandmeyersteel.com, access on February 9th of 2022.

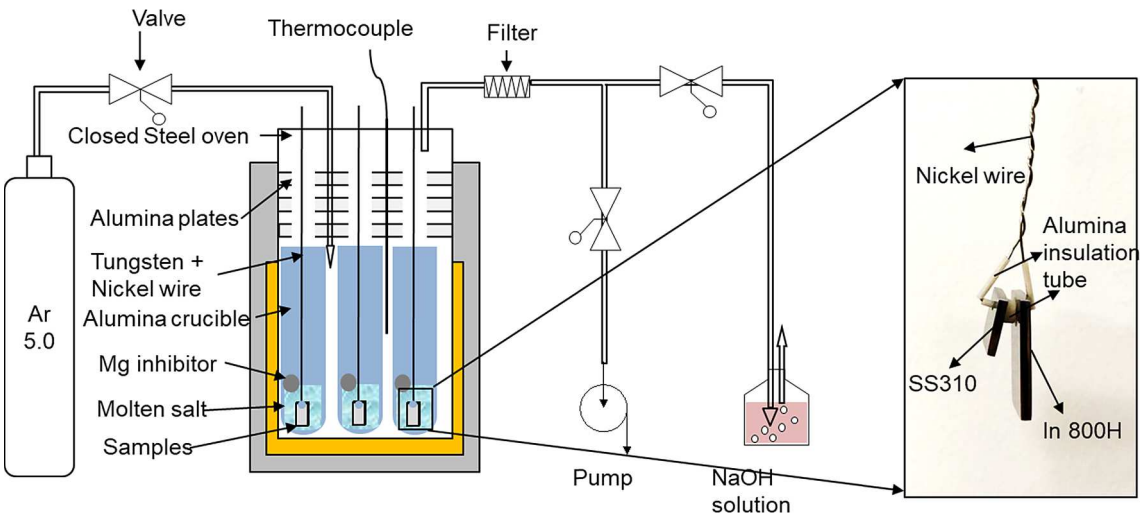

Fig. 2. Schematic diagram of experimental set-up for immersion test, and the sample holder with alloys samples.

2. Material and methods

2.1. Chemicals and alloys

Magnesium chloride ($MgCl_2$, Magnesia, purity > 99 wt%), potassium chloride (KCl, Alfa Aesar, purity > 99 wt%), and sodium chloride (NaCl, Alfa Aesar, purity > 99 wt%) were weighed, mixed, and grinded in a glovebox (GS^{TM}, O_2 < 0.5 ppm, H_2O < 1 ppm), to synthesize 300 g ternary eutectic $MgCl_2$-NaCl-KCl (47.1–30.2–22.7 mol.%) for the experiments [7]. Magnesium metal bars (Thermo Scientific, purity > 99.9 wt%) with 5 mm diameter were cut, polished, and weighed as the additive.

Table 1 summarizes the chemical compositions of two tested commercial Fe-based alloys SS 310 (1.4845) and In 800H (1.4876). Before exposure test, 10 × 10 × 2 mm SS 310 samples and 20 × 10 × 2 mm In 800H samples were polished successively with finer SiC sandpapers (600, 800, and 1200 grids) and washed with deionized water and dried with compressed air. Then the weight of each sample was recorded by an analytical balance with an accuracy of 0.0001 g.

2.2. Exposure test

Fig. 2 shows the set-up sketch of the exposure experiment. Six batches of 50 g salt containing 2.8 wt% Mg were dispensed into six

Table 2
Immersion corrosion test sample ID and corresponding test parameters.

Sample ID	Alloy	Duration of immersion hour	Sample size mm^3	Test condition	CR method
SS310-100h	SS 310 (1.4845)	100	10 × 10 × 2	Immersion in 50 g $MgCl_2$-NaCl-KCl (47.1–30.2–22.7 mol.%, 56.5–22.2–21.3 wt%) with 2.8 wt% Mg additive at 700 °C under 10 L/h Ar 5.0 sweep gas.	SEM-EDX + Mass loss
SS310-250h		250	10 × 10 × 2		SEM-EDX
SS310-500h		500	10 × 10 × 2		SEM-EDX
SS310-500h-2		500	10 × 10 × 2		Mass loss
SS310-1000h		1000	10 × 10 × 2		SEM-EDX
SS310-2000h		2000	10 × 10 × 2		SEM-EDX
In800H-100h	In 800H (1.4876)	100	20 × 10 × 2		SEM-EDX + Mass loss
In800H-250h		250	20 × 10 × 2		SEM-EDX
In800H-500h		500	20 × 10 × 2		SEM-EDX
In 800H-500h-2		500	20 × 10 × 2		Mass loss
In800H-1000h		1000	20 × 10 × 2		SEM-EDX
In800H-2000h		2000	20 × 10 × 2		SEM-EDX

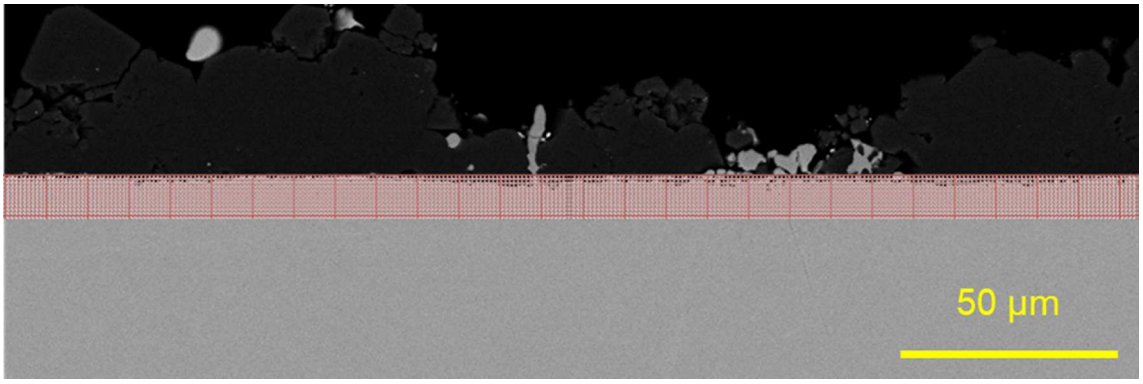

Fig. 3. Cross-section SEM image of SS 310-2000h sample with grids for calculation of the corrosion rate.

separate alumina crucibles in the glove box. The exposure time of the prepared salt in the air was<2 min to minimize the salt hydration during the transfer of salts from the glovebox to the test platform (autoclave). Then the test platform was heated to 700 °C under an inert atmosphere (Ar 5.0: purity ≥ 99.999 %, O_2 and H_2O < 1 ppm, flow rate: 10 L/h). After several-hour purification with liquid Mg at 700 °C, a batch of salt samples was withdrawn from each of the six independent crucibles for analysis. The six groups of alloy samples were then immersed into the purified molten salts in the six crucibles. As shown in Fig. 2, the alloy samples and nickel wire were separated by the insulating alumina tubes to prevent galvanic coupling due to direct contact between SS 310, In 800H, and the nickel wire. After 100, 250, 500, 1000, and 2000 h of exposure, the alloy samples were extracted from the furnace and cleaned with distilled water. Upon taking each alloy sample, the salt sample was subsequently withdrawn. The test conditions for different samples with specific sample identification (sample ID) are summarized in Table 2. The specific ID will be used throughout this work to denote the samples.

2.3. Alloy corrosion analysis

The corrosion condition of an alloy can be quantitatively evaluated by corrosion rate (CR) with unit microns per year (μm/year). One method of calculating CR is based on the mass change of samples before/after the exposure tests [15,18,43,48,49]. Under the hypothesis of uniform corrosion, the CR is calculated as **Eq. (2)** [48].

$$CR(\mu m/year) = \frac{K \times W}{A \times t \times \rho} \tag{2}$$

where,

K is a constant 8.76×10^7 ($\mu m \cdot h \cdot cm^{-1} \cdot year^{-1}$);
W is the mass loss of samples in g;
A is the sample's surface area in cm^2,
t is immersion time in hour;

ρ is the density of samples (g/cm^3). The density of SS 310 and In 800H is 7.89 g/cm^3 and 7.95 g/cm^3, respectively.

Before the mass-loss measurement of this work, the oxide films on samples were washed away according to the standard ASTM-G1 [48]. In this work, mass loss method was carried out on Samples SS310-100h, In800H-100h, SS310-500h-2 and In800H-500h-2. However, the mass-loss measurement has two drawbacks that lead to a biased view of corrosion state of the samples. Firstly, it is pointed out that the acid-washing could also damage the alloy matrix and thus cause over-estimation on corrosion rate [48]. Secondly, the mass-loss method cannot characterize the non-uniform corrosion such as intergranular corrosion. Intergranular corrosion can cause a significant corrosion depth even in case of a low mass loss, resulting in material failure. Therefore, the macroscopic corrosion analysis such as the mass loss method used in this work should be combined with the microscopic analysis method, to reduce the misjudgment of the corrosion state of the samples.

In this work, the CRs of alloy samples were also evaluated by the microstructural analysis with Scanning Electron Microscopy (SEM, model: Zeiss LEO 1530 VP), equipped with Electron Dispersive X-ray spectroscopy (EDX). In order to maintain the maximum integrity of the samples (especially oxide film on surfaces), the SEM samples were washed only with deionized water except for the acid-washed 100 h samples. As shown in Fig. 3, a 10-μm-thick-grid plot was put on the sample surface, divided into 1 μm × 1 μm small grids. The corroded grids (with the dark colour in SEM) were accounted for, while the CR was calculated according to Eq. (3) [23,30,39,50].

$$\boldsymbol{CR(\mu m/year)} = \frac{\boldsymbol{n_{cor}}}{\boldsymbol{W_{SEM}}} \times \frac{24 \times 365}{\boldsymbol{t}} \tag{3}$$

where,

n_{cor} is the total number of corroded 1 μm × 1 μm grids;
W_{SEM} is the width of the SEM image in μm (e.g., 274 μm for Fig. 3);
t is the immersion time in hour.

A typical phenomenon of the corrosion layer of Fe-Cr-Ni alloy in molten chloride salt is the Cr-depletion since Cr is the most active metal among the main alloying elements of Fe, Ni, and Cr [15,22,30,32]. In order to determine the depletion of Cr in the corrosion layer, EDX-mapping was carried out to measure the main elements in the alloy.

The surface compositions of exposed samples were analysed by SEM-EDX and X-ray diffraction (XRD, Seifert PAD II) with Cu Kα1 radiation (λ = 0.15406 nm, 40 kV, and 30 mA) in Bragg-Brentano geometry (θ-2θ) with a step size of 0.02° and a scan speed at 0.1°/min.

2.4. Salts analysis with titration and AAS

Before and after immersion of alloy, 2–3 g molten chloride salt samples were extracted. The acid-base titration was carried out to determine the concentration of corrosive impurities in experimental salts. It is well accepted that MgOHCl was the main corrosive impurity, as it has a high solubility in molten chloride salts [15,18,23,30]. All the titrations were performed on the high-precision titration instrument 905 Titrando (Metrohm GmbH, Germany). The titers of the standard titrants 0.01 M HCl (Merck KGaA, Germany) were validated with sodium carbonate (Na_2CO_3). About 500 mg salt sample was weighed and dissolved in 160 ml deionized water for each titration. During the titration, the N_2 sweep gas was employed to exclude the effect of carbon dioxide/carbonic acid. A 0.01 M HCl titrant was filled into the salt solution with an average 0.2 ml/minute rate. Simultaneously, a stirrer rotated continuously to make the solution homogeneous. A pH electrode measured the pH value of the salt solution. The pH value declined from ~ 9 to 4 with

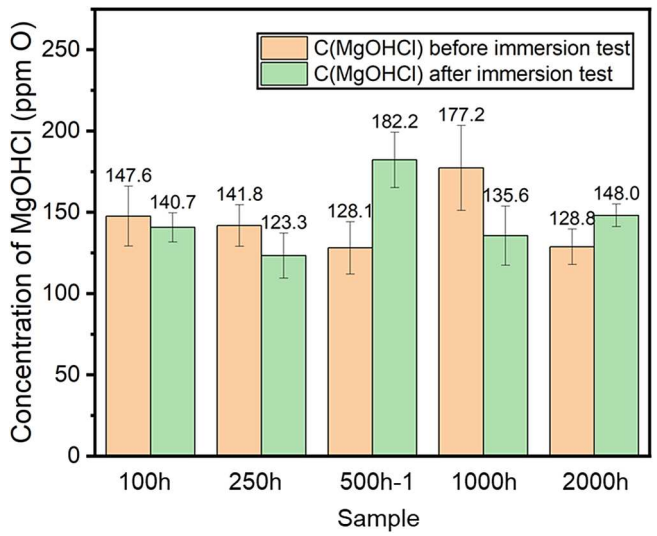

Fig. 4. Concentration of corrosive impurity MgOHCl in tested chloride salts before/after metal samples were immersed.

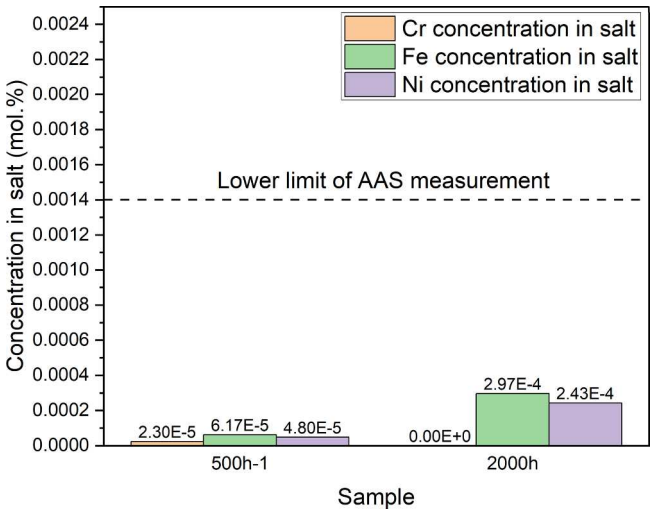

Fig. 5. The concentrations of Cr, Fe, and Ni in the molten chloride salt measured with AAS. The samples 500h-1 and 2000h mean the samples were extracted immediately after metal Samples-500h and −2000h, respectively. All the results are much lower than limit of AAS.

the filling of the HCl titrant. The HCl consumption at the equivalence point, where the amounts of acid and base were sufficient to cause complete neutralization, was recorded and used to calculate the impurity concentration. In order to obtain the mean value and standard deviation, each salt sample was titrated three times repeatedly. According to the consumption of 0.01 M HCl titrant at equivalence points, the concentration of the corrosive impurity MgOHCl with unit parts per million oxygen (ppm O) was calculated according to **Eq. (4)**. The unit ppm O is given to describe the proportion of the mass of the O-element in MgOHCl to the total sample mass [21,51]. One hundred ppm O means 0.048 wt% MgOHCl in samples.

$$\boldsymbol{C(MgOHCl)[ppmO]} = \boldsymbol{C_{HCl}} \times \boldsymbol{V_{HCl}}/\boldsymbol{m_{sample}} \times \boldsymbol{M_O} \times 1000 \quad (4)$$

where,

V_{HCl} is the volume of HCl at equivalence point in L;
C_{HCl} is 0.01× titer in mol/L;
m_{sample} is the mass of the salt sample in g;
M_O is the molar mass of oxygen, i.e., 16 g/mol.

Moreover, the concentrations of Cr, Fe, and Ni elements in salt samples were measured with an atomic absorption spectrometer (AAS, Thermo Scientific iCE 3000 series, Thermo Fisher Scientific, US). A hollow cathode lamp was employed as the radiation source. The currents of the lamp were 12 mA for Cr and 10 mA for Fe and Ni. The analytical lines with a spectral bandwidth of 0.2–0.5 nm correspond to the Cr at 357.9 nm, the Fe at 248.3 nm, and the Ni at 232.0 nm. The operational software Solaar AA Version 11.03 was integrated into the spectrometer, which can be used for signal evaluation and concentration calculation. The standard solutions with the concentrations of 1, 2, and 5 mg/l for Cr, Fe, and Ni were prepared by dissolving the chloride or nitrate salt in 100 ml distilled water and adding 1 ml 1 wt% HCl and 10 ml 10 wt% CsCl solution. During the AAS tests for salt samples, about 1000 mg salt samples were dissolved in the 100 ml distilled water with 1 ml 1 wt% HCl and 10 ml 10 wt% CsCl. The procedure of AAS experiments was in line with that in our previous work [39]. To obtain a lower limit for AAS measurements, the amount of salt sample in this work was ten times enlarged from 100 mg to 1000 mg. With this amount of salt samples, the measurement limits of AAS are 1.52×10^{-3} mol.% for Cr, 1.41×10^{-3} mol. % for Fe, and 1.35×10^{-3} mol.% for Ni, respectively.

3. Results

3.1. Concentration of impurities in experimental salt

For evaluating the corrosivity of experimental molten chloride salts, the concentration of corrosive impurity MgOHCl in molten chloride salts in this work was determined by acid-base titration. After 16-hour pretreatment with liquid Mg, i.e., before the exposure test of alloy samples, salt samples were extracted from each crucible. In addition, shortly after the exposure test of each alloy sample, the salt samples were extracted as well for post titration. Fig. 4 exhibits the concentration of the corrosive impurity (MgOHCl) in molten $MgCl_2$-KCl-NaCl mixtures before and after alloy immersion measured by titration, in which the error bars are the standard deviation of three-time titrations. In general, it can be concluded that the concentrations of MgOHCl in $MgCl_2$-KCl-NaCl mixtures purified with liquid Mg were lower than 200 ppm O (i.e., < 0.096 wt%) during exposure test of alloys.

The different operation durations could cause the fluctuation of MgOHCl concentration in sampling. A small amount of air inevitably diffused into the autoclave during the sampling. This leads to a reaction of the $MgCl_2$ with moisture in the leaked air, as shown in **Eq. (5)**. The longer the sampling continued, the more MgOHCl was produced. The duration of sampling varied within one minute, resulting the inconsistent concentration of MgOHCl from 123.3 ppm O to 182.2 ppm O as shown in Fig. 3.

$$MgCl_2{\cdot}H_2O_{(l/s)} \rightarrow \mathbf{MgOHCl}_{(s)} + HCl_{(g)} \quad (5)$$

The concentrations of Cr, Fe, and Ni in all salt samples are smaller than their measurement limits of AAS, as shown in Fig. 5. In other words, the corrosion products in molten chloride salt are smaller than 1.52×10^{-3} mol.% after the 2000 h corrosion test. Based on such low concentrations of MgOHCl and corrosion products in salt samples, it is believed that the corrosivity of the purified molten chloride salts was controlled successfully.

3.2. Surface characterization of exposed alloys

Fig. 6 shows the surface morphologies and the corrosion products of the exposed alloy samples. The optical pictures of the samples exposed for 250 h and 2000 h are shown in Fig. 6 (h). The sample exposed for 2000 h shows the black color, and its surface is covered with some particles. Fig. 6 (a) – (f) display the SEM images and corresponding EDX-

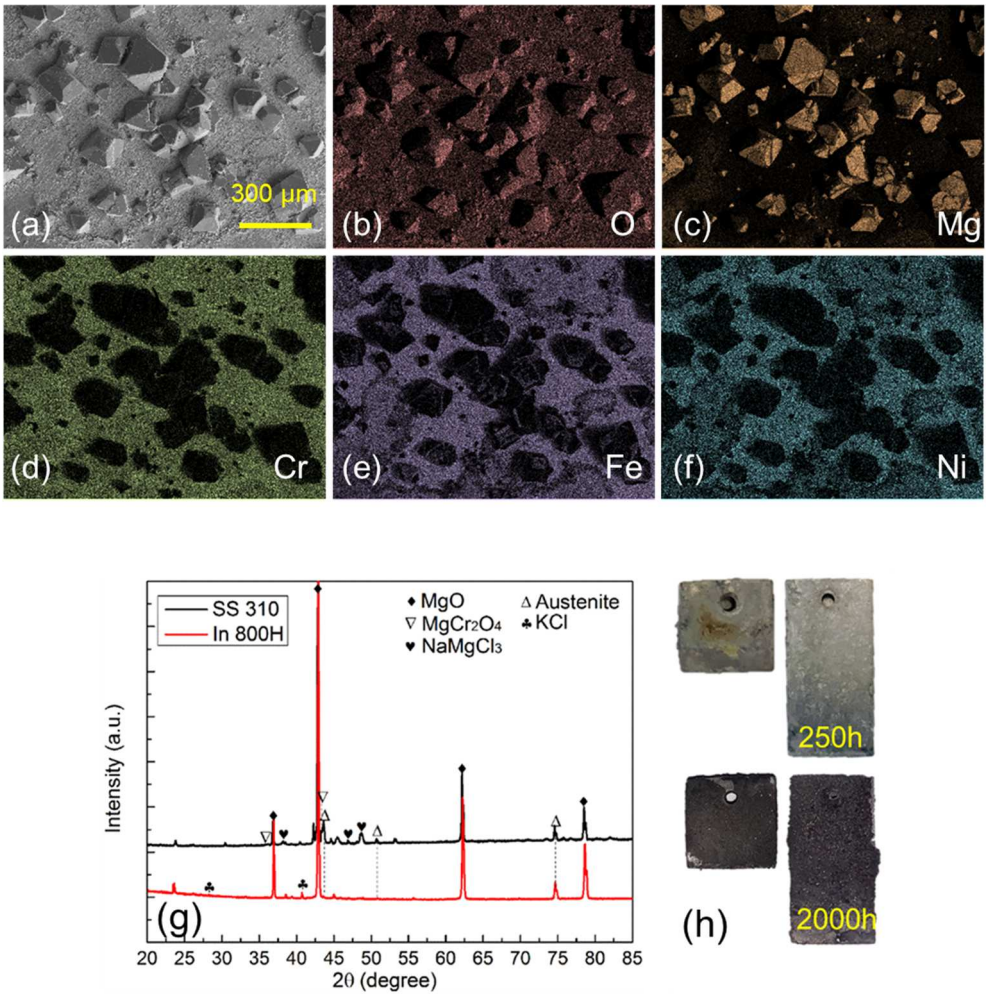

Fig. 6. (a) SEM image and (b)-(f) corresponding EDX-mappings of SS 310-500h sample surface. (g) XRD pattern of Samples SS310-1000h and In800H-1000h sample surfaces. (h) optical pictures of 250 h and 2000 h samples after test (SS 310: 10 × 10 × 2 mm, In 800H: 20 × 10 × 2 mm).

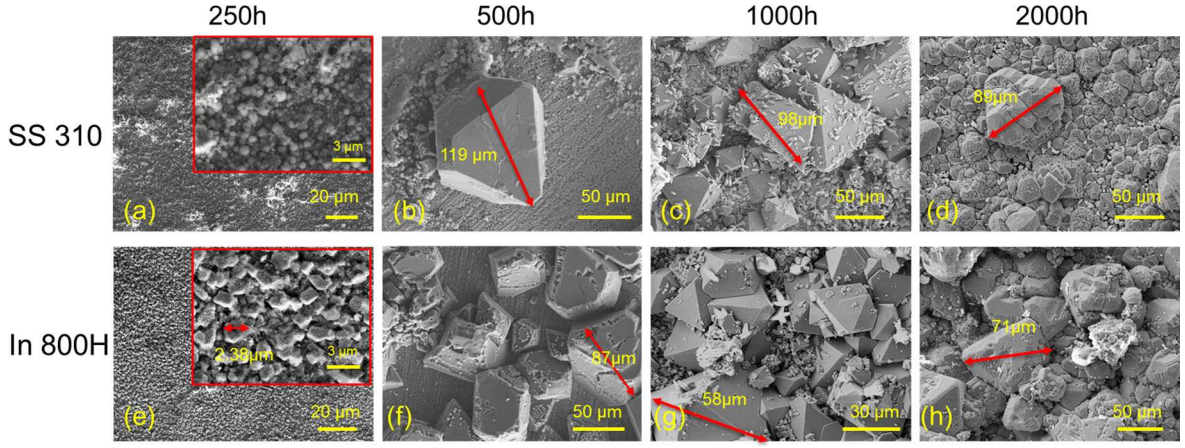

Fig. 7. Development of MgO morphology at the surface of metal samples during the 2000 h exposure test in $MgCl_2$-KCl-NaCl at 700 °C under Ar, characterized by SEM.

mapping of Sample SS310-500h. Surface images of Sample SS310-500h show some tetrahedral crystal particles. According to the corresponding EDX-mapping, the particles are enriched in Mg and O.

The phase compositions of the species on the surfaces of Samples SS310-1000h and In800H-1000h were examined by XRD, as shown in Fig. 6 (g). For both SS 310 and In 800H, the diffraction reflections of MgO at $2\theta = 37.1°$, 42.6°, and 62.5° are dominant. In addition, the austenite phase was detectable in the XRD patterns of both studied Fe-based alloys, which indicates the surfaces of both samples were not fully covered by oxide precipitations after 1000 h exposed to molten chloride salt. Moreover, the XRD pattern of the Sample SS310-1000h shows a slight signal of $MgCr_2O_4$. In contrast, no reflection of

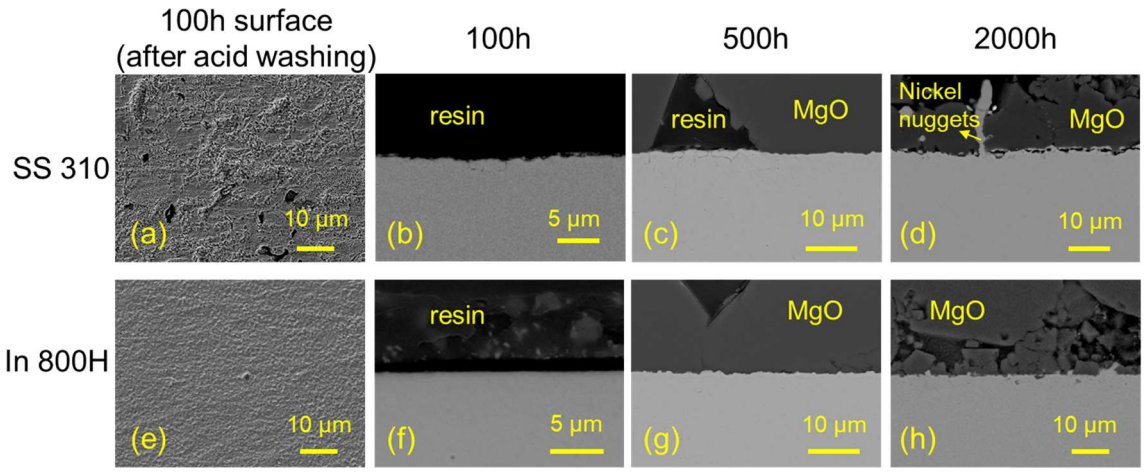

Fig. 8. Development of corrosion morphology of alloy samples during the 2000 h exposure immersion test in $MgCl_2$-KCl-NaCl at 700 °C under Ar, characterized by SEM on their cross-sections.

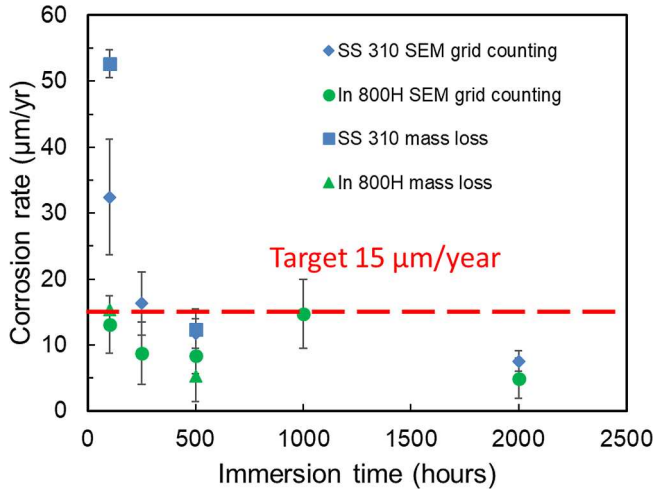

Fig. 9. Corrosion rates of SS 310 and In 800H based on SEM-grid-counting and mass loss results as a function of the immersion time.

$MgCr_2O_4$ was detected on Sample In800H-1000h. Based on the SEM-EDX and XRD results, MgO is the dominant deposit on the surface of both SS 310 and In 800H. Fig. 7 shows the evolution of surface morphologies of SS 310 and In 800H samples during exposure to Mg-additive chloride salt for 2000 h. After 250 h, small size MgO particles (size of < 3 μm) were aggregated on the surface of SS 310 and In 800H (Fig. 7 (a) and (e)), followed by MgO crystal particles with the size of tens of micrometre eventually covering the entire surface (Fig. 7 (d) and (h)). The growth process of MgO on SS 310 and In 800H samples was similar during the 2000 h-immersion test.

3.3. Corrosion evolution of alloys in molten chloride salt

The mass losses of Samples SS310-100h and In800H-100h were recorded after descaling according to the ASTM-G1 standard [48]. As shown in Fig. 8 (a) and (e), no residual oxide layer can be observed on the surfaces of Samples SS 310–100h and In 800H-100h after descaling, confirming the acid washing can erase the oxide layer. According to the mass loss of Samples SS310-100h, In800H-100h, SS310-500h-2, and In800H-500h-2, the $CRs_{(mass\text{-}loss)}$ of the studied alloys are calculated based on Eq. (2). The $CRs_{(mass\text{-}loss)}$ of SS 310 are 52.6 ± 2.11 and 12.4 ± 0.38 μm/year for 100 h and 500 h, respectively, while $CRs_{(mass\text{-}loss)}$ of In 800H are 15.3 ± 2.11 and 5.3 ± 0.38 μm/year, respectively. The error here originates from the measurement limit of the balance.

Fig. 8 displays the development of corrosion morphology of tested samples during the 2000 h-exposure test in the purified $MgCl_2$-KCl-NaCl molten salt at 700 °C under Ar sweep gas. On most of the SEM images, only thin corrosion layers can be observed. According to grid counting on SEM images mentioned in Eq. (3) and Fig. 3, the CRs of samples were calculated and summarized, as shown in Fig. 9. The corrosion depths of SS 310 and In 800H are notably small (1.73 ± 0.36 μm for SS 310 and 1.13 ± 0.5 μm for In 800H) after 2000-hour immersion, suggesting that $CRs_{(grid\text{-}counting)}$ are 7.6 ± 1.6 μm/year and 4.9 ± 2.2 μm/year of SS 310 and In 800H, respectively. The error here originates from the standard deviation of corrosion depth of three different parts for the same sample. Since the corrosion depth is limited, the position of the sample

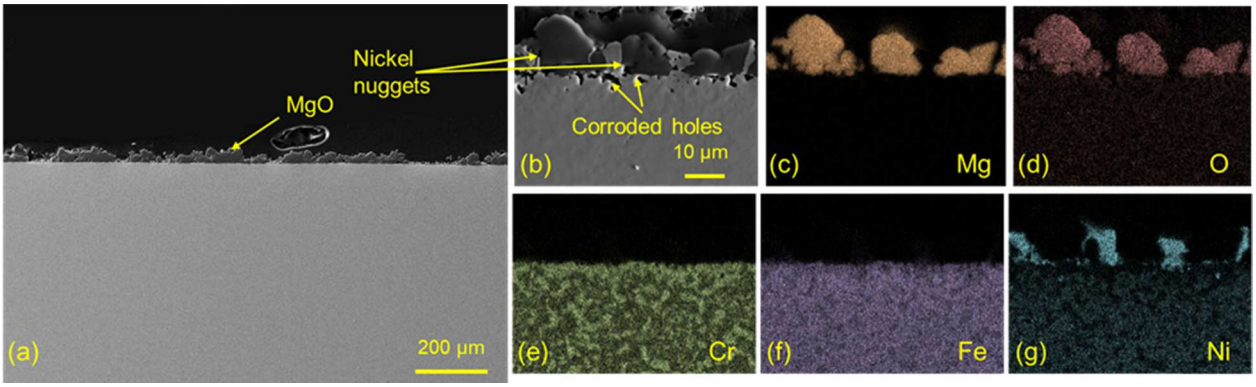

Fig. 10. Cross-section SEM and EDX-mapping images of Sample SS 310-2000h.

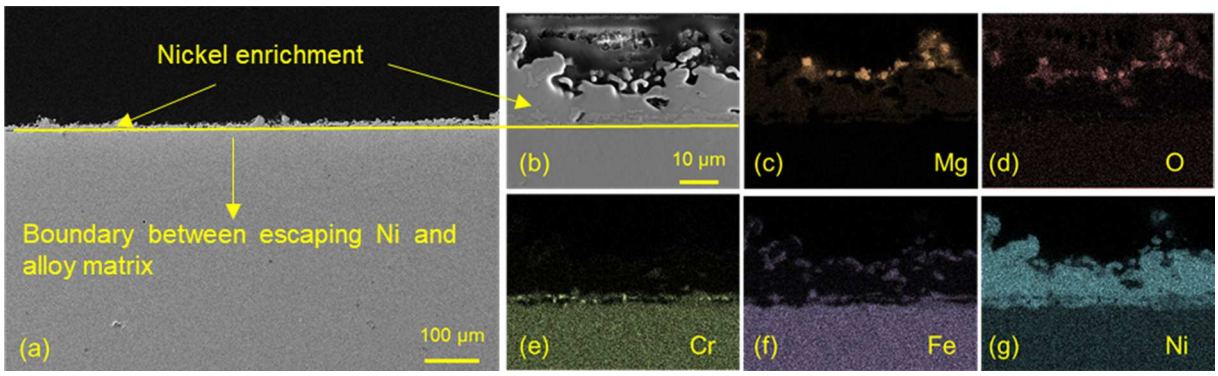

Fig. 11. Cross-section SEM and EDX-mapping images of Sample In800H-2000h.

embedded in the resin and the initial surface roughness of the sample affected the CR calculation significantly, leading to high relative errors in CRs. Overall, the CRs from grid counting and mass loss are comparable under identical experimental conditions (see Fig. 9). The CRs of both SS 310 and In 800H show a decreasing tendency with increasing exposure time. For example, the CR of SS 310 decreases from ~ 53 μm/year to < 10 μm/year with increasing immersion time from 100 h to 2000 h.

Fig. 10 and Fig. 11 provide SEM images of 2000-hour-sample cross-sections and elemental analysis by EDX-mapping. As shown in Fig. 10 (a), a non-uniform MgO layer with a thickness of about 80 μm was observed on the surface of SS 310. The corrosion layer was almost invisible. The enlarged SEM image and EDX-mapping of the corrosion layer of SS 310 are shown in Fig. 10 (b)-(g). Some small holes with an average depth of 3 μm beneath the MgO layer were observed. From the EDX-mapping images, chromium distributes in the matrix unevenly. In addition, there exists some nickel enrichment at the surface of the sample and depletion in the matrix simultaneously.

For Sample In800H-2000h, some parts of its surface were also covered with MgO (as shown in Fig. 8 (h)), while another typical surface feature is covered with Ni enrichment (as shown in Fig. 11 (g)). In contrast to the nugget shape on Sample SS310-2000h, the Ni-enrichment on Sample In800H-2000h exhibits a relatively uniform and continuous layer. Besides Ni, few other matrix elements such as Fe and Cr were measured by EDX. Furthermore, the Cr distribution in Sample In800H-2000h is more uniform than that in Sample SS310-2000h. The corrosion layer is also barely visible on sample In800H-2000h and exhibits a thickness below 2 μm. For Samples SS310-2000h and In800H-2000h, no typical Cr-depletion layer was observed by EDX-mapping. Because the Cr-depletion is a typical feature of corroded Fe-Cr-Ni alloy in molten chloride salts [15,30,32], the little-Cr-depletion indicates that the corrosion on the 2000 h-samples is slight.

4. Discussion

4.1. Development and influence of MgO layer

It is reasonable to assume that there are two sources of MgO in the presented experiments, as discussed in our previous work [30]. On the one hand, formed MgO was originated from the spontaneous decomposition of MgOHCl, which was generated from the hydrolysis of hydrated $MgCl_2$ such as $MgCl_2{\cdot}H_2O$, as shown in **Eq. (6)** [25,27,30]. On the other hand, both alloying elements in specimens (e.g., Cr) and inhibitor Mg react with the dissolved MgOHCl impurity in the molten salt, leading to the formation of the MgO layer on the surface of samples, as shown in **Eq. (7)**. In contrast to the previous work with a clear signal of $MgCr_2O_4$ [23,30], a weak signal of $MgCr_2O_4$ was detected by XRD in this work, while no Cr signal was detected with EDX in the oxide layer, indicating that Cr-depletion was too little from the alloy to form Cr-rich oxide. The

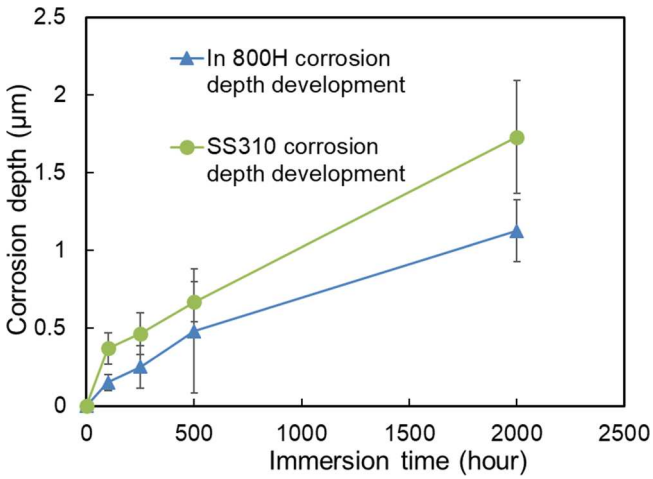

Fig. 12. SS 310 and In 800H corrosion development in $MgCl_2$-KCl-NaCl at 700 °C under Ar sweep gas. The salts were purified with 2.8 wt% Mg at 700 °C for 16 h before tests.

little Cr-rich oxide is a sidelight of the low-level corrosion in this work.

$$MgOHCl_{(s)} \rightarrow \mathbf{MgO}_{(s)} + HCl_{(g)} \quad (6)$$

$$M_{(Mg,\ Fe,\ Cr,\ Ni)} + 2MgOHCl(l) \rightarrow 2\mathbf{MgO}_{(s)} + MCl_2 + H_{2(g)} \quad (7)$$

As displayed in Fig. 7, the MgO grew gradually on the surface of samples during the 2000 h-exposure test. It is foreseeable that without any actions, a dense MgO layer would also grow on the structural material in the future applications of chloride-TES. Although it makes sense in principle that a dense and continuous MgO layer could inhibit the attack of MgOHCl on the alloy by acting as a barrier, there is no direct evidence that the MgO layer on the alloy sample is dense enough to inhibit the attack of MgOHCl. In the previous work [23,24,30,39] with significantly thick MgO layer, the corrosion layers in the matrix are still as high as tens of microns in molten chloride salt. In the present work, even for the same sample (e.g., Sample In800H-2000h), the distribution of the MgO layer is unevenly distributed. A part of the sample surface was covered by the MgO layer, as shown in Fig. 8 (h), while a part of the sample surface was covered by Ni-enrichment, as shown in Fig. 11 (a). However, the corrosion depth under these two types of surfaces is equally tiny, implying that the corrosion layer depth has no significant relationship with the MgO layer in this case. However, blockages or performance drop caused by MgO in the cycle of chloride-TES might lead to high operating cost. Hence, the large particle and thick layer of MgO in the cycle of the system are potential risks. Some filters reported in reference [15] can be employed to remove MgO particles out of the molten salt and solve such problems.

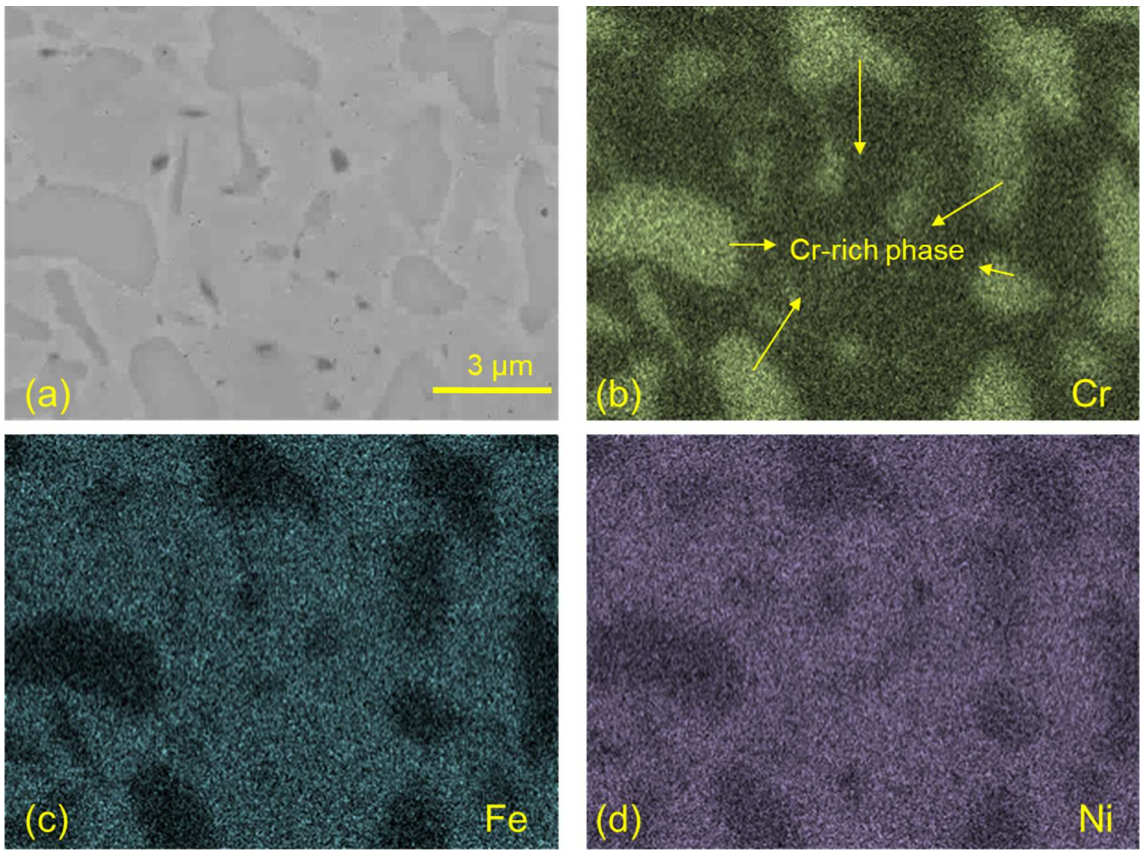

Fig. 13. SEM and EDX-mapping images of Sample SS 310-2000h in the deep matrix. Cr-rich phase is observed.

4.2. Corrosion of Fe-based alloys in molten chloride salt at 700 °C

The presented results experimentally prove that Fe-based alloys can reach the target of 15 μm/year proposed by DOE [29] in $MgCl_2$-KCl-NaCl mixtures at 700 °C with Mg salt-purifier and corrosion-inhibitor. Firstly, according to the corrosion results (Fig. 9), the CRs based on mass loss and microstructural analysis of 500–2000 h samples are always smaller than 15 μm/year. Secondly, almost no Cr-depletion can be observed from EDX mapping, which confirms the low CRs of the alloy samples. In addition, the MgO is the dominant component of the oxide layer, while very weak Cr-enrich oxide was detected, which confirms again that the Cr-depletion from the matrix is small. The target of 15 μm/year means that the corrosion depth of the primary structural material will be<0.5 mm, after 30 years of operation.

Fig. 12 shows the corrosion-depth development of the samples with different exposure times. As can be seen, the corrosion depth increases sharply in the first 100 h of tests, while after 250 h, the corrosion curve is relatively flat. The corrosion development of SS 310 and In 800H in molten chloride salt in this work is comparable to that of Inconel 600 used in fluoride loop in the literature [52] (Figure 12.1 in [52]). In the long-term corrosion test of the fluoride loop, the rapid corrosion of the first 250 h is the initial impurity-driven corrosion. In comparison, the slow corrosion after 250 h was a thermal gradient effect resulting from the metal solubility difference in molten fluoride salt at different temperatures and parts [52].

Although the corrosion curves of previous and this work are comparable, the explanations of corrosion in that dynamic fluoride loop and this static chloride test are not in line. There exists no thermal-gradient-effect corrosion in this static corrosion test. The impurities (e.g., MgOHCl) drove the corrosion of samples in this work. As shown in Fig. 4, the concentration of the main corrosive impurity MgOHCl was at a similar level, i.e., < 200 ppm O in separate crucibles after various exposure times. Hence, it is probable that the variation of CRs is not attributed to the concentration difference of MgOHCl. A possible cause of the relatively high mass loss in the early stage could be the rapid passivation of the bare metal after polishing. After that, corrosion would be controlled by diffusion of the alloying elements involved in the corrosion reactions, which was slower.

The estimated CRs of alloy in molten chloride salt in this work are low, however, the problem of Ni-enrichment on the surface is noteworthy, as shown in the EDX-mapping of Samples SS310-2000h and In800H-2000h (i.e., Fig. 10 (g) and Fig. 11 (g)). This phenomenon is particularly evident in the Sample In800H-2000h, which shows a continuous Ni-enrichment layer with a height of 20 μm. One plausible explanation for this is that the Ni in the sample matrix has a high affinity with the Mg metal dissolved in molten chloride salt. The Mg-Ni interaction phenomenon was also observed by other researchers in corrosion tests of Fe-Cr-Ni alloys with Mg-rich molten chloride salts [22,43,53]. The research on Mg-Ni interaction is insufficient and requires further investigation.

Another noteworthy point from EDX-mapping is inhomogeneous Cr-distribution in SS 310 after 2000 h exposure to molten salt at 700 °C, as shown in Fig. 10 (e). This inhomogeneity is not due to the impact of molten chloride but the segregation of Cr in SS 310 at 700 °C. The following two reasons are given to support this view. Firstly, the inhomogeneous Cr distribution in SS 310 after 2000 h exposure is observed not only near the surface but also in the deep matrix (see Fig. 13). In the deep matrix that was inaccessible to the melts, only high temperature can affect the distribution of Cr. Secondly, in literature [54,55], the austenitic stainless steels were tested/in service at temperatures above 600 °C without molten salt. In these cases, Cr-rich secondary phases, such as the sigma phase, were presented at grain boundaries (GBs), leading to the inhomogeneous Cr distribution. The embrittle sigma phase precipitates at GBs, leading to the degradation of these steels'

Table 3
Comparison of CRs for Fe-based alloys in $MgCl_2$-containing molten salt at 700 °C under inert atmosphere.

Materials	Purification method	Immersion time hour	Salts	CR based on mass loss μm/year	CR based on SEM-EDX μm/year	Data sources
SS 310	–	500	$MgCl_2$-KCl-NaCl	1581[a]	1752	DLR [30]
In 800H				364[a]	876	
SS 310	Adding 1 wt% Mg			–	298	DLR [39]
In 800H				–	262	
SS 310	Salt pre-treatment by 2.8 wt% liquid Mg + test with excessive Mg	500		12.4[a]	~12[b]	This work
In 800H				5.3[a]	~8[b]	
SS 316	Salt pre-treatment by solid Mg and test with 1 wt% Mg	400		51	~ 20 μm corrosion along grain boundary after 400-hour test	CAS [32]
SS 316 (carburized)				52	~ 60 μm corrosion along grain boundary after 400-hour test	
SS 316	Salt dried at 300 °C for 24 h	100		261	~ 50 μm corrosion along grain boundary after 100-hour test	CAS [20]
SS 316 L	Salt pre-treatment by CCl_4 bubbling	100	$MgCl_2$-KCl	18	almost invisible	ORNL [35]

[a] For mass loss measurement, the samples were washed by acid according to ASTM G1 [48].
[b] Errors of these values are high because of almost invisible corrosion layers on samples, as shown in Fig. 8 (c), (g) and Fig. 14 (c).

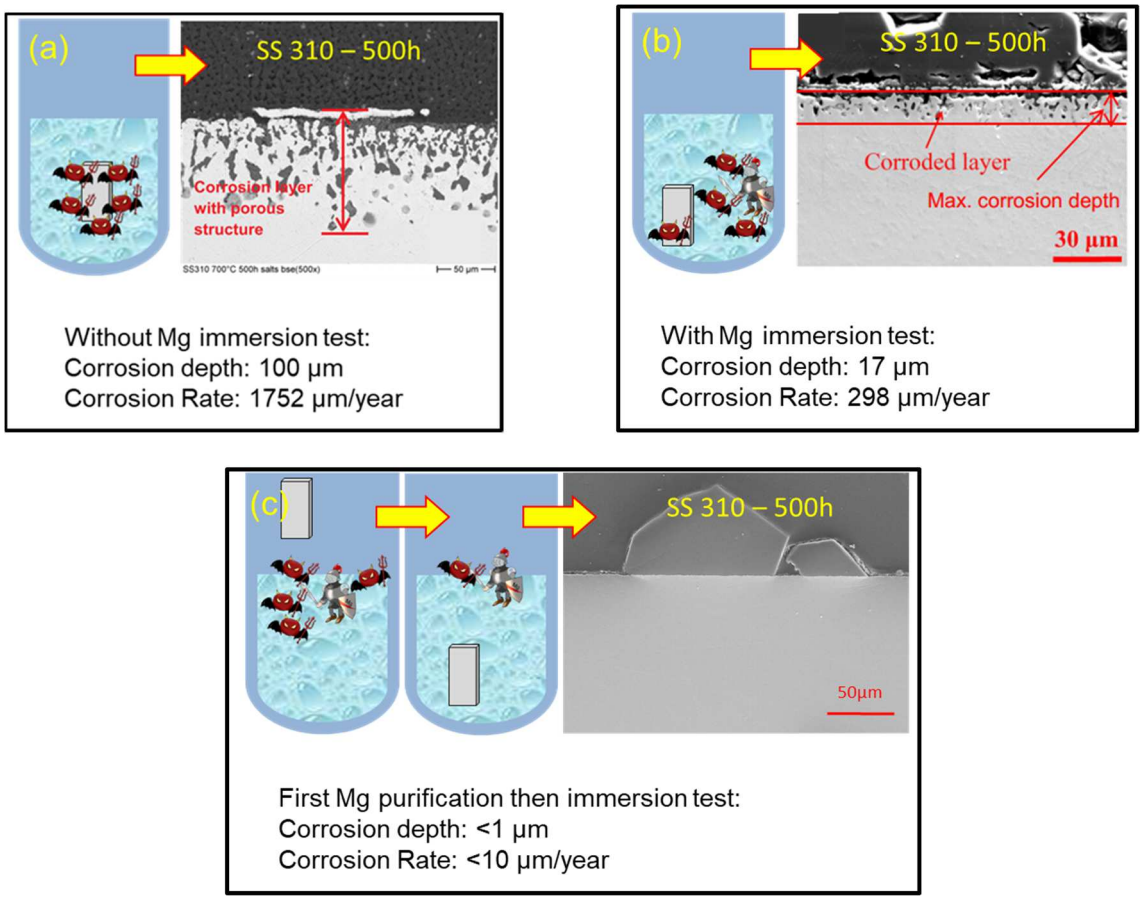

Fig. 14. Comparison of three exposure tests at DLR. The tests were performed at the same platform with $MgCl_2$-KCl-NaCl at 700 °C under Ar sweep gas. (a) SS 310 was heated with the impurified salt to 700 °C and held for 500 h [30]; (b) SS 310 was heated with salt and 1 wt% Mg to 700 °C and held for 500 h [39]. (c) In this work, the salt was purified with 2.8 wt% liquid Mg at 700 °C for 16 h, and then the SS 310 was immersed in purified salt. Red devil: MgOHCl; Knight: Mg metal. (For interpretation of the references to color in this figure legend, the reader is referred to the web version of this article.)

mechanical properties (especially anti-creep property) at high temperatures [56], indicating that the 700 °C seems not the optimum service temperature of SS 310. For the future application of chloride-TES tank, stainless steels with better thermal stability at > 700 °C are required, which should have reasonably high-temperature mechanical properties, especially anti-creep properties [57].

4.3. *Influence of purification methods on CRs of Fe-based alloys*

The purification method is essential for the corrosion control. It was pointed out that the corrosion products can accelerate the corrosion of metal matrix in molten chloride salt [28]. The purification strategy is therefore crucial, as it affects the initial conditions of corrosion.

Table 3 summarizes the CRs of Fe-based alloys in $MgCl_2$-containing molten salt at 700 °C under an inert atmosphere, including the results

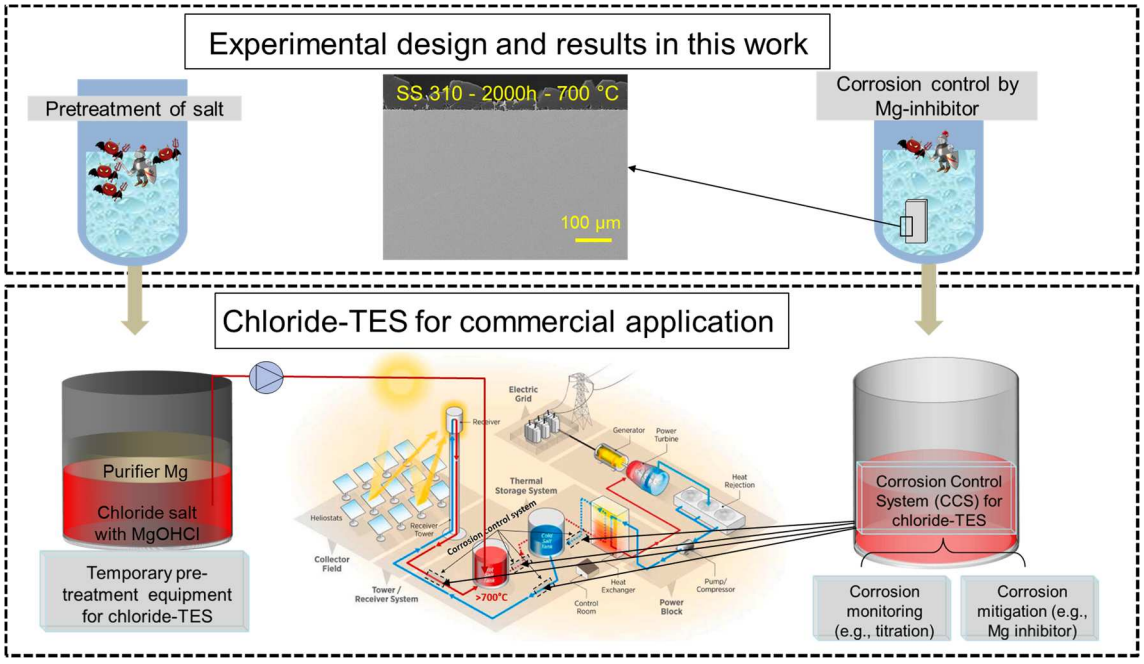

Fig. 15. Industrial procedure of chloride-TES for commercial application in CSP designed based on the results in this work.

from the Chinese Academy of Sciences (CAS) [32], the Oak Ridge National Laboratory (ORNL) [40], our previous work [30,39], and this work. All the molten chloride salts were chemically purified, except for the molten chloride salts employed in ref. [30] not purified with any chemical methods, in which the CR of SS 310 is 1752 μm/year as a reference.

Kurley et al. from ORNL purified 600 g $MgCl_2$-KCl salt with CCl_4 bubbling at 850 °C for over 100 h [40]. Then SS 316 L samples were immersed in purified salt for 100 h at 700 °C. Based on the mass-loss measurement, the CR of SS 316 L was about 18 μm/year in this case, implying that intensely chemical pre-treatment is an effective method to decline the corrosivity of molten chloride. However, due to its expensive cost and toxicity, the CCl_4 bubbling method could be challenging for large-scale purification.

In our previous work [39], Mg (1 wt%) was used as the additive to mitigate molten chloride salt corrosion of alloy samples. During the heating, however, some produced corrosive impurities like MgOHCl and HCl, before reacting with Mg, corroded the SS 310 sample, leading to a 17 μm corrosion layer in 500 h immersion test (298 μm/year) [39]. Ren et al. in CAS used a Mg rod to purify $MgCl_2$-KCl-NaCl at 600 °C for 24 h [32]. After purification, standard SS 316 and carburized SS 316 samples were immersed into purified salt with 1 wt% Mg for 400 h at 700 °C. Although the mass loss results imply that the CRs of samples were not severe (~51 μm/year), the corrosion depth at the cross-section measured by SEM was relatively high due to intergranular corrosion. The passivation of the Mg rod by the MgO layer (see **Eq. (1)**) could result in the corrosive impurities were not reduced to a low level, leading to relatively large intergranular corrosions.

As shown in Fig. 14, sketches of three corrosion experiments performed at the German Aerospace Center (DLR) are summarized. In this work, the alloy samples were immersed in molten chloride salts at 700 °C, pre-treated by 2.8 wt% liquid Mg for 16 h. With this approach, the concentration of MgOHCl in this work is controlled under 200 ppm O, while the concentrations of Cr, Fe, and Ni were smaller than 1.52×10^{-3} mol.% in melts, resulting in the CRs being smaller than 15 μm/year. Furthermore, with a suitable corrosion inhibitor, the CR decreases with the increasing test time, as shown in Fig. 9.

According to the experience learned from this work, an industrial procedure similar as that for the commercial molten nitrate-TES system could be designed for the molten chloride-TES system, as schematically shown in Fig. 15. Based on the promising salt purification effectiveness of Mg in this work, an equipment (similar as the commercial pre-melting equipment for nitrate salts [58]) is patented [59] and will be developed for pre-melting and salt purification with Mg. After pre-melting and salt purification, the molten chloride salt will be pumped to the commercial salt tank of the CSP plant. During the operation of the CSP plant, the molten chloride flows in the molten chloride TES system. The corrosion control system (CCS) in the chloride-TES is necessary for the 30-year service life of CSP [7]. The CCS consists of two parts: corrosion monitoring and corrosion mitigation. In this work, the corrosion monitoring part corresponds to the titration and AAS methods, giving ex-situ analysis of the salt corrosivity (e.g. MgOHCl concentration) and corrosion products. Besides the ex-situ analysis, some in-situ techniques based on some electrochemical methods (e.g., CV [21,60,61] and OCP [61]) could be used for online monitoring. In this work, the Mg metal plays two roles as both salt purifier before metal exposure and corrosion inhibitor during the 2000-hour test. In other words, the Mg metal could be also used as a corrosion inhibitor in CCS for corrosion mitigation. Except for Mg-inhibitor, other options such as electrolysis [36] could be used for corrosion mitigation. With the procedure described in Fig. 15 based on the promising results of this work, the corrosion rate of stainless steel in chloride-TES for commercial application in CSP could be controlled at a low level. However, static experiments on a laboratory scale cannot fully reflect the real situation in the industry. Therefore, subsequent study closes to the real conditions of CSP based on dynamic platforms is necessary for reducing the scaling-up risk of chloride-TES.

4.4. Economic discussion on the chloride-TES

The corrosion of molten chloride salt to Fe-Cr-Ni alloy has long been one of the most challenging issues for molten chloride salt [1,18,20,43,62]. It is the prerequisite for the application of molten chloride salts to overcome the high corrosivity with a cost-effective approach, especially for the next-generation CSP with up to 30000-ton salt. In this work, we purified the inexpensive salt ($MgCl_2$-KCl-NaCl) with an inexpensive method (Mg-additive), controlling the corrosion rates of inexpensive alloys (Fe-based alloys) under 15 μm/year in molten chloride salt at 700 °C for 2000 h.

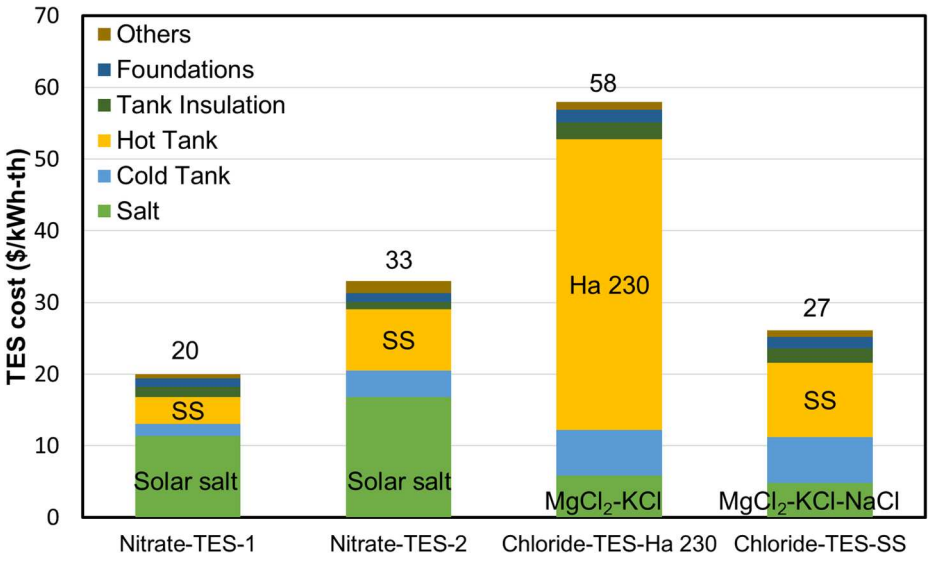

Fig. 16. A comparison of cost of commercial nitrate-TES with estimated chloride-TES [1]. When the stainless steel could be available in chloride-TES, the cost of chloride-TES would be in line with nitrate-TES.

The positive results of the static corrosion test suggest that stainless steel is a promising candidate for structural material for chloride-TES, which is in line with the main structural material for commercial nitrate-TES. Fig. 16 shows the cost comparison of nitrate- and chloride-TES. Among them, the costs of Nitrate-TES-1 (commercial case: Abengoa GO 18149, 20 $/kwh-th), Nitrate-TES-2 (commercial case: Worley-Parsons, 33 $/kwh-th), and Chloride-TES-Ha 230 (estimation, 58 $/kwh-th) are available in the report published by the NREL [1], while the cost of Chloride-TES-SS (27 $/kwh-th) is estimated based on stainless-steel hot tank and $MgCl_2$-KCl-NaCl ternary chloride salt using the estimation model in the report of NREL. In the Chloride-TES-SS, the cost of the hot tank was estimated by generalizing the hot tank in Chloride-TES-Ha 230. The Ha 230 hot tank costs 70 % of total TES, i.e., 41 $/kWh-th. The cost of the nickel-based alloy is about 10 times higher than stainless steel [47], but nickel-based alloy shows 2.5 times better mechanical properties at 700 °C[63]. Hence the cost of the hot tank of Chloride-TES-SS is estimated by (41/10) * 2.5 = 10.25 $/kWh-t. The stainless-steel hot tank leads to a sharply decreasing chloride-TES cost, resulting in a comparable cost with commercial cases of nitrate-TES.

5. Conclusions and outlook

The main conclusions of this work are summarized as follows:

- Based on the 2000-hour exposure test, the corrosion rates of In 800H and SS 310 in the molten $MgCl_2$-KCl-NaCl salt purified with liquid Mg at 700 °C under the Ar atmosphere were 7.6 ± 1.6 μm/year and 4.9 ± 2.2 μm/year, respectively.
- The CRs of SS 310 in this work decrease from 52.6 μm/year to 7.6 μm/year, while CRs of In 800H decrease from 15.3 μm/year to 4.9 μm/year with increasing exposure time from 100 h to 2000 h.
- With an optimizing salt purification by 2.8 wt% Mg before immersion tests, the concentration of MgOHCl corrosive impurity was smaller than 200 ppm O (~0.096 wt%), which can be seen as the acceptable impurity level of $MgCl_2$-KCl-NaCl for Fe-based alloy.
- The development of oxide layers on the sample surface illustrated the growth of MgO particles from several micro-meter to be about one hundred micro-meters during the 2000-hour test. The MgO layers showed no apparent correlation with the corrosion depth in this work.
- An industrial procedure similar as that for the commercial molten nitrate-TES system could be designed for the commercial molten chloride-TES system to ensure the long service life time. It includes the salt pre-melting and salt purification by an equipment using Mg, pumping of the purified salt into the commercial salt tank and corrosion control during the operation of the chloride-TES system.

In summary, this work experimentally proves that Fe-based alloys can reach the target of 15 μm/year proposed by DOE in $MgCl_2$-KCl-NaCl mixtures at 700 °C with Mg salt-purifier and corrosion-inhibitor. Moreover, if the stainless steels fulfill other essential requirements like mechanical properties, they can be used as the main structural material of the salt tank. This makes the chloride-TES system have a similar cost (27 USD/kWh-th) to the commercial nitrate-TES system and be more cost-effective and competitive.

In the future, the following work is suggested to develop the chloride-TES technology for final commercial applications:

- With Mg-additive, some stainless steels or Fe-based alloys with good high-temperature mechanical properties could be tested in molten chloride salt.
- Some essential structural elements (e.g., welding joint) could be tested in the purified molten chloride salt.

CRediT authorship contribution statement

Qing Gong: Conceptualization, Methodology, Investigation, Writing – original draft, Visualization. **Hao Shi:** Methodology, Investigation, Writing – review & editing. **Yan Chai:** Methodology, Investigation, Writing – review & editing. **Rui Yu:** Methodology, Investigation, Writing – review & editing. **Alfons Weisenburger:** Methodology, Writing – review & editing. **Dihua Wang:** Methodology, Writing – review & editing. **Alexander Bonk:** Methodology, Writing – review & editing. **Thomas Bauer:** Writing – review & editing, Funding acquisition. **Wenjin Ding:** Conceptualization, Methodology, Writing – review & editing, Supervision, Project administration, Funding acquisition.

Declaration of Competing Interest

The authors declare the following financial interests/personal relationships which may be considered as potential competing interests: Qing Gong reports financial support was provided by German Academic Exchange Service (DAAD).

Acknowledgement

This research has been performed within the DLR-DAAD fellowship program (Nr. 57540125). The authors would like to thank M. Braun, R. Hoffmann, and A. Hanke for support in the different laboratories.

References

[1] Mehos M, Turchi C, Vidal J, Wagner M, Ma Z, Ho C, et al. Concentrating solar power Gen3 demonstration roadmap. United States: National Renewable Energy Lab.(NREL), Golden, CO (United States); 2017. https://doi.org/10.2172/1338899.
[2] Ding W, Bauer T. Progress in Research and Development of Molten Chloride Salt Technology for Next Generation Concentrated Solar Power Plants. Engineering 2021. https://doi.org/10.1016/j.eng.2020.06.027.
[3] Bauer T, Odenthal C, Bonk A. Molten Salt Storage for Power Generation. Chemie Ingenieur Technik 2021;93:534-46. https://doi.org/10.1002/cite.202000137.
[4] Villada C, Bonk A, Bauer T, Bolívar F. High-temperature stability of nitrate/nitrite molten salt mixtures under different atmospheres. Appl Energy 2018;226:107–15. https://doi.org/10.1016/j.apenergy.2018.05.101.
[5] Wei X, Song M, Wang W, Ding J, Yang J. Design and thermal properties of a novel ternary chloride eutectics for high-temperature solar energy storage. Appl Energy 2015;156:306–10. https://doi.org/10.1016/j.apenergy.2015.07.022.
[6] Vignarooban K, Pugazhendhi P, Tucker C, Gervasio D, Kannan AM. Corrosion resistance of Hastelloys in molten metal-chloride heat-transfer fluids for concentrating solar power applications. Sol Energy 2014;103:62–9. https://doi.org/10.1016/j.solener.2014.02.002.
[7] Villada C, Ding W, Bonk A, Bauer T. Engineering molten MgCl2–KCl–NaCl salt for high-temperature thermal energy storage: Review on salt properties and corrosion control strategies. Sol Energy Mater Sol Cells 2021;232. https://doi.org/10.1016/j.solmat.2021.111344.
[8] Vignarooban K, Xu X, Arvay A, Hsu K, Kannan AM. Heat transfer fluids for concentrating solar power systems – A review. Appl Energy 2015;146:383–96. https://doi.org/10.1016/j.apenergy.2015.01.125.
[9] Ambrosek JW. Molten chloride salts for heat transfer in nuclear systems: The University of Wisconsin - Madison; 2011. https://www.proquest.com/docview/885007950?parentSessionId=5Ny2J3Dfp0LfvlEPUHP6b3HyR2nnutVr4yPpB7p7OEY%3D.
[10] Ezell NDB, Raiman SS, Kurley JM, McDuffee J. Neutron irradiation of alloy N and 316L stainless steel in contact with a molten chloride salt. Nucl Eng Technol 2021;53:920–6. https://doi.org/10.1016/j.net.2020.07.042.
[11] Guo S, Zhang J, Wu W, Zhou W. Corrosion in the molten fluoride and chloride salts and materials development for nuclear applications. Prog Mater Sci 2018;97:448–87. https://doi.org/10.1016/j.pmatsci.2018.05.003.
[12] Raiman SS, Mayes RT, Kurley JM, Parrish R, Vogli E. Amorphous and partially-amorphous metal coatings for corrosion resistance in molten chloride salt. Sol Energy Mater Sol Cells 2019;201. https://doi.org/10.1016/j.solmat.2019.110028.
[13] Raiman SS, Lee S. Aggregation and data analysis of corrosion studies in molten chloride and fluoride salts. J Nucl Mater 2018;511:523–35. https://doi.org/10.1016/j.jnucmat.2018.07.036.
[14] Mohan G, Venkataraman M, Gomez-Vidal J, Coventry J. Assessment of a novel ternary eutectic chloride salt for next generation high-temperature sensible heat storage. Energy Convers Manage 2018;167:156–64. https://doi.org/10.1016/j.enconman.2018.04.100.
[15] Zhao Y. Molten Chloride Thermophysical Properties, Chemical Optimization, and Purification. National Renewable Energy Lab.(NREL), Golden, CO (United States); 2020. https://www.osti.gov/biblio/1734652.
[16] Turchi CS, Vidal J, Bauer M. Molten salt power towers operating at 600–650 C: Salt selection and cost benefits. Sol Energy 2018;164:38–46. https://doi.org/10.1016/j.solener.2018.01.063.
[17] Villada C, Ding W, Bonk A, Bauer T. Simulation-Assisted Determination of the Minimum Melting Temperature Composition of MgCl2–KCl–NaCl Salt Mixture for Next-Generation Molten Salt Thermal Energy Storage. Front Energy Res 2022;10. https://doi.org/10.3389/fenrg.2022.809663.
[18] Ding W, Bonk A, Bauer T. Corrosion behavior of metallic alloys in molten chloride salts for thermal energy storage in concentrated solar power plants: A review. Front Chem Sci Eng 2018;12:564–76. https://doi.org/10.1007/s11705-018-1720-0.
[19] Turchi C, Gage S, Martinek J, Jape S, Armijo K, Coventry J, et al. CSP Gen3: Liquid-Phase Pathway to SunShot. National Renewable Energy Lab.(NREL), Golden, CO (United States); 2021. https://doi.org/10.2172/1807668.
[20] Sun H, Wang J, Li Z, Zhang P, Su X. Corrosion behavior of 316SS and Ni-based alloys in a ternary NaCl-KCl-MgCl2 molten salt. Sol Energy 2018;171:320–9. https://doi.org/10.1016/j.solener.2018.06.094.
[21] Ding W, Bonk A, Gussone J, Bauer T. Electrochemical measurement of corrosive impurities in molten chlorides for thermal energy storage. J Energy Storage 2018;15:408–14. https://doi.org/10.1016/j.est.2017.12.007.
[22] D'Souza B, Zhuo W, Yang Q, Leong A, Zhang J. Impurity driven corrosion behavior of HAYNES® 230® alloy in molten chloride Salt. Corros Sci 2021;187. https://doi.org/10.1016/j.corsci.2021.109483.
[23] Grégoire B, Oskay C, Meißner T, Galetz M. Corrosion mechanisms of ferritic-martensitic P91 steel and Inconel 600 nickel-based alloy in molten chlorides. Part II: NaCl-KCl-MgCl2 ternary system. Sol Energy Mater Sol Cells 2020;216. https://doi.org/10.1016/j.solmat.2020.110675.
[24] Sun H, Wang J-Q, Tang Z, Liu Y, Wang C. Assessment of effects of Mg treatment on corrosivity of molten NaCl-KCl-MgCl2 salt with Raman and Infrared spectra. Corros Sci 2020;164. https://doi.org/10.1016/j.corsci.2019.108350.
[25] Kipouros GJ, Sadoway DR. A thermochemical analysis of the production of anhydrous MgCl2. J Light Met 2001;1:111–7. https://doi.org/10.1016/S1471-5317(01)00004-9.
[26] Kashani-Nejad S, Ng K, Harris R. Properties of MgOHCl. Metall Mater Trans B 2004;35:406–8. https://doi.org/10.1007/s11663-004-0043-3.
[27] Kashani-Nejad S. Oxides in the dehydration of magnesium chloride hexahydrate: McGill University; 2005. https://escholarship.mcgill.ca/concern/theses/ws859g01q.
[28] Garcia-Diaz B, Martinez-Rodriguez M. Full loop thermodynamic corrosion inhibition and sensing in molten chloride systems. Final report. Office of Scientific and Technical Information (OSTI); 2020.10.2172/1734665.
[29] Garcia-Diaz BL, Olson L, Martinez-Rodriguez M, Fuentes R, Colon-Mercado H, Gray J. High temperature electrochemical engineering and clean energy systems. J. South Carolina Acad Sci 2016;14:4. https://scholarcommons.sc.edu/jscas/vol14/iss1/4.
[30] Ding W, Shi H, Xiu Y, Bonk A, Weisenburger A, Jianu A, et al. Hot corrosion behavior of commercial alloys in thermal energy storage material of molten MgCl2/KCl/NaCl under inert atmosphere. Sol Energy Mater Sol Cells 2018;184:22–30. https://doi.org/10.1016/j.solmat.2018.04.025.
[31] Zhang M, Ge J, Yin T, Zhang J. Redox potential measurements of Cr (II)/Cr Ni (II)/Ni and Mg (II)/Mg in molten MgCl2–KCl–NaCl mixture. J Electrochem Soc 2020;167. https://doi.org/10.1149/1945-7111/aba15a.
[32] Ren S, Chen Y, Ye X-X, Jiang L, Yan S, Liang J, et al. Corrosion behavior of carburized 316 stainless steel in molten chloride salts. Sol Energy 2021;223:1–10. https://doi.org/10.1016/j.solener.2021.05.057.
[33] Mortazavi A, Zhao Y, Esmaily M, Allanore A, Vidal J, Birbilis N. High-temperature corrosion of a nickel-based alloy in a molten chloride environment – The effect of thermal and chemical purifications. Sol Energy Mater Sol Cells 2022;236. https://doi.org/10.1016/j.solmat.2021.111542.
[34] Lambrecht M, de Miguel MT, Lasanta MI, Pérez FJ. Past research and future strategies for molten chlorides application in concentrated solar power technology. Sol Energy Mater Sol Cells 2022;237. https://doi.org/10.1016/j.solmat.2021.111557.
[35] Ding W, Gomez-Vidal J, Bonk A, Bauer T. Molten chloride salts for next generation CSP plants: Electrolytical salt purification for reducing corrosive impurity level. Sol Energy Mater Sol Cells 2019;199:8-15. https://doi.org/10.1016/j.solmat.2019.04.021.
[36] Ding W, Yang F, Bonk A, Bauer T. Molten chloride salts for high-temperature thermal energy storage: Continuous electrolytic salt purification with two Mg-electrodes and alternating voltage for corrosion control. Sol Energy Mater Sol Cells 2021;223:110979. https://doi.org/10.1016/j.solmat.2021.110979.
[37] Zhao Y, Klammer N, Vidal J. Purification strategy and effect of impurities on corrosivity of dehydrated carnallite for thermal solar applications. RSC Adv 2019;9:41664-71. https://doi.org/10.1039/C9RA09352D.
[38] Zhao Y, Vidal J. Potential scalability of a cost-effective purification method for MgCl2-Containing salts for next-generation concentrating solar power technologies. Sol Energy Mater Sol Cells 2020;215. https://doi.org/10.1016/j.solmat.2020.110663.
[39] Ding W, Shi H, Jianu A, Xiu Y, Bonk A, Weisenburger A, et al. Molten chloride salts for next generation concentrated solar power plants: Mitigation strategies against corrosion of structural materials. Sol Energy Mater Sol Cells 2019;193:298–313. https://doi.org/10.1016/j.solmat.2018.12.020.
[40] Kurley JM, Halstenberg PW, McAlister A, Raiman S, Dai S, Mayes RT. Enabling chloride salts for thermal energy storage: implications of salt purity. RSC Adv 2019;9:25602–8. https://doi.org/10.1039/C9RA03133B.
[41] Mayes RT, Kurley Iii JM, Halstenberg PW, McAlister A, Sulejmanovic D, Raiman SS, et al. Purification of Chloride Salts for Concentrated Solar Applications. Office of Scientific and Technical Information (OSTI); 2018.10.2172/1506795.
[42] Maricle DL, Hume DN. A new method for preparing hydroxide-free alkali chloride melts. United States: Massachusetts Inst. of Tech., Cambridge. Lab. for Nuclear Science; 1959. https://www.osti.gov/biblio/4197980.
[43] Pint BA, McMurray JW, Willoughby AW, Kurley JM, Pearson SR, Lance MJ, et al. Re-establishing the paradigm for evaluating halide salt compatibility to study commercial chloride salts at 600°C–800°C. Mater Corros 2019;70:1439–49. https://doi.org/10.1002/maco.201810638.
[44] Li Y, Wang X. Strengthening mechanisms and creep rupture behavior of advanced austenitic heat resistant steel SA-213 S31035 for A-USC power plants. Materials Science and Engineering: A. 2020;775:138991. https://doi.org/10.1016/j.msea.2020.138991.
[45] Chai G, Forsberg U. Sanicro 25: an advanced high-strength, heat-resistant austenitic stainless steel. Materials for ultra-supercritical and advanced ultra-supercritical power plants: Elsevier; 2017. p. 391-421. https://doi.org/10.1016/B978-0-08-100552-1.00012-9.
[46] Taylor M, Ramirez J, Charit I, Potirniche GP, Stephens R, Glazoff MV. Creep behavior of Alloy 709 at 700° C. Materials Science and Engineering: A. 2019;762:138083. https://doi.org/10.1016/j.msea.2019.138083.
[47] Gilardi T, Rodriguez G, Gomez A, Leybros J, Borgard J, Carles P, et al. Influence of material choice on cost estimation of some key components of the sulfur iodine thermochemical process. Proc of 16th World Hydrogen Energy Conference (WHEC) 2006. p. 13-6. https://core.ac.uk/download/pdf/37987793.pdf.
[48] ASTM-G1-03. Standard Practice for Preparing, Cleaning, and Evaluating Corrosion Test Specimens. 1999.

[49] Guo L, Liu Q, Yin H, Pan TJ, Tang Z. Excellent corrosion resistance of 316 stainless steel in purified NaCl-MgCl2 eutectic salt at high temperature. Corros Sci 2020; 166:108473. https://doi.org/10.1016/j.corsci.2020.108473.
[50] Grégoire B, Oskay C, Meißner T, Galetz M. Corrosion mechanisms of ferritic-martensitic P91 steel and Inconel 600 nickel-based alloy in molten chlorides* Part I* NaCl–KCl binary system. Sol Energy Mater Sola Cells 2020;215. https://doi.org/10.1016/j.solmat.2020.110659.
[51] Skar RA. Chemical and electrochemical characterisation of oxide/hydroxide impurities in the electrolyte for magnesium production: Norwegian University of Science and Technology Fakultet for naturvitenskap og teknologi; 2001. http://hdl.handle.net/11250/244438.
[52] Sridharan K, Allen T. Corrosion in molten salts. Molten salts chemistry: Elsevier; 2013. p. 241-67. https://doi.org/10.1016/B978-0-12-398538-5.00012-3.
[53] Hanson K, Sankar KM, Weck PF, Startt JK, Dingreville R, Deo CS, et al. Effect of Excess Mg to Control Corrosion in Molten MgCl2 and KCl Eutectic Salt Mixture. Corros. Sci. 2021:109914. https://doi.org/10.1016/j.corsci.2021.109914.
[54] Zhu F. Microstructural evolution in austenitic stainless steels for extended-life power station applications: Loughborough University; 2011. https://repository.lboro.ac.uk/articles/thesis/Microstructural_evolution_in_austenitic_stainless_steels_for_extended-life_power_station_applications/9230147.
[55] Yamamoto Y, Brady MP, Lu ZP, Maziasz PJ, Liu CT, Pint BA, et al. Creep-resistant, Al2O3-forming austenitic stainless steels. Science 2007;316:433-6. https://www.science.org/doi/10.1126/science.1137711.
[56] Terada M, Escriba DM, Costa I, Materna-Morris E, Padilha AF. Investigation on the intergranular corrosion resistance of the AISI 316L(N) stainless steel after long time creep testing at 600 °C. Mater Charact. 2008;59(663–8):7. https://doi.org/10.1016/j.matchar.2007.05.01.
[57] Zeng X, Wang X, Li H, Qian C. Strength and creep-fatigue analysis of a molten-salt storage tank. In: 2019 International Conference on Artificial Intelligence and Advanced Manufacturing (AIAM): IEEE; 2019. p. 742-6. https://doi.org/10.1109/AIAM48774.2019.00153.
[58] Mehos M, Price H, Cable R, Kearney D, Kelly B, Kolb G, et al. Concentrating Solar Power Best Practices Study. Office of Scientific and Technical Information (OSTI); 2020.10.2172/1665767.
[59] Ding W, Gong Q, Bauer T. Kontinuierliches Reinigungssystem für Halogensalze mit Mg-Additiv. In: DPMA, editor. Germany2021.
[60] Guo J, Hoyt N, Williamson M. Multielectrode array sensors to enable long-duration corrosion monitoring and control of concentrating solar power systems. J. Electroanal. Chem. 2021;884:115064. https://doi.org/10.1016/j.jelechem.2021.115064.
[61] Choi S, Orabona NE, Dale OR, Okabe P, Inman C, Simpson MF. Effect of Mg dissolution on cyclic voltammetry and open circuit potentiometry of molten MgCl2–KCl–NaCl candidate heat transfer fluid for concentrating solar power. Sol Energy Mater Sol Cells 2019;202. https://doi.org/10.1016/j.solmat.2019.110087.
[62] Susskind H, Hill F, Green L, Kalish S, Kukacka L, McNulty W, et al. Corrosion studies for a fused salt-liquid metal extraction process for the liquid metal fuel reactor. Brookhaven National Lab., Upton, NY; 1960. https://doi.org/10.2172/4023508.
[63] ASME. ASME Boiler And Pressure Vessel Code 2010. ASME BPVC (2010). New York: ASME 2010.

Paper III: Selection of cold tank structural material utilizing corrosion control at 500 °C

Gong Q, Hanke A, Kessel F, Bonk A, Bauer T, Ding W. Molten chloride salt technology for next-generation CSP plants: Selection of cold tank structural material utilizing corrosion control at 500 °C. Solar Energy Materials and Solar Cells. 2023;253. https://doi.org/10.1016/j.solmat.2023.112233

Solar Energy Materials & Solar Cells 253 (2023) 112233

Contents lists available at ScienceDirect

Solar Energy Materials and Solar Cells

journal homepage: www.elsevier.com/locate/solmat

Molten chloride salt technology for next-generation CSP plants: Selection of cold tank structural material utilizing corrosion control at 500 °C

Qing Gong [a,*], Andrea Hanke [a], Fiona Kessel [b], Alexander Bonk [a], Thomas Bauer [c], Wenjin Ding [a]

[a] Institute of Engineering Thermodynamics, German Aerospace Center (DLR), Stuttgart, Germany
[b] Institute of Structures and Design, German Aerospace Center (DLR), Stuttgart, Germany
[c] Institute of Engineering Thermodynamics, German Aerospace Center (DLR), Cologne, Germany

ARTICLE INFO

Keywords:
Concentrating solar power (CSP)
Thermal energy storage (TES)
Molten chloride salt
Corrosion mitigation
Material selection of cold tank

ABSTRACT

$MgCl_2$-KCl-NaCl molten chloride salt is a promising candidate for thermal energy storage medium and heat transfer fluid for next-generation Concentrating Solar Power (CSP) plants (Gen-3 CSP). The main challenge has yet been the selection of economical yet corrosion-resistant structural materials to be used. Previous work by the authors has demonstrated that simple corrosion control strategies can mitigate corrosion effects, thereby allowing the use of classical stainless steels as structural materials in the hot part (e.g., ≥700 °C) of the CSP system. This study addresses the selection of cold tank materials, which have to withstand corrosion effects up to temperatures of 500 °C. Two cost-effective commercial types of steels, P91 and SS 304, were examined as candidates for structural materials, and controlled corrosion experiments were performed in molten $MgCl_2$-KCl-NaCl salt at 500 °C for 1400 h. Before the exposure tests, the chloride salt was purified using a simple yet effective Mg-doping technique. The results show that the corrosion rates (CRs) of P91 samples are consistently low (<15 μm/year) for both macroscopic and microscopic analysis. The cheaper P91 steel outperforms the more expensive SS 304 in terms of corrosion resistance and also may prove to be beneficial in terms of mechanical properties and economics. Overall, the use of P91 as a cold tank structural material allows for significant cost reduction of the cold tank for chloride-TES system and enhances its competitiveness compared with commercial nitrate-TES.

1. Introduction

The ternary mixture of $MgCl_2$-KCl-NaCl is a viable thermal energy storage (TES) medium for next-generation concentrating solar power (CSP) plants [1–3]. With the chloride-based thermal energy storage (chloride-TES), the operating temperature range of CSP could be extended to between 420 °C and 800 °C [2,4], which is significantly higher than the commercial CSP with nitrate thermal energy storage (nitrate-TES), whose operating temperature range is 290 °C–565 °C [5,6]. Higher operating temperatures allow for the integration of high-efficiency power cycles (e.g., CO_2 Brayton cycles), which can result in higher overall efficiency and overall reduction of the Levelized Cost of Electricity (LCOE) [1–3].

As depicted in Fig. 1, the molten salt TES system is one of the most critical components in the CSP plant, predominantly consisting of the hot tank, the cold tank, molten salt as interior, piping, and additional components (e.g., foundation, insulation). The cold tank is an indispensable part of the TES system, which, in the commercial nitrate-TES, is commonly constructed from carbon steel (e.g., ASTM A 516 70). It accounts for approximately 8% of the total system cost, e.g., 4.4 million USD for a 2703 MWh-th capacity, as shown in the report published by the National Renewable Energy Laboratory (NREL) in the USA [1].

Recent investigations on selecting suitable hot-tank materials at ≥700 °C have revealed numerous compatibility issues, especially related to corrosion phenomena originating from the molten chloride salt [2,7–16]. In contrast, cold tanks for chloride-TES have received relatively little attention. According to the literature [1–4], $MgCl_2$-KCl-NaCl based TES system has the cold tank with an operating temperature range of 420–500 °C. To our knowledge, there is no specific study on cold tank structural material for chloride-TES in this temperature range available in the literature.

The selection of adequate cold-tank structural material is subject to noticeable challenges. Firstly, the structural material of TES in the cold

* Corresponding author.
E-mail address: qing.gong@dlr.de (Q. Gong).

https://doi.org/10.1016/j.solmat.2023.112233
Received 9 January 2023; Received in revised form 3 February 2023; Accepted 7 February 2023
Available online 16 February 2023

tank is cost-sensitive since a large amount of steel is used to make the vessel for upwards of 30 000 tons of molten salt. According to the report published by NREL [1], the cost of the cold tank is about four times higher than nitrate-TES when SS 347H is used as the cold tank material in a chloride-TES system. The total cold tank costs are estimated to be 16.8 million USD for chloride-TES, but only 4.4 million USD for nitrate-TES, considering an equal capacity of 2703 MWh-th. Although the SS 347H at 500 °C shows comparable maximum allowable stress to the carbon steel (ASTM A 516 70) at 300 °C [17], the compatibility of stainless steel with molten chloride salt was not mentioned in this report. This report has not discussed some key issues, such as corrosion, sufficiently [1].

The corrosion of structural material at 500 °C is still not negligible, although the molten chloride salt at 500 °C is not as corrosive as at ≥ 700 °C. In the previous work in the 1960s on the molten salt reactor (MSR), the Brookhaven National Laboratory (BNL) in the USA published corrosion data of Fe-Cr-Ni alloys (e.g., SS 347, 5 Cr steel) in the $MgCl_2$-KCl-NaCl melts at the temperature range of 450 °C and 500 °C [18]. Before the exposure tests, the researchers used Bi metal to handle the corrodents and reduce the redox of the molten salt. In their experiments, intergranular and pitting corrosions were found on the cross-section of SS 347 at 500 °C in a vacuum, which would cause fatal damage to the structural materials during operation. However, due to the lack of understanding of the corrosion mechanism and effective detection methods for corrosive impurities (e.g., $MgOH^+$) in salt [19], the corrosions were not well evaluated and mitigated. As the Oak Ridge National Laboratory (ORNL) mentioned in a report published in 2022 [20], there is still a gap in the research on the long-term corrosion of structural materials in chloride salts at 500 °C.

In general, the anti-corrosion of molten chloride salts at high temperatures involves two aspects: the optimization of structural materials and the purification of the salts. The optimization of structural materials encompasses a range of methods, including coating [21,22] and pre-oxidation [23,24] on metallic materials, as well as using non-metallic materials with good corrosion resistance such as oxide ceramics [25], composite material [26], and insulating firebrick [3,27]. However, the coating and pre-oxidation methods may face thermal shock issues. Non-metallic structural materials such as oxide ceramics often have weaker fracture toughness and/or complex shape limitation, compared to metallic materials. Another aspect of anti-corrosion involves reducing the concentration of corrosive impurities, such as MgOHCl, in the molten chloride salt through effective purification techniques [9,13,28–32], in order to use affordable metallic materials as the main structural materials in chloride-TES system. For more information on corrosion behavior and control of structural materials in molten chlorides, the review papers of our group [2,4,10] are suggested. In our previous work, the CR of SS 310 was suppressed to <15 μm/year in the Mg-purified $MgCl_2$-KCl-NaCl molten salt at 700 °C, principally allowing the use of stainless steel not Ni-based alloy, as hot tank material [9]. This shows the feasibility and high-efficiency of Mg for the molten chloride salt purification. But the corrosion of commercial steel at 500 °C in purified salt has not been sufficient investigated.

In this work, we selected the P91 (EN 1.4903, ASME SA-213) and SS 304 (EN 1.4301, ASME SA-240) as the candidates for the cold tank structural materials. Both candidates offer outstanding mechanical properties at 500 °C. However, the poor corrosion resistance in the molten chloride salt limits the application of P91 and SS 304. To overcome the corrosion challenges, in line with our previous work [9], the $MgCl_2$-KCl-NaCl molten chloride salts were purified with liquid Mg at 700 °C. Afterward, the P91 and SS 304 samples were exposed to the $MgCl_2$-KCl-NaCl melts at 500 °C for up to 1400 h. The extracted salt samples of this series of experiments were analysed by titration and atomic absorption spectroscopy (AAS). In addition, the CR of the alloy samples was determined by descaling (mass change), and cross-sections were measured by scanning electron microscope (SEM) with Energy-dispersive X-ray spectroscopy (EDX). Finally, the cost of the P91 cold tank of chloride-TES was estimated based on the corrosion test and data available in the literature [1,17,33].

2. Material and methods

2.1. Chemicals and alloys

The ternary eutectic $MgCl_2$-NaCl-KCl (47.1-30.2–22.7 mol.%, 56.5-22.2-21.3 wt%) mixture was synthesized by stoichiometric mixing of magnesium chloride ($MgCl_2$, Magnesia, purity >99 wt%), potassium chloride (KCl, Alfa Aesar, purity >99 wt%), and sodium chloride (NaCl, Alfa Aesar, purity >99 wt%) [4]. Batches of ~50 g were produced for individual series of experiments. The salts were weighed, mixed, and ground in a glovebox (GSTM, O_2 < 0.5 ppm, H_2O < 1 ppm). Magnesium metal cylinders (Thermo Scientific, purity >99.9 wt%) with 3 mm diameter and ~5 mm length were cut, polished, and weighed to be later used as purification agents. Two steel types (P91 and SS 304) were employed for the exposure test in the molten chloride salt. The chemical compositions of the tested alloy are listed in Table 1 [17]. Before the exposure test, the alloy samples were processed into four groups of 20 × 10 × 2 cuboids and polished with successively finer SiC sandpapers down to 1200 grids.

2.2. Exposure test

Fig. 2 (a) shows the schematic diagram of the experimental setup for the exposure test. The exposure test was performed in an autoclave with a custom-designed flange. The flange was equipped with several valves

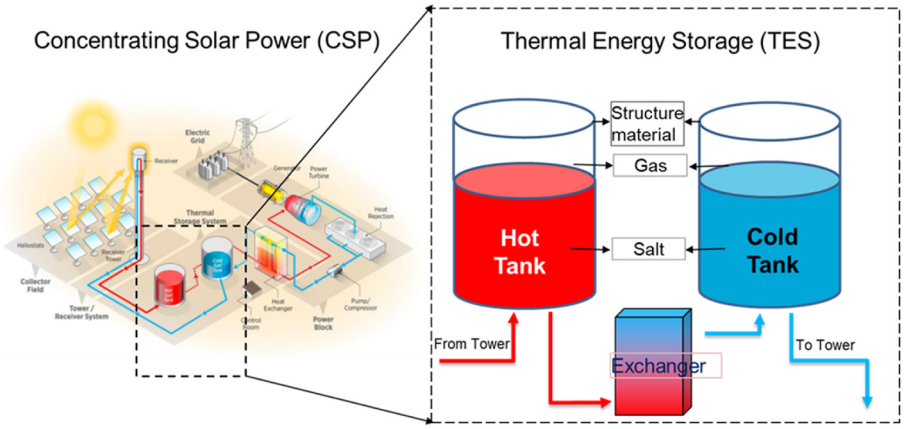

Fig. 1. A molten salt thermal energy storage (TES) system of the concentrating solar power (CSP) plant. Figure adapted from Ref. [1].

Table 1
Composition of tested alloys (in wt.%) according to the ASME boiler and pressure vessel code [17].

Samples	Type	Fe	Cr	Ni	C	Mn	S	P	Si	N	Mo	V	Nb	Al
P91 (1.4903)	Ferritic-martensitic	Bal.	8.0–9.5	0.4	0.08–0.12	0.3–0.56	0.01	0.020	0.2–0.5	0.03–0.07	0.85–1.05	0.18–0.25	0.06–0.10	0.02
SS 304 (1.4301)	Austenitic	Bal.	17.5–19.5	8.0–10.5	0.07	2.0	0.03	0.045	0.75	0.1	–	–	–	–

to sample the alloy and salt during the exposure test. According to a 100-mbar overpressure test, the leakage was <3 mbar/h. The alloy samples were loaded in 3D-printed alumina holders (Steinbach AG Germany), which have shown excellent compatibility with molten chloride salts in our previous work [25]. In this work, four groups of P91 and SS 304 samples were loaded in four designed alumina holders, as shown in Fig. 2 (a). Each alumina holder has two sample slots for the placement of two samples separately, avoiding galvanic coupling of alloy samples during the exposure tests.

At the beginning of the exposure test, the 50 g $MgCl_2$-KCl-NaCl salt mixtures were loaded in four separate alumina crucibles with 1.4 g Mg metal in the glove box. Then the loaded alumina crucibles were transported into the autoclave. During Phase I, the flange covered the autoclave was evacuated to – 900 mbar four times with the pump shown in Fig. 2 (b). After the evacuation, the autoclave was protected by high-purity argon (purity >99.999%) with a flow rate of 20 L/h. In Phase II, the salts with the Mg purifier were heated to – and isothermally held at 700 °C 16 h for salt pre-purification, consistent with our previous work [9]. Around 2 g of salt samples were extracted from the autoclave for post-analysis before the alloy samples were immersed. When the temperature cooled to 500 °C, four alumina crucibles with alloy samples were immersed in the purified chloride melts. After 250, 500, and 1400 h of immersion, the alloy pieces were sampled from the molten salt and washed with distilled water. Immediately after the alloy sampling, 3–4 g salt samples were also extracted to qualify and quantify corrosive impurities and corrosion products. The alloy and salt sampling resulted in the transient drop from overpressure to atmospheric pressure, as can be observed in Fig. 2 (b), indicating that the atmosphere in the autoclave exchanged with air shortly during the sampling.

2.3. Alloy corrosion analysis

The corrosion of alloy samples was analysed by both mass loss and microstructural methods, as summarized in Table 2. All alloy samples were weighed before and after the exposure test by a microbalance (Mettler Toledo, readability 1 μg) to obtain the mass loss per unit area without descaling, as shown in Eq. (1). Before the weight, the samples were cleaned with the deionized water to remove the residual salt after exposure test. In addition, the groups of 250 h and 1400h-1 samples were descaled with acid according to the standard ASTM-G1 [34] to extract the CR in μm/year based on Eq. (2).

$$\Delta m\ \left(mg\,/\,cm^2\right) = \frac{m_0 - m_1}{A} \tag{1}$$

$$CR\ (\mu m\,/\,year) = \frac{K \times \Delta m}{t \times \rho} \tag{2}$$

where,

K is a constant 8.76×10^7 (μm h cm^{-1}·$year^{-1}$);

m_0 and m_1 are the mass of samples before and after immersion test in g;

A is the surface area of sample in cm^2,

t is immersion time in hour;

ρ is the density of samples in g/cm^3. The density of SS 304 and P91 are 7.93 g/cm^3 and 7.77 g/cm^3, respectively.

After the exposure experiments, the alloy samples were embedded in an epoxy resin and ground with 320, 600, and 1200-grit SiC sand papers successively. Subsequently, the ground samples were polished with 9 μm, 3 μm, and 1 μm diamond suspension. The cross-sections and surfaces morphology of the samples were investigated with a scanning electron microscope (SEM, Zeiss Ultra Plus, Carl Zeiss Microscopy GmbH, Jena, Germany) and energy-dispersive X-ray spectroscopy (EDX, X-Max20, Oxford Instruments, Germany). The sample IDs and the performed analysis methods are listed in Table 2. Two groups of 1400 h samples were marked as 1400h-1 and 1400h-2. The 1400h-1 samples were characterized by acid descaling and mass loss. The 1400h-2

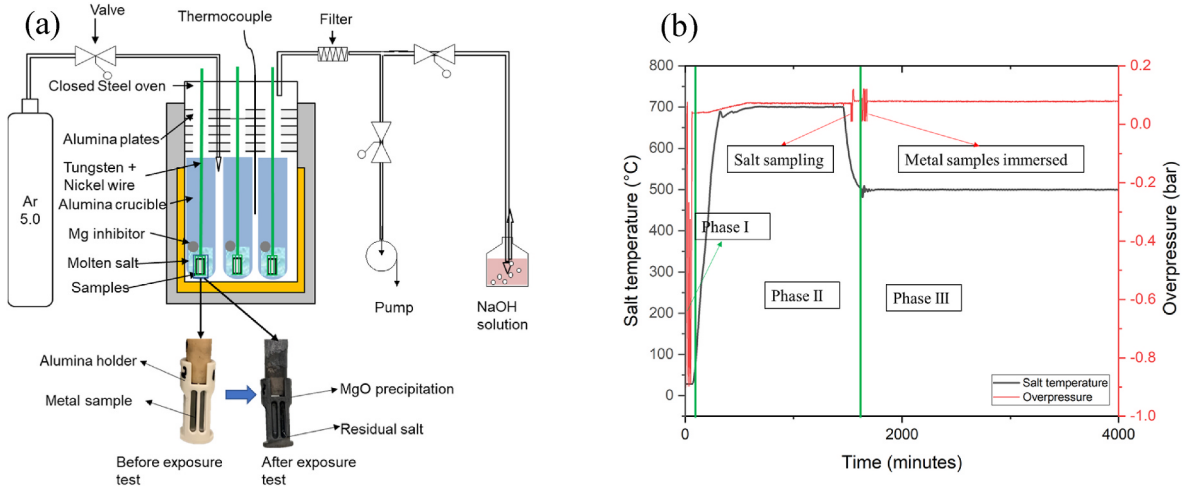

Fig. 2. (a) Schematic diagram of experimental set-up for immersion test with the alumina crucible before and after test. (b) The measured temperature and pressure in the first 4000 min of immersion test.

Table 2
Immersion corrosion test sample IDs and corresponding corrosion analysis methods.

Sample ID	Duration of immersion hour	Sample size mm^3	Mass loss without descaling	Mass loss with descaling	SEM-EDX
P91-250h	250	20 × 10 × 2	Yes	Yes	Yes
P91-500h	500	20 × 10 × 2	Yes	No	Yes
P91-1400h-1	1400	20 × 10 × 2	Yes	Yes	No
P91-1400h-2	1400	20 × 10 × 2	Yes	No	Yes
SS304-250h	250	20 × 10 × 2	Yes	Yes	Yes
SS304-500h	500	20 × 10 × 2	Yes	No	Yes
SS304-1400h-1	1400	20 × 10 × 2	Yes	Yes	No
SS304-1400h-2	1400	20 × 10 × 2	Yes	No	Yes

samples were characterized with SEM-EDX. In order to analyse the surface oxide layer on the 1400h-2 samples, no descaling was carried out on this group of samples.

2.4. Salt analysis with the titration and AAS

The salt analysis methods were consistent with our previous work [9,35]. Before and after the exposure tests of each sample, 3–4 g molten salts were sampled by a quartz glass tube for further titration and AAS analysis. The acid-base titration was carried out on the high-precision instrument 905 Titrando (Metrohm GmbH, Germany) with a pH electrode to determine the main corrosive impurity MgOHCl in the experimental salt. About 500 mg salt sample with unknown MgOHCl concentration was dissolved in 160 ml deionized water, accelerated by a rotated stirrer during the titration experiments. An N_2 sweep gas was used to prevent the influence of CO_2/H_2CO_3 on the acid-base titration. A 0.01 M HCl standard solution was employed as a titrant and filled into the salt solution with an average 0.2 ml/min rate. The titer determination was performed against sodium carbonate before the titration, as described in our previous work [35]. The rotated stirrer was running continuously to speed up the mass transfer. The pH value decreased from ~9 to 4 with the continuous filling of HCl. During the drop in pH value, the equivalence point was recorded by the titration program, where the extreme value of the pH value slope indicates that HCl was sufficient to neutralize MgOHCl in the solution. Thus, the concentration of MgOHCl can be calculated based on the consumption of HCl at the equivalence point in a unit of parts per million oxygen (ppm O), as shown in Eq. (3). One hundred ppm O means 0.048 wt% MgOHCl in the experimental salt.

$$C(MgOHCl)[ppm\ O] = C_{HCl} \times V_{HCl} \,/\, m_{sample} \times M_O \times ti \times 1000 \quad (3)$$

where,

V_{HCl} is the volume of HCl at equivalence point in L;
C_{HCl} is 0.01 in mol/L;
m_{sample} is the mass of the salt sample in g;
ti is the titer, a dimensionless value;
M_O is the molar mass of oxygen, i.e., 16 g/mol.

According to our previous analysis, the average error of such a titration method was 6.62 ppm O at 36 ppm O MgOHCl concentration with a 4.35 ppm O standard deviation [35]. In this work, each batch of samples was titrated three times to obtain average values and standard deviation.

The procedure of AAS experiments was in line with that in our previous work [9,23]. An atomic absorption spectrometer (AAS, Thermo Scientific iCE 3000 series, Thermo Fisher Scientific, US) was employed to obtain the concentration of Cr, Fe, and Ni elements in salt species. The currents of the hollow lamp at the spectrometer were 12 mA for Cr and 10 mA for Fe and Ni. The spectral bandwidth of analytical lines is 0.2–0.5 nm. The specific wavelengths are 357.9 nm, 248.3 nm, and 232.0 nm for Cr, Fe, and Ni, respectively. The spectrometer has the operating software Solaar AA Version 11.03 installed, which was used to assess signals and determine concentrations. The standard solutions for Cr, Fe, and Ni were made by dissolving the chloride or nitrate salt in 100 mL of distilled water, adding 1 ml of 1 wt% HCl solution, and 10 mL of 10 wt% CsCl solution. These solutions had concentrations of 1, 2, and 5 mg/l. About 1000 mg of salt samples were dissolved in 100 ml of distilled water together with 1 ml of 1 wt% HCl and 10 ml of 10 wt% CsCl for the AAS tests on the salt samples. The measurement limits of AAS are 1.52×10^{-3} mol.% for Cr, 1.41×10^{-3} mol. % for Fe, and 1.35×10^{-3} mol.% for Ni, respectively, in line with previous work [9].

3. Results

3.1. Corrosion tests of alloy samples

3.1.1. Mass loss of alloy samples

The mass loss of alloy samples before and after descaling is shown in Fig. 3. As can be seen, the samples without descaling showed a small mass change (<0.5 mg/cm^2). Seven of eight samples without descaling show mass loss, while the P91-1400h-1 shows 0.045 mg/cm^2 mass gain. Excess Mg was observed on the surface of this group of samples, which can be the reason for the abnormal mass change in this group of samples. After descaling based on the standard of ASTM-G1 [34], the mass loss of samples increased slightly. The most significant mass loss was displayed on the samples of P91-250 h after descaling, whose mass loss was 1.023 mg/cm^2. Based on the mass loss after descaling, the CRs of 250 h and 1400h-1 group can be calculated by Eq. (2). The CRs of 250 h samples are 45 μm/year and 29 μm/year for P91 and SS 304, respectively. In contrast, the CRs of 1400h-1 samples are 1.5 μm/year and 6.14 μm/year for P91 and SS 304, respectively.

3.1.2. SEM-EDX analysis of P91

The surface morphology of sample P91-1400h-2 is illustrated in Fig. 4. The sample was exposed to $MgCl_2$-KCl-NaCl salt at 500 °C for 1400 h with 2.8 wt % Mg under Ar atmosphere. As can be seen from EDX analysis, two types of surface are observed, one with the predominance of Mg and O elements and the other with the predominance of Fe elements. This indicates that the MgO layer unequally covers the body of the P91 sample. It is therefore required to assess the origin of Mg-O-compounds during exposure based on the literature data. According to literature, there are two primary MgO sources in molten $MgCl_2$-KCl-NaCl, which are shown in Eq. (4) and Eq. (5) [9,19,23]. According to the two equations, MgO can result from two entirely different reaction paths. Both, however, require the presence of the corrosive magnesium hydroxy chloride species. In addition, the relatively weak signal of Cr is detectable across the entire sample surface, including both Fe-dominated and Mg- and O-dominated regions. This implies that there is a small amount of $MgCr_2O_4$ spinel in the oxide layer, as demonstrated by in Eq. (6) and discussed in some literature [16,19,36].

$$MgOHCl_{(s)} \rightarrow MgO_{(s)} + HCl_{(g)} \quad (4)$$

$$M_{(s/l)} + 2MgOHCl_{(l)} \rightarrow 2\mathbf{MgO}_{(s)} + MCl_{2\ (s/l)} + H_{2(g)}$$

$$M = Mg, Fe, Cr, Ni \quad (5)$$

$$MgO_{(s)} + Cr_2O_{3(s)} \rightarrow MgCr_2O_4(s) \quad (6)$$

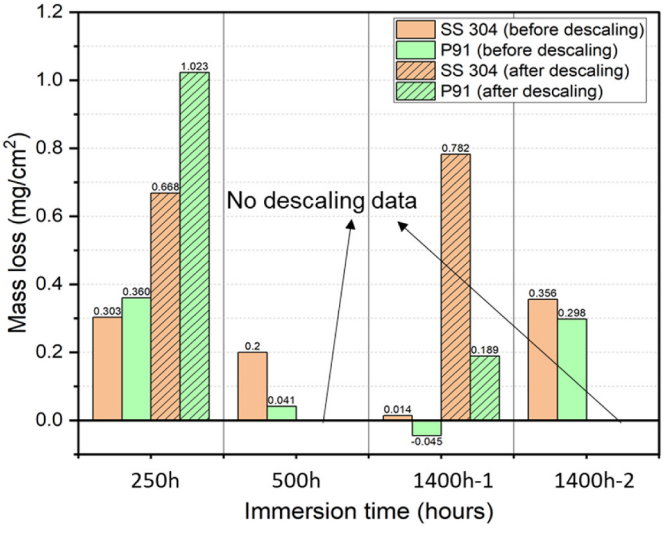

Fig. 3. Mass loss of SS 304 and P91 samples in the purified molten $MgCl_2$-KCl-NaCl at 500 °C. The samples were weighted after exposure test before and after descaling.

Fig. 5 shows the cross-section images of samples P91-500 h and P91-1400h-2. Iron is homogeneously distributed in the bulk of the sample. However, there is some chromium enrichment along, what appears to be, the grain boundaries. After both 500 h and 1400 h, the formation of a thin layer at the exposed surface of the steel can be detected. It is composed of MgO according to the EDX-maps. In contrast to the surface EDX analysis shown in Fig. 4, little chromium is detected in the oxide layer of cross-section, indicating oxidation of the metal components was significantly limited during immersion tests. Intergranular can be observed, reflected by inwards corrosion along the grain boundaries, which is typical corrosion in the molten chloride salt observed in the previous work many times [16,18,19,37]. However, the corrosion depth in this work does not change during 500 h and 1400 h for P91, indicating that there is only further marginal corrosion after 500 h. As can be seen in Fig. 5 (b) and (d), the corrosion layers along the grain boundaries of samples P91-500 h and P91-1400h-2 are consistent with each other (~2 μm). Parts of the cross-section images reveal unevenly thick MgO layers at the surface of sample P91-1400h-2 (Fig. 5 (c)). Besides, the corrosion depth is identical in regions of thinner and thicker MgO layers, indicating that bulky MgO precipitates at the surface do not affect the corrosion behavior. In this work, no significant correlation can be concluded between the thickness of MgO and the degradation of the sample. As shown in Fig. 5 (d), the non-uniform corrosion layers under both thick and thin MgO layers are equal 2 μm after the 1400-h exposure test.

Generally, the corrosion mechanisms observed during the analysis of P91 by SEM-EDX are consistent with the mass loss results. For example, the mass loss results show that the CR of P91-1400h-1 is about 1.5 μm/year, while the SEM-EDX results show that the CR of P91-1400h-2 is about 12.5 μm/year (2 μm/1400 h). Considering the matrix loss in the corrosion layer is only about one-tenth, the results of mass-loss and SEM-EDX analysis are comparable. The micro and macro analysis suggest that the corrosion of P91 stalled after the first stage of the exposure experiment. The corrosion of P91 in this work was well controlled by the Mg purifier and inhibitor in molten chloride salt at 500 °C. The CRs were achieved 1.5 μm/year based on the mass-loss result and 12.5 μm/year based on SEM-EDX results, which is smaller than the 15 μm/year corrosion-rate target [9,38].

3.1.3. SEM-EDX analysis of SS 304

The surface morphology of sample SS 304-1400h-2 is shown in Fig. 6. This sample was exposed to $MgCl_2$-KCl-NaCl at 500 °C with 2.8 wt % Mg for 1400 h. As can be observed from SEM-EDX images, the SS 304 sample was covered by a layer consisting of magnesium and oxygen. Only weak signals for Fe, Cr, and Ni can be observed. This indicates that the MgO layer on the SS 304 sample is continuous and denser than on the P91 sample.

The cross-section images of samples SS304-250 h, SS304-500 h, and SS 304-1400h-2 are shown in Fig. 7. The formation of elongated voids perpendicular to the surface can be observed. Some of those cracks are enriched in oxygen but are fully depleted in iron, chromium, and nickel. Some, in contrast, are enriched in manganese and sulfur. It is likely, that the empty voids formed due to selective corrosion of a former MnS phase contacting the surface. Therefore, it is reasonable to assume that the SS 304 samples suffered from selective corrosion (i.e., the pitting corrosion) along the MnS phase. The width of such corrosion cracks on the sample surface is typically as small as several microns and cannot be observed by the human eye. However, the depth of such cracks in the steel samples can be tens of microns, as seen in Fig. 7 (a)–(c). Further observation shows that corrosion is constantly developing along a specific phase. The EDX analysis in Fig. 7 (d) shows that this phase contains only two elements, Mn and S, most likely the MnS inclusions shown in the literature [39–41]. In aqueous-based corrosion of stainless steel, MnS inclusions

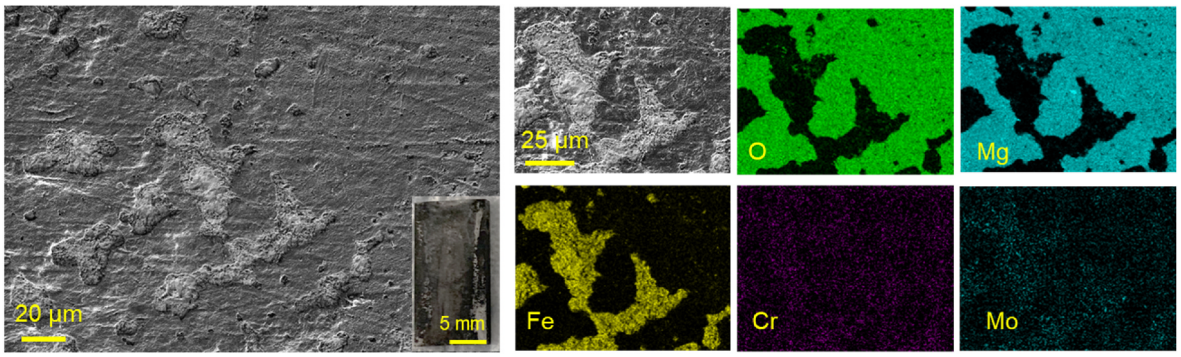

Fig. 4. Surface morphology of sample P91-1400h-2 analysed by SEM and EDX.

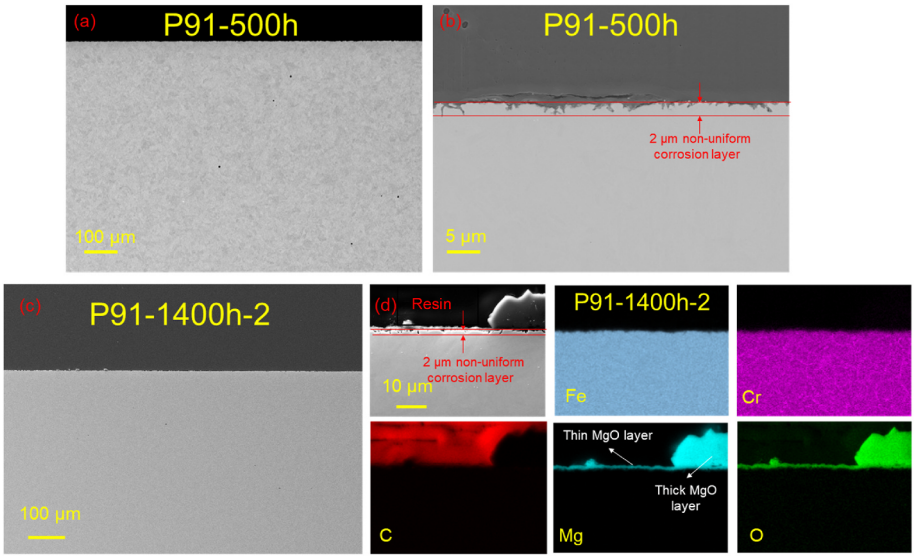

Fig. 5. SEM-EDX images of P91 samples without descaling. (a) and (b) the cross-section of P91-500 h sample with different magnification; (c) the cross-section of P91-1400h-2 sample; (d) the EDX analysis of P91-1400h-2 sample.

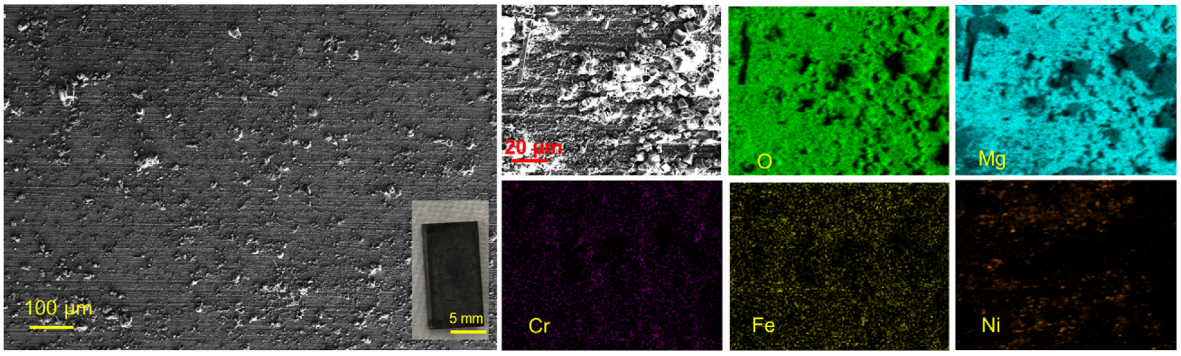

Fig. 6. Surface morphology of sample SS304-1400h-2 analysed by SEM and EDX.

have been seen as the initiators of pitting corrosion in numerous references [40–42]. Hence, it is a high possibility that selective corrosion along the MnS phases occurred in SS 304 samples. The average CR is 394 μm/year (63 μm/1400 h) for sample SS304-1400h-2, based on the selective corrosion observed by SEM, as shown in Fig. 7 (c).

3.2. *Impurities in salts measured by titration and AAS*

MgOHCl is considered the main corrosive impurity in the $MgCl_2$-KCl-NaCl molten salt. The concentrations of MgOHCl in each crucible before and after the exposure test were determined by titration and are shown in Fig. 8. Concentrations of MgOHCl of five salt samples are smaller than 130 ppm O, and three other samples were larger than 240 ppm O. The differences in oxygen content are likely to originate from the inevitable diffusion of air during salt and steel sampling, where the sweep gas can be contaminated with moisture and atmospheric oxygen. The moisture can react with the molten chloride salt, as shown in Eq. (7), leading to increase concentrations of MgOHCl. For example, the salt samples were

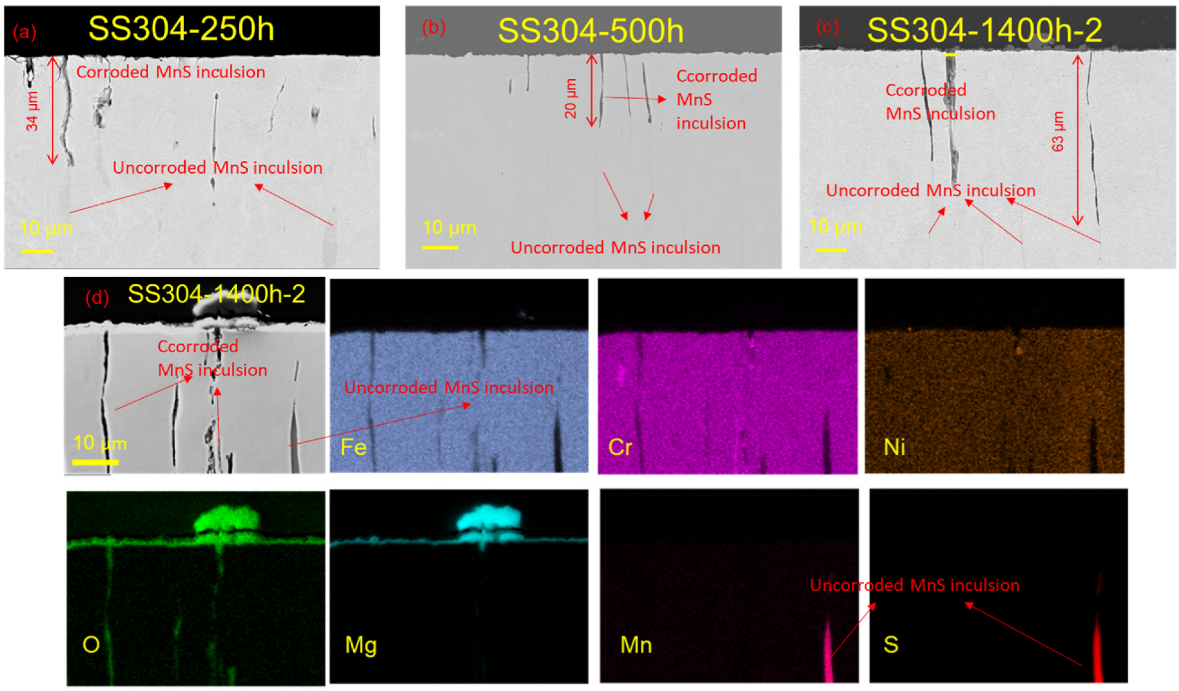

Fig. 7. Cross-section of samples SS 304-250 h, SS 304–500 h, and SS 304-1400h-2 analysis by SEM-EDX. (a), (b) and (c) the cross-section of SS304 samples with different exposure time; (d) the EDX analysis of SS304-1400h-2 sample.

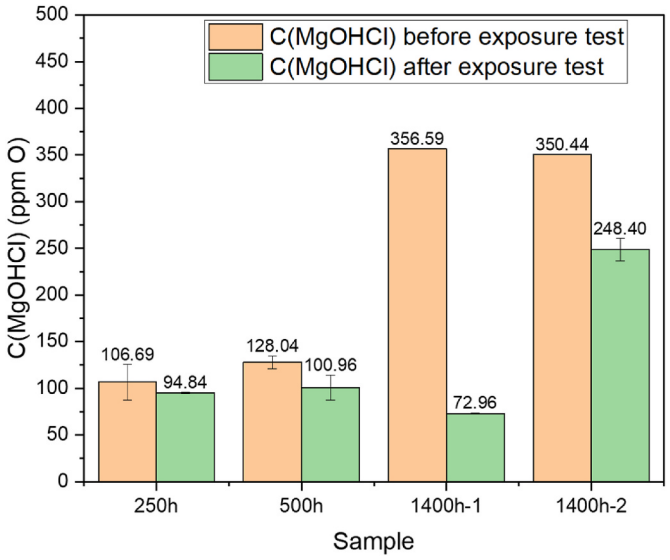

Fig. 8. Concentration of corrosive impurity MgOHCl in tested chloride salts before/after metal samples were immersed.

extracted from each crucible one by one for about 15 min before the metal samples were immersed in molten salt, as shown in Fig. 2 (b). MgOHCl concentration in samples increased from ~100 ppm O to ~350 ppm O. After closing the set-up, the MgOHCl concentration decreased from ~350 ppm O to ~100 ppm O, according to the reaction shown in Eq. (5).

$$MgCl_{2(l)} + H_2O_{(g/l)} \rightarrow MgOHCl_{(s)} + HCl_{(g)} \quad (7)$$

The presence of corrosion products (Fe, Cr, and Ni ions) in salt samples serves as an indicator for corrosion analysis. In addition, it is known that the presence of Fe and Cr ions can actually exacerbate corrosion, as noted in previous studies [43,44]. In this study, the elements of Cr, Fe, and Ni in the molten chloride salt after the exposure test are determined by AAS, as shown in Fig. 9. The concentrations of Cr, Fe, and Ni are smaller than 0.003 mol. % in the salt samples. The AAS results in this work are comparable to our previous work, which showed only marginal corrosion on the Fe-Cr-Ni alloy at 700 °C in molten chloride [9]. The low concentrations of corrosion products indicate that the corrosion of the metal samples was well controlled. Additionally, such small concentrations of corrosion products would have a negligible impact on accelerating corrosion.

4. Discussion

4.1. Corrosion mechanism and corrosion control strategy

The corrosion mechanism of steel in molten chloride salt can be

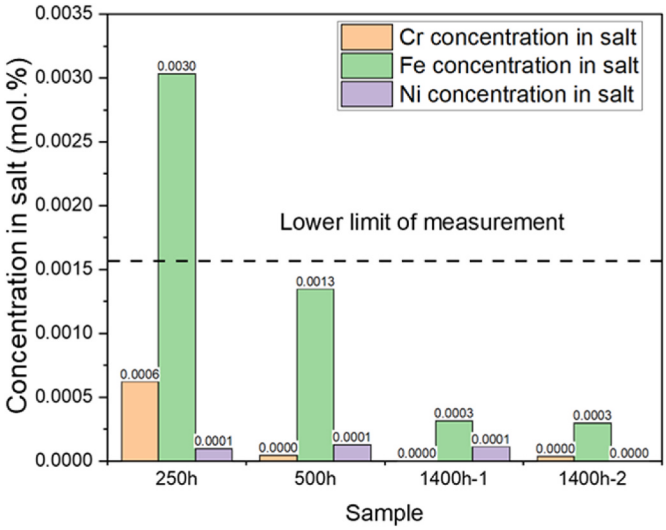

Fig. 9. The Cr, Fe, and Ni elements concentration in the salt after the 250 h, 500 h, and 1400 h exposure test.

summarized as the reactions between corrosive impurities with high redox potential and the relatively active metal [10,12,15,19]. For example, the corrosive MgOHCl in $MgCl_2$-containing salt can react with Cr, Fe, Mn, and Ni in the steel, resulting in corrosion, as shown in Eq. (5).

In this work, the SS 304 samples showed deep selective corrosion, as demonstrated in Fig. 7. The corrosion of SS 304 in this work can be explained as follow. First, according to the formation Gibbs formation energy of chlorides shown in Fig. 10 (a), Mn has the highest activity among the metals in the SS 304. In addition, as a common inclusion in SS 304, the MnS inclusion was found and investigated in numerous references [39,41,42,45]. For example, M. Nishimoto et al. display the SEM-EDX analysis of MnS, in which the width of MnS inclusion is about 5 μm while the length can as long as 60 μm [39], consisting with that shown in Fig. 7 in this study. In some corrosion research, the MnS inclusion in stainless steel is the pit initiation of steel in aqueous solutions [41,42], which might also be true for the molten chloride salt system. As shown in Fig. 10 (b), the MnS inclusions lead to the enrichment of Mn in SS 304 samples. The corrosive MgOHCl prioritizes attacking the MnS inclusions in the samples, leading to deep selective corrosion. The possible reactions of such corrosion processes can be written as Eq. (8), Eq. (9), and Eq. (10), where the Gibbs free energy at 500 °C for each reaction is queried from the thermodynamic databases software FactSage™. According to the Gibbs free energy, the greatest possibility is that the free Mn and S elements in the MnS inclusions reacted with MgOHCl and caused corrosion, as shown in Eq. (8) and Eq. (9). Alternatively, the MnS inclusion can react with HCl generated by hydrolysis of $MgCl_2{\cdot}H_2O$, as shown in Eq. (11). However, the corrosion mechanism of MnS as pit initiation in molten chloride salt needs to be explored more systematically, the reactions with Gibbs free energy listed here would be references in the future. Despite the deep selective corrosion in SS 304 samples, the average corrosion indicated by mass loss is small due to the limited MgOHCl amount in the chloride salts. This case illustrates that steel corrosion must be evaluated microscopic and macroscopic to avoid misinterpretation of results.

$$Mn_{(s)} + 2MgOHCl_{(l)} \rightarrow 2MgO_{(s)} + MnCl_{2(s)} + H_{2(g)}\ \Delta G = -165.4\ \text{kJ/mol}\ (500\ ^\circ\text{C}) \quad (8)$$

$$Mn_{(s)} + S_{(s)} + 2MgOHCl_{(l)} \rightarrow 2MgO_{(s)} + MnCl_{2(s)} + H_2S_{(g)}\ \Delta G = -210.7\ \text{kJ/mol}\ (500\ ^\circ\text{C}) \quad (9)$$

$$MnS_{(s)} + 2MgOHCl_{(l)} \rightarrow 2MgO_{(s)} + MnCl_{2(s)} + H_2S_{(g)}\ \Delta G = +10.8\ \text{kJ/mol}\ (500\ ^\circ\text{C}) \quad (10)$$

$$MnS_{(s)} + HCl_{(g)} \rightarrow MnCl_{2(s)} + H_2S_{(g)}\ \Delta G = -5.04\ \text{kJ/mol}\ (500\ ^\circ\text{C}) \quad (11)$$

The P91 steel (also called T91, 1.4903) is typical ferritic-martensitic steel. It is generally accepted that Ni positively affects the corrosion resistance of steel in molten chloride salt [3,12,19] due to its low metallic activity. However, as shown in Fig. 5, the P91 samples, even though it does not contain Ni, showed minimal corrosion in the purified molten $MgCl_2$-KCl-NaCl at 500 °C. The measured CRs of P91 in this work can be as small as 1.5 μm/year (P91-1400h-1) in purified molten chloride salt at 500 °C, much below the target of 15 μm/year proposed by the department of energy (DOE) [38]. This is ascribed to the corrosion control strategy, which reduces the corrosive MgOHCl impurity levels to ~100 ppm O, as presented in this work. Similar conclusions have been drawn in the previous work on steel in molten chloride salt at 700 °C [9,13]. The purification strategy of the molten chloride salt is crucial to mitigate corrosion [4,9].

There is an unexpected phenomenon that the Sample P91-250 h has larger mass loss than that of the Sample-1400h-1, as shown in Fig. 3. In addition, as shown in Fig. 9, the concentration of corrosion products Fe ions in 250 h crucible is higher than that of the 1400h-1 crucible, which is consistent with the corrosion analysis based on mass loss. This may be related to the distribution of Mg inhibitor in the crucible during the exposure test. Fig. 11 displays the Mg residue on the sample holders freshly lifted out of the crucible. From the photographs it can be see that the alloy samples in 1400h-1 crucible were closer to the Mg inhibitor than those in 250 h crucible. Therefore, the Sample P91-1400h-1 is better protected by Mg than the Sample P91-250 h.

4.2. Material selection for cold tank of chloride-TES

For the operating temperature of ~500 °C, two types of steels can be selected: ferritic-martensitic steels (e.g., P91) and austenitic stainless steels (e.g., 300-series stainless steels), from the aspect of mechanical properties. The maximal allowable stress of some types of steel is summarized in Fig. 12(a), according to the ASME Boiler And Pressure Vessel Code 2010 [17]. The mechanical property of the cold tank of commercial nitrate-TES is selected as the reference, i.e., the maximal allowable stress of the carbon steel SA-516 at 300 °C is 115 MPa [1,17] which is marked as the dashed line in Fig. 12 (a). Austenitic stainless steels typically have the allowable stress of <120 MPa, while the

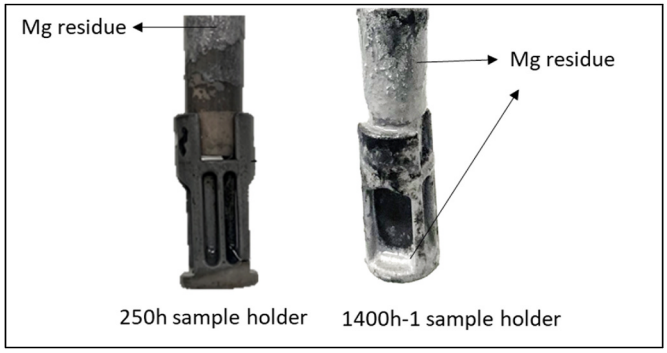

Fig. 11. The photographs of sample holders for 250 h and 1400h-1 freshly lifted out of the crucible. The Mg residue on 1400h-1 sample holder is closer to the alloy samples than 250 h sample holder.

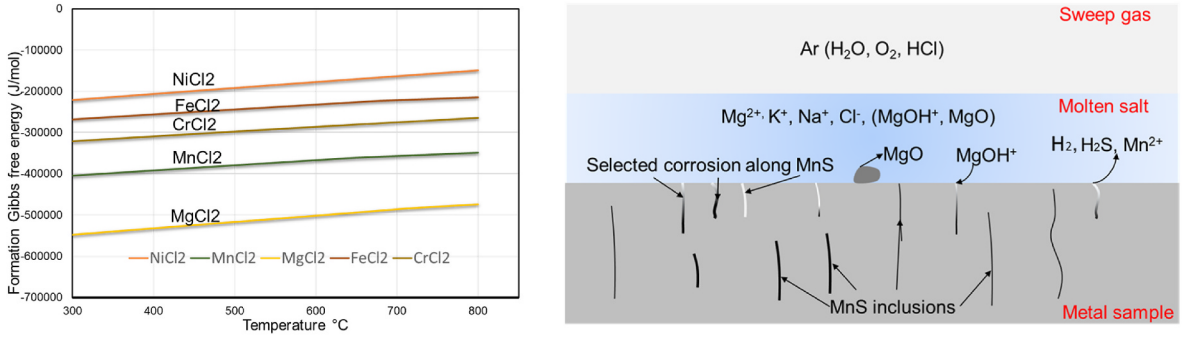

Fig. 10. (a) The formation Gibbs free energy of chlorides at high temperature based on FactSage™ databases. (b) Schematic diagram of the corrosion mechanism of Mn selective corrosion in the SS 304 samples.

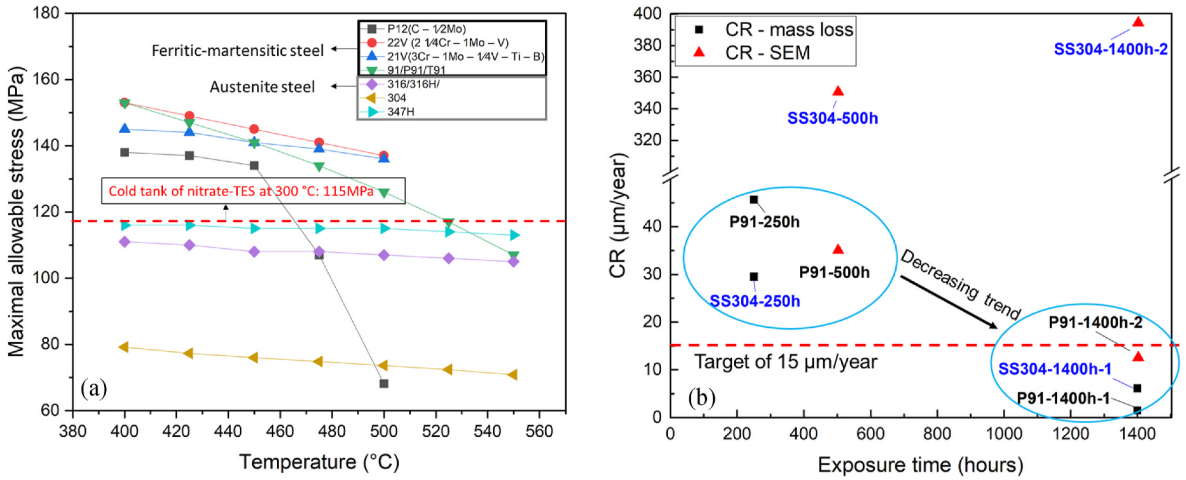

Fig. 12. (a)The maximal allowable stress of candidate steel for cold tank of chloride-TES. Data sources: ASME code [17]. (b) The CRs of P91 and SS 304 in this work. The CR target was proposed by DOE [38].

ferritic-martensitic steels have ~140 MPa allowable stress, which is even higher than that of SA-516 at 300 °C.

It is often assumed that austenitic stainless steels show better corrosion resistance in oxidizing and corrosive environments but that it is more costly than ferritic-martensitic steel. For example, the cost of 300-series stainless steel is four times higher than that of P91 [33]. However, the corrosion results in this work indicate that the CR of P91 is lower than that of SS 304 in molten chloride salt with a proper corrosion control strategy at 500 °C, as summarized in Fig. 12 (b). Due to the deep pitting of SS 304 along the MnS inclusion, the CRs of SS 304 in this work can be as high as 394 μm/year. On the contrary, the CRs of both mass loss and SEM for P91 steel are smaller than 15 μm/year, reaching the CR target of the DOE [38]. In addition, the CRs of P91 in this work show a decreasing trend with increase exposure time, indicating that the further decrease potential of CRs for long-term service. Moreover, P91 shows the advantages of cost-effectiveness coupled with sufficient mechanical properties. When the P91 steel is used instead of SS 347H proposed in Ref. [1], the cost would be reduced to a quarter, i.e., from 8 $/kWh-th to 2 $/kWh-th for chloride-TES. This cold tank material cost is comparable to nitrate-TES made from carbon steel (1.6 $/kWh-th), which can be calculated based on data in Ref. [1]. Hence, in a chloride-TES with a corrosion control approach [4,9], ferritic-martensitic steels, represented by P91, can be selected as the cold tank structural material.

5. Conclusions and outlook

In this work, the samples of ferritic-martensitic steel (P91) and austenitic stainless steel (SS 304) were investigated as the cold tank material candidates for chloride-TES using corrosion mitigation with Mg. The steel samples were exposed to Mg-purified $MgCl_2$-KCl-NaCl molten salt at 500 °C isothermally for 1400 h. Some conclusions can be drawn as follows.

1. The corrosion analysis based on mass loss demonstrates that both P91 and SS 304 steel show limited degradation (<10 μm/year) in molten $MgCl_2$-KCl-NaCl at 500 °C for 1400 h.
2. The microanalysis based on SEM-EDX images shows deep pitting corrosion along the MnS inclusion in the body of SS 304 on the cross-section. Because of the pitting, the CR of SS 304 is 394 μm/year based on the microanalysis. Thus, special attention is suggested to give on the corrosion due to MnS in the alloys such as SS304 with MnS inclusion. No selective corrosion in the samples of P91 was observed. Thus, the CR of P91 is 12.5 μm/year based on the microanalysis of 1400-h exposure test.
3. According to the analysis of the salt samples, the concentration of corrosive impurity MgOHCl was smaller than <100 ppm O (0.05 wt %) during most test phases. The increase in the concentration was observed after frequent sampling with the peak MgOHCl concentration of ~350 ppm O. Fe-, Cr-, and Ni-ions corrosion products were typically smaller than 0.003 mol.% in the salt samples.
4. The ferritic-martensitic steel P91 is recommended as a promising candidate for the cold tank of chloride-TES, based on the corrosion results in this work, the cost of steel, and the high-temperature mechanical properties. When P91 can be used as the primary structural material, the material cost of the cold tank for chloride-TES would be comparable to that of commercial nitrate-TES.

CRediT authorship contribution statement

Qing Gong: Writing – original draft, Visualization, Methodology, Investigation, Conceptualization. **Andrea Hanke:** Writing – review & editing, Methodology, Investigation. **Fiona Kessel:** Writing – review & editing, Methodology, Investigation. **Alexander Bonk:** Writing – review & editing, Methodology, Investigation. **Thomas Bauer:** Writing – review & editing, Funding acquisition. **Wenjin Ding:** Writing – review & editing, Supervision, Project administration, Methodology, Investigation, Funding acquisition.

Declaration of competing interest

The authors declare the following financial interests/personal relationships which may be considered as potential competing interests:

Qing Gong reports financial support was provided by German Academic Exchange Service.

Data availability

Data will be made available on request.

Acknowledgement

This research is supported by German Academic Exchange Service by DLR-DAAD fellowship program (Nr. 57540125). The authors would like to thank M. Braun and R. Hoffmann for support in the different laboratories.

References

[1] M. Mehos, C. Turchi, J. Vidal, M. Wagner, Z. Ma, C. Ho, W. Kolb, C. Andraka, A. Kruizenga, Concentrating Solar Power Gen3 Demonstration Roadmap, National Renewable Energy Lab.(NREL), Golden, CO (United States), United States, 2017, https://doi.org/10.2172/1338899.

[2] W. Ding, T. Bauer, Progress in Research and Development of Molten Chloride Salt Technology for Next Generation Concentrated Solar Power Plants, Engineering, 2021, https://doi.org/10.1016/j.eng.2020.06.027.

[3] C. Turchi, S. Gage, J. Martinek, S. Jape, K. Armijo, J. Coventry, J. Pye, C.-A. Asselineau, F. Venn, W. Logie, CSP Gen3: Liquid-phase Pathway to SunShot, National Renewable Energy Lab.(NREL), Golden, CO (United States), 2021, https://doi.org/10.2172/1807668.

[4] C. Villada, W. Ding, A. Bonk, T. Bauer, Engineering molten MgCl2–KCl–NaCl salt for high-temperature thermal energy storage: review on salt properties and corrosion control strategies, Sol. Energy Mater. Sol. Cell. 232 (2021), 111344, https://doi.org/10.1016/j.solmat.2021.111344.

[5] T. Bauer, C. Odenthal, A. Bonk, Molten salt storage for power generation, Chem. Ing. Tech. 93 (2021) 534–546, https://doi.org/10.1002/cite.202000137.

[6] A. Bonk, S. Sau, N. Uranga, M. Hernaiz, T.J.P.i.E. Bauer, C. Science, Advanced heat transfer fluids for direct molten salt line-focusing CSP plants 67 (2018) 69–87, https://doi.org/10.1016/j.pecs.2018.02.002.

[7] Q. Liu, H. Xu, H. Yin, N. Li, W. Wang, L. Li, Z. Tang, Y. Qian, Corrosion behaviour of 316 stainless steel in NaCl-KCl-MgCl2 salt vapour at 700°C, Corrosion Sci. 194 (2022), 109921, https://doi.org/10.1016/j.corsci.2021.109921.

[8] X. Li, T. Xu, M. Liu, Y. Song, Y. Zuo, Z. Tang, L. Yan, J. Wang, Thermodynamic and kinetic corrosion behavior of alloys in molten MgCl2–NaCl eutectic: FPMD simulations and electrochemical technologies, Sol. Energy Mater. Sol. Cell. 238 (2022), 111624, https://doi.org/10.1016/j.solmat.2022.111624.

[9] Q. Gong, H. Shi, Y. Chai, R. Yu, A. Weisenburger, D. Wang, A. Bonk, T. Bauer, W. Ding, Molten chloride salt technology for next-generation CSP plants: compatibility of Fe-based alloys with purified molten MgCl2-KCl-NaCl salt at 700 °C, Appl. Energy 324 (2022), 119708, https://doi.org/10.1016/j.apenergy.2022.119708.

[10] W. Ding, A. Bonk, T. Bauer, Corrosion behavior of metallic alloys in molten chloride salts for thermal energy storage in concentrated solar power plants: a review, Front. Chem. Sci. Eng. 12 (2018) 564–576. https://10.1007/s11705-018-1720-0.

[11] G. Mohan, M. Venkataraman, J. Gomez-Vidal, J. Coventry, Assessment of a novel ternary eutectic chloride salt for next generation high-temperature sensible heat storage, Energy Convers. Manag. 167 (2018) 156–164, https://doi.org/10.1016/j.enconman.2018.04.100.

[12] Y. Zhao, Molten Chloride Thermophysical Properties, Chemical Optimization, and Purification, National Renewable Energy Lab.(NREL), Golden, CO (United States), 2020. https://www.osti.gov/biblio/1734652.

[13] J.M. Kurley, P.W. Halstenberg, A. McAlister, S. Raiman, S. Dai, R.T. Mayes, Enabling chloride salts for thermal energy storage: implications of salt purity, RSC Adv. 9 (2019) 25602–25608, https://doi.org/10.1039/C9RA03133B.

[14] B.A. Pint, J.W. McMurray, A.W. Willoughby, J.M. Kurley, S.R. Pearson, M.J. Lance, D.N. Leonard, H.M. Meyer, J. Jun, S.S. Raiman, Re-establishing the paradigm for evaluating halide salt compatibility to study commercial chloride salts at 600°C–800°C, Mater. Corros. 70 (2019) 1439–1449, https://doi.org/10.1002/maco.201810638.

[15] B. Pint, Progression to Compatibility Evaluations in Flowing Molten Salts, Office of Scientific and Technical Information (OSTI), 2020, https://doi.org/10.2172/1649281.

[16] B. Grégoire, C. Oskay, T. Meißner, M. Galetz, Corrosion mechanisms of ferritic-martensitic P91 steel and Inconel 600 nickel-based alloy in molten chlorides. Part II: NaCl-KCl-MgCl2 ternary system, Sol. Energy Mater. Sol. Cell. 216 (2020), 110675, https://doi.org/10.1016/j.solmat.2020.110675.

[17] ASME, ASME boiler and pressure vessel code 2010, in: ASME BPVC (2010), ASME, New York, 2010.

[18] H. Susskind, F. Hill, L. Green, S. Kalish, L. Kukacka, W. McNulty, E. Wirsing Jr., Corrosion Studies for a Fused Salt-Liquid Metal Extraction Process for the Liquid Metal Fuel Reactor, Brookhaven National Lab., Upton, NY, 1960, https://doi.org/10.2172/4023508.

[19] W. Ding, H. Shi, Y. Xiu, A. Bonk, A. Weisenburger, A. Jianu, T. Bauer, Hot corrosion behavior of commercial alloys in thermal energy storage material of molten MgCl2/KCl/NaCl under inert atmosphere, Sol. Energy Mater. Sol. Cell. 184 (2018) 22–30, https://doi.org/10.1016/j.solmat.2018.04.025.

[20] K. Robb, Simplified High-Temperature Molten Salt CSP Plant Preconceptual Design, Office of Scientific and Technical Information (OSTI), 2022, https://doi.org/10.2172/1856690.

[21] B. Grégoire, C. Oskay, T.M. Meißner, M.C. Galetz, Corrosion performance of slurry aluminide coatings in molten NaCl–KCl, Sol. Energy Mater. Sol. Cell. 223 (2021), 110974, https://doi.org/10.1016/j.solmat.2021.110974.

[22] S.S. Raiman, R.T. Mayes, J.M. Kurley, R. Parrish, E. Vogli, Amorphous and partially-amorphous metal coatings for corrosion resistance in molten chloride salt, Sol. Energy Mater. Sol. Cell. 201 (2019), 110028, https://doi.org/10.1016/j.solmat.2019.110028.

[23] W. Ding, H. Shi, A. Jianu, Y. Xiu, A. Bonk, A. Weisenburger, T. Bauer, Molten chloride salts for next generation concentrated solar power plants: mitigation strategies against corrosion of structural materials, Sol. Energy Mater. Sol. Cell. 193 (2019) 298–313, https://doi.org/10.1016/j.solmat.2018.12.020.

[24] S. Abu Kassim, J.A. Thor, A. Abu Seman, T.K. Abdullah, High temperature corrosion of Hastelloy C22 in molten alkali salts: the effect of pre-oxidation treatment, Corrosion Sci. 173 (2020), 108761, https://doi.org/10.1016/j.corsci.2020.108761.

[25] W. Ding, Y. Shi, M. Braun, F. Kessel, M. Frieß, A. Bonk, T.J.E. Bauer, Compatibility of 3D-printed oxide ceramics with molten chloride salts for high-temperature thermal energy storage in next-generation, CSP Plants 14 (2021) 2599, https://doi.org/10.3390/en14092599.

[26] W. Ding, Y. Shi, F. Kessel, D. Koch, T. Bauer, Characterization of corrosion resistance of C/C–SiC composite in molten chloride mixture MgCl2/NaCl/KCl at 700 °C, npj Materials Degradation 3 (2019) 42, https://doi.org/10.1038/s41529-019-0104-3.

[27] S.H. Gage, D. Kesseli, J. Dupree, C. Kimbal, J. Rigby, J. Yates, B. Morrison, G. Bigham, C.S. Turchi, Technical and economic feasibility of molten chloride salt thermal energy storage systems, Sol. Energy Mater. Sol. Cell. 226 (2021), 111099, https://doi.org/10.1016/j.solmat.2021.111099.

[28] Y. Zhao, J. Vidal, Potential scalability of a cost-effective purification method for MgCl2-Containing salts for next-generation concentrating solar power technologies, Sol. Energy Mater. Sol. Cell. 215 (2020), 110663, https://doi.org/10.1016/j.solmat.2020.110663.

[29] Y. Zhao, N. Klammer, J. Vidal, Purification strategy and effect of impurities on corrosivity of dehydrated carnallite for thermal solar applications, RSC Adv. 9 (2019) 41664–41671, https://doi.org/10.1039/C9RA09352D.

[30] W. Ding, J. Gomez-Vidal, A. Bonk, T. Bauer, Molten chloride salts for next generation CSP plants: electrolytical salt purification for reducing corrosive impurity level, Sol. Energy Mater. Sol. Cell. 199 (2019) 8–15, https://doi.org/10.1016/j.solmat.2019.04.021.

[31] B. Garcia-Diaz, M. Martinez-Rodriguez, Full Loop Thermodynamic Corrosion Inhibition and Sensing in Molten Chloride Systems, Office of Scientific and Technical Information (OSTI), 2020, https://doi.org/10.2172/1734665.

[32] M. Zhang, J. Ge, T. Yin, J. Zhang, Redox potential measurements of Cr (II)/Cr Ni (II)/Ni and Mg (II)/Mg in molten MgCl2–KCl–NaCl mixture, J. Electrochem. Soc. 167 (2020), 116505, https://doi.org/10.1149/1945-7111/aba15a.

[33] A. Soleimani Dorcheh, R.N. Durham, M.C. Galetz, Corrosion behavior of stainless and low-chromium steels and IN625 in molten nitrate salts at 600°C, Sol. Energy Mater. Sol. Cell. 144 (2016) 109–116, https://doi.org/10.1016/j.solmat.2015.08.011.

[34] ASTM-G1-03, Standard Practice for Preparing, Cleaning, and Evaluating Corrosion Test Specimens, 1999.

[35] Q. Gong, W. Ding, Y. Chai, A. Bonk, J. Steinbrecher, T. Bauer, Chemical analysis and electrochemical monitoring of extremely low-concentration corrosive impurity MgOHCl in molten MgCl2–KCl–NaCl, Front. Energy Res. 10 (2022), https://doi.org/10.3389/fenrg.2022.811832.

[36] M. Lambrecht, M.T. de Miguel, M.I. Lasanta, F.J. Pérez, Past research and future strategies for molten chlorides application in concentrated solar power technology, Sol. Energy Mater. Sol. Cell. 237 (2022), 111557, https://doi.org/10.1016/j.solmat.2021.111557.

[37] S. Ren, Y. Chen, X.-X. Ye, L. Jiang, S. Yan, J. Liang, X. Yang, B. Leng, Z. Li, Z. Chen, Corrosion behavior of carburized 316 stainless steel in molten chloride salts, Sol. Energy 223 (2021) 1–10, https://doi.org/10.1016/j.solener.2021.05.057.

[38] B.L. Garcia-Diaz, L. Olson, M. Martinez-Rodriguez, R. Fuentes, H. Colon-Mercado, J. Gray, High temperature electrochemical engineering and clean energy systems, Journal of the South Carolina Academy of Science 14 (2016) 4. https://scholarcommons.sc.edu/jscas/vol14/iss1/4.

[39] M. Nishimoto, I. Muto, Y. Sugawara, N. Hara, Passivity of (Mn,Cr)S inclusions in type 304 stainless steel: the role of Cr and the critical concentration for preventing inclusion dissolution in NaCl solution, Corrosion Sci. 176 (2020), 109060, https://doi.org/10.1016/j.corsci.2020.109060.

[40] R. Ke, R. Alkire, Surface analysis of corrosion pits initiated at MnS inclusions in 304 stainless steel, J. Electrochem. Soc. 139 (1992) 1573–1580, https://doi.org/10.1149/1.2069458.

[41] A. Chiba, I. Muto, Y. Sugawara, N. Hara, Pit initiation mechanism at MnS inclusions in stainless steel: synergistic effect of elemental sulfur and chloride ions, J. Electrochem. Soc. 160 (2013) C511–C520, https://doi.org/10.1149/2.081310jes.

[42] J.H. Park, Y. Kang, Inclusions in stainless steels – A review, Steel Res. Int. 88 (2017), 1700130, https://doi.org/10.1002/srin.201700130.

[43] P. Lu, Q. Liu, H. Bao, T.J. Pan, Z. Tang, Effect of FeCl3 in NaCl-MgCl2 molten salts on the corrosion behavior of 316 stainless steel at 600 °C, Corrosion Sci. 212 (2023), 110961, https://doi.org/10.1016/j.corsci.2023.110961.

[44] B.L. Garcia-Diaz, Fundamental Corrosion Studies in High-Temperature Molten Salt Systems for Next Generation Concentrated Solar Power Systems, Office of Scientific and Technical Information (OSTI), 2016, https://doi.org/10.2172/1491796.

[45] Q. Meng, G.S. Frankel, H.O. Colijn, S.H. Goss, Stainless-steel corrosion and MnS inclusions, Nature 424 (2003) 389–390, https://doi.org/10.1038/424389b.

3 Methods

This chapter will provide a general overview of the methods, while the details are shown in three journal papers.

3.1 MgOHCl measurement

Fig. 6 shows the flowchart of the MgOHCl measurement in molten $MgCl_2$-KCl-NaCl (47.1–30.2–22.7 mol.%, 56.5–22.2–21.3 wt.%) at 500, 600, 700 °C. In order to obtain the concentration gradient of MgOHCl, the electrolysis method was carried out for the experiments at 500 °C, as shown in Eq. 13 and Eq. 14. Similarly, the concentration gradients of MgOHCl were obtained through thermal decomposition after a certain waiting time since MgOHCl decomposes to MgO and HCl at the temperature of > 555 °C, as shown in Eq. 5. For each concentration of MgOHCl, a CV experiment was performed to record the electrical signal in the molten chloride salt. After the CV experiment, a salt sample was extracted and titrated to measure the concentration of MgOHCl.

$$Cathode(Reduction): 2MgOH^+ + 2e^- \rightarrow 2MgO(s) + H_2(g) \quad \text{Eq. 13}$$

$$Anode\ (Oxidation): Cl^- \rightarrow Cl_2(g) + 2e^- \quad \text{Eq. 14}$$

By combing the signals of MgOHCl measured by CV and results of the titration, the relationship between the electrochemical signal and the concentration was identified, then the MgOHCl can be measured by CV in-situ. There are two difficulties with this series of experiments. Firstly, the lower limit of measurement of MgOHCl depends on the accuracy of the titration. It is significant to develop a more accurate titration method than the available MgOHCl measurement methods. Secondly, measurements based on CV often have problems of electrode passivation, which can lead to deviation of electrochemical signal. In this work, the electrodes most susceptible to passivation were renewed after each CV experiment.

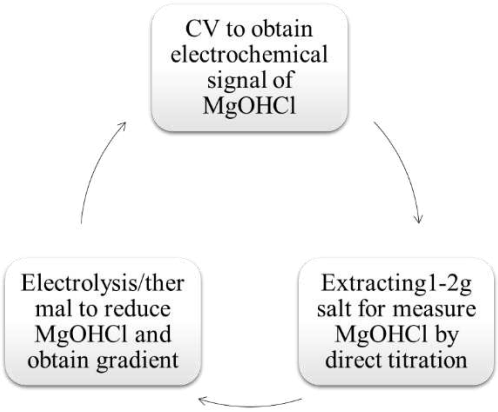

Fig. 6. Flowchart of CV-titration experiments for the MgOHCl measurement in/ex-situ in molten $MgCl_2$-KCl-NaCl salt.

3.2 Compatibility research of alloys with purified salt

In Paper II and III, exposure test of metal in molten salt is carried out to study the compatibility of metal samples with molten $MgCl_2$-KCl-NaCl (47.1–30.2–22.7 mol.%) at 500 °C and 700 °C, corresponding to the hot and cold parts of chloride-TES. The molten chloride salts were purified by 2.8 wt.% liquid Mg at 700 °C for 16 hours under sweep gas of argon. After purification, the prepared metal samples were immersed in the molten salt for 1400 hours and 2000 hours at 500 °C and 700 °C, respectively. Some samples were lifted out in order to study the corrosion trend, during the thousands of hours exposure test. After each sample was taken out, the corresponding 1-2 g salt sample was extracted for the post-analysis by direct titration shown in Paper I and atomic absorption spectroscopy (AAS).

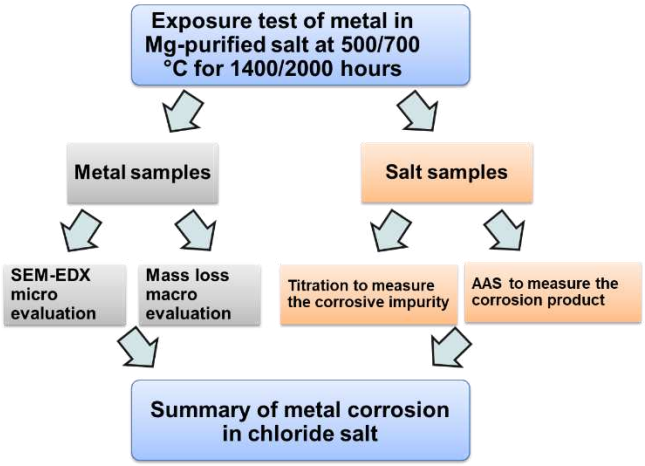

Fig. 7. Flowchart of the compatibility study of metal samples with purified salt. The corrosivity of salts and the corrosion of metal samples were evaluated separately.

4 Results and Discussion

4.1 Results

The core results of this thesis can be summarised in one sentence. Corrosion of molten salts at 500 - 700 °C has been controlled by an improved molten salt purification technique, which has reduced the corrosion rates of commercial structural materials (e.g., stainless steel) to an acceptable range of less than 15 μm/year. Firstly, as shown in Paper I, a highly accurate measurement of MgOHCl, a corrosive impurity in molten $MgCl_2$-KCl-NaCl, was developed based on the direct titration methods. The direct titration using a high-precision automatic titrator can detect the MgOHCl concentration at the tens of ppm O level. Secondly, a purification method of molten chloride salt was optimized based on the previous work [31], as shown in Paper II and Paper III. With such method, the concentration of MgOHCl in molten chloride salt can be smaller than hundreds of ppm O, resulting in a significantly reduction of corrosion rates of stainless steel in molten chloride salt from thousands of microns per year to less than 15 microns per year, achieving the standard of CR for a 30-year life.

4.1.1 Monitoring of Extremely Low-Concentration Corrosive Impurity MgOHCl in Molten $MgCl_2$–KCl–NaCl

According to the direct titration results in Paper I, the MgOHCl can be measured at the tens of ppm O level by the direct titration method. The error analysis of such titration shows that when the MgOHCl concentration in about 500 mg salt samples is 36.1 ppm O, the average error is +6.62 ppm O and the average standard deviation is 4.35 ppm O, as shown **Fig. 8**. This method has one to two orders of magnitude more accuracy than other MgOHCl measurement methods[53,55].

The obtained current density of peak B for 500–700°C shows good linearity with the data on direct titration (i.e., MgOHCl concentration) in the range from 39 to 4211 ppm O. The slope of the concentration of MgOHCl (obtained by titration) vs. the peak current density in CV (shown in **Fig. 9**) was 7.2 ±2 (ppm O)/(mA/cm^2) at 500–700°C, as shown in **Fig. 10**.

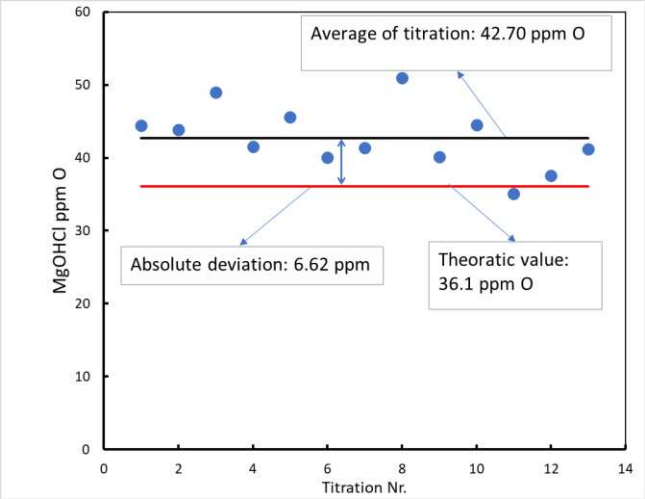

Fig. 8. Thirteen times direct titration experiments with the standard MgOHCl solution to determine RSD and relative error at a concentration equivalent 36 ppm O in 500mg salt sample.

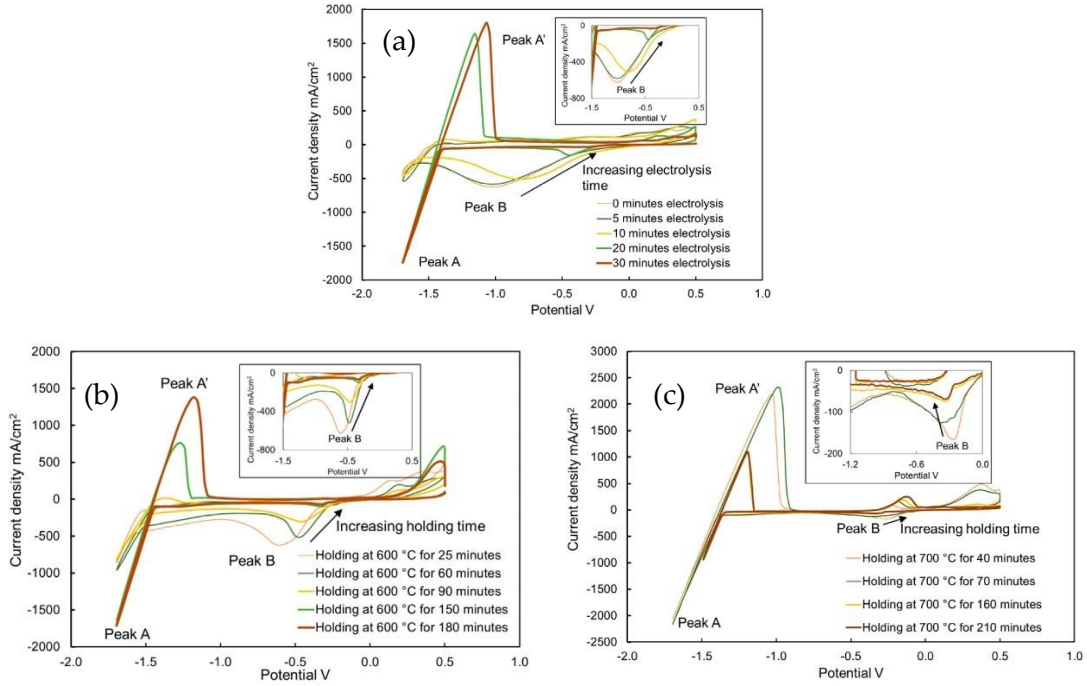

Fig. 9. Cyclic voltammograms in molten chloride salt at 500 °C (a), 600 °C (b), and 700 °C (c). The MgOHCl concentration gradients are generated by electrolysis at 500 °C, and thermal decomposition at 600 and 700 °C. The current density of Peak B which is the feature peak of MgOHCl is recorded at different concentration of MgOHCl.

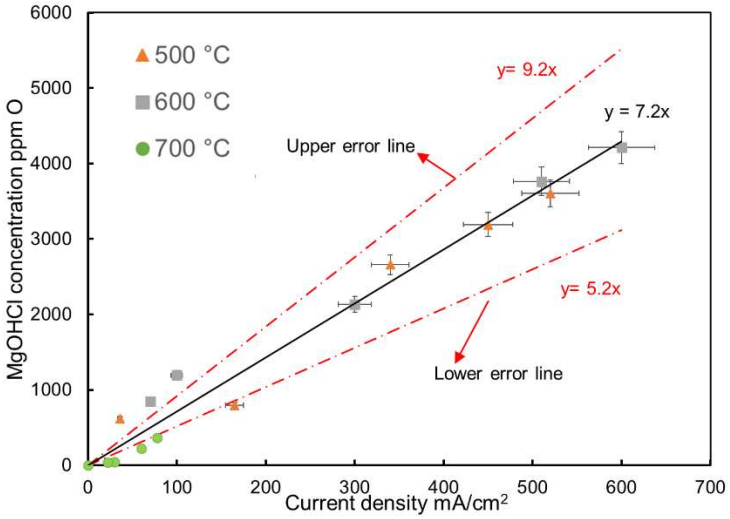

Fig. 10. Relationship between current density of Peak B and MgOHCl concentration obtained by titration.

4.1.2 Analysis of purified chloride salt

Before the immersion/exposure tests in Paper II and Paper III, the molten $MgCl_2$-KCl-NaCl salts were purified by ~2.8 wt.% liquid Mg at 700 °C for 16 hours. As can be seen from the Fig 11, the titration analysis developed in Paper I shows that the concentrations of MgOHCl in test salt are hundreds of ppm O, which are significantly reduced comparing with that in unpurified salt (> 3000 ppm O MgOHCl). In addition, after the exposure tests, the concentrations of MgOHCl are comparable with those before exposure tests, indicating the stable test environment with argon sweeping gas. In other words, the metal samples in these series experiments face with low corrosive molten chloride salts during the immersion tests.

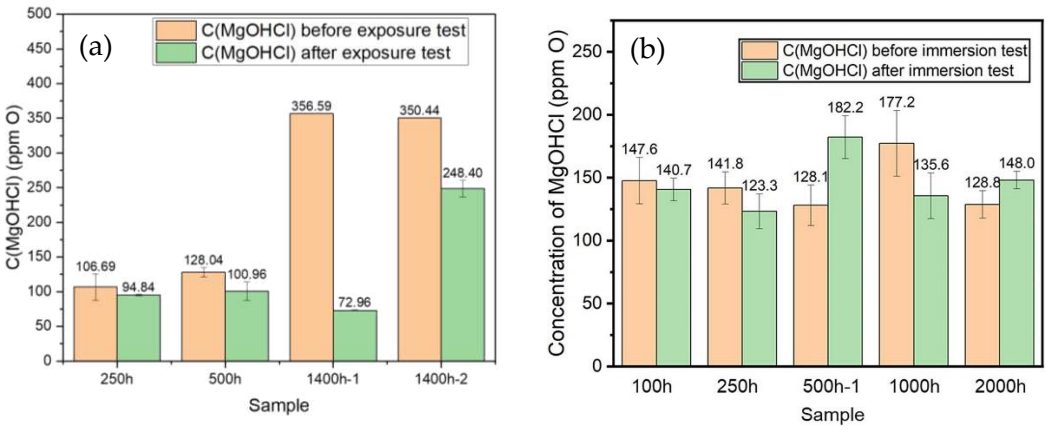

Fig. 11. Concentration of corrosive impurity MgOHCl in tested chloride salts before/after metal samples were immersed. (a) the immersion tests are carried out at 500 °C shown in Paper III; (b) the immersion tests are carried out at 700 °C shown in Paper II

4.1.3 Corrosion of Fe-based alloy in purified chloride salt

In paper II, it is experimentally proved that Fe-based alloys (SS310 and In 800H) can reach the CR target of 15 μm/year in $MgCl_2$-KCl-NaCl mixtures at 700 °C with Mg salt-purifier and corrosion-inhibitor. Based on the 2000-hour exposure test, the CRs of SS 310 and In 800H in the molten $MgCl_2$-KCl-NaCl salt purified with liquid Mg at 700 °C under the Ar atmosphere are 7.6 ± 1.6 μm/year and 4.9 ± 2.2 μm/year, respectively. **Fig. 12** displays the SEM-EDX analysis of SS 310 in $MgCl_2$-KCl-NaCl mixture at 700 °C for 2000-hour. As can be seen, the corrosion layer of this sample is minor, while little Cr-depletion in the corrosion layer is observed, implying the stainless steel can have good compatibility with purified $MgCl_2$-KCl-NaCl at 700 °C with a proper anti-corrosion strategy.

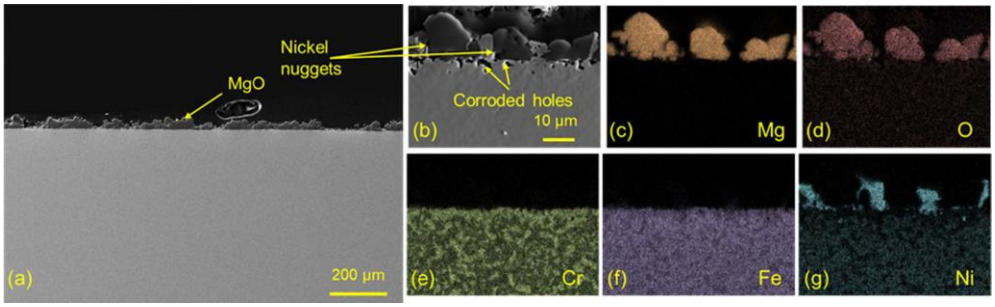

Fig. 12. Cross-section SEM and EDX-mapping images of Sample SS 310-2000h, which is immersed in purified $MgCl_2$-KCl-NaCl salt at 700 °C for 2000 h.

Similarly, in paper III, two cost-effective commercial types of steels, P91 and SS 304, are examined as candidates for structural materials, and controlled corrosion experiments are performed in molten $MgCl_2$-KCl-NaCl salt at 500 °C for 1400 h. As shown in **Fig. 13**, the CRs of P91 samples are <15 μm/year according to the macroscopic analysis on the 1400-hour sample, thereby allowing the use of cost-effective non-nickel steel as structural materials in the cold part (e.g., 500 °C) of the chloride-TES.

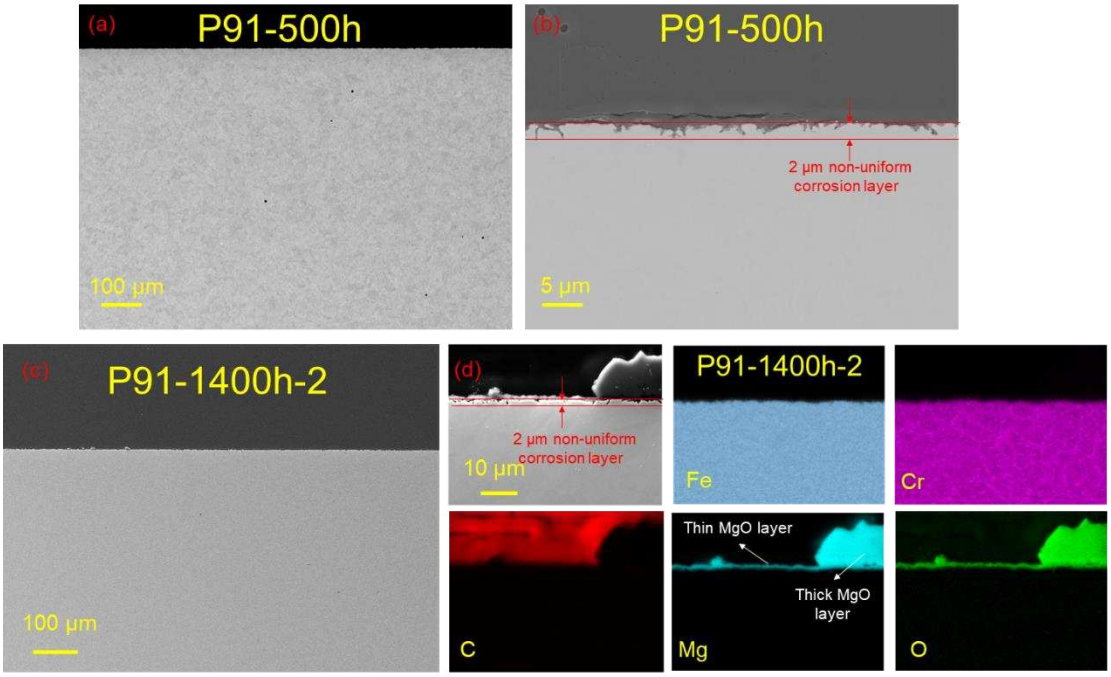

Fig. 13. SEM-EDX images of P91 samples without descaling. (a) and (b) the cross-section of P91 sample immersed in purified $MgCl_2$-KCl-NaCl salt at 500 °C for 500 h with different magnification; (c) the cross-section of P91 sample immersed in purified $MgCl_2$-KCl-NaCl salt at 500 °C for 1400 h; (d) the EDX analysis of P91 sample in (c).

4.2 Discussion

Solving the problem of corrosion of Fe-based alloys (e.g., stainless steel) in chloride salts is the key to breaking the trilemma of high temperature molten chloride salts. This thesis demonstrates that the optimized Mg purification can reduce corrosivity of molten $MgCl_2$-KCl-NaCl salt at 700 °C, thereby expanding the material selection window for chloride-TES, as shown in Paper II and Paper III. In addition, the cost of chloride-TES using Fe-based alloy as the main structural material will be initially estimated. Furthermore, the experience gained in the laboratory can be extended to industrial process design and some research gaps before the application of chloride-TES are suggested in this discussion section.

4.2.1 Cost estimation of chloride-TES

In both paper II and III, the estimation of cost of hot and cold tanks is included. In this section, the cost of chloride-TES will be analysed and discussed comprehensively based on a chloride-TES with 2703 MWh-th heat storage capacity. The NREL model

in Ref. [1] and data available in the literature [1,11,25,49,71] are adopted in this estimation. Because properties of molten salt and costs of materials vary on different literature sources, the maximum and minimum values available will be used for the data sensitivity analysis.

Cost of salt in chloride-TES is influenced by several parameters. Firstly, the unit cost of $MgCl_2$-KCl-NaCl is in the range of 0.22 – 0.7 USD/kg [1,25,49,71]. Secondly, the temperature difference of hot and cold parts (ΔT) varies from 200 °C (500 °C – 700 °C) to 280 °C (420 °C – 700 °C). For a fixed heat storage capacity, the larger temperature difference means the smaller mass and volume which influences the tank cost. In this estimation, heat capacity and density of molten $MgCl_2$-KCl-NaCl salt are 1.12 J/(g °C) and 1.65 g/cm^3, respectively, taken from a review paper published by Villada et al. [11].

Cost of tanks in chloride-TES is influenced by the volume of used salt, maximum allowable stress and cost factor of used alloy at operating temperature. Firstly, the volume of chloride salt can be calculated from the density and mass of molten chloride salt. Secondly, the maximum allowable stress is available in the ASME code, as shown in **Fig. 14**. For the hot tank with operating temperature ≥ 700 °C, the austenitic stainless steel (e.g. TP310HCbN, S31035 and S30432) with affordable cost is recommended. Thirdly, although accurate steel costs are difficult to gather, costs for austenitic stainless steels with similar Ni wt.% are comparable and much lower than Ni-based alloys. Considering the hot tank of nitrate-TES is made of SS347H with maximum allowable stress of about 115 MPa at 565°C, a classic austenitic stainless steel, the F_2 in Eq. 11 can be set in range of 1 – 1.5. When S31035 with maximum allowable stress of about 64 MPa at 700°C is selected as the main structural material of hot tank for chloride-TES, the F_3 in Eq. 12 is equal to 1.8. For the cold tank with operating temperature < 500 °C, the ferritic-martensitic steel (e.g. P91) with low cost and high allowable stress is recommended with the F_2 of 1.5 and F_3 of 0.82 compared with carbon steel (e.g. ASTM A 516 70 in Table 1) in nitrate-TES.

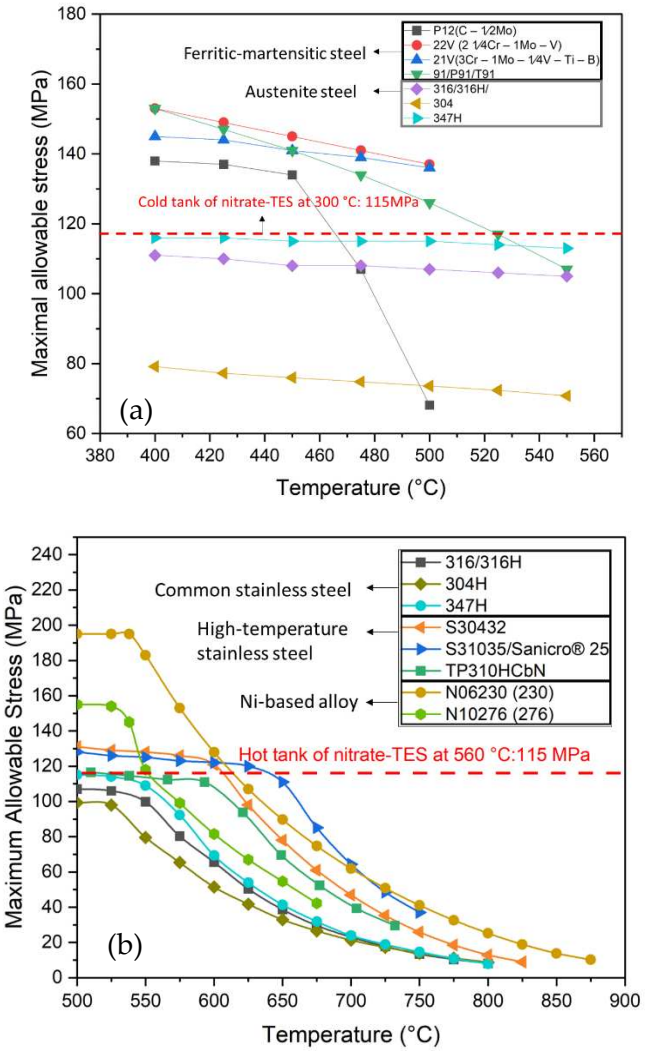

Fig. 14. Maximum allowable stress of some types of steel, all from ASME Boiler And Pressure Vessel Code [23] except S31035 which is available on the datasheet [72]. (a) Some candidates for cold tank. (b) Some candidates for hot tank.

The costs of nitrate-TES, chloride-TES with Ha 230 as hot tank (chloride-TES-Ha 230), and chloride-TES with stainless steel (Chloride-TES-SS) are displayed in the Fig. 15. Breakdown of costs with different factors is listed in Table 4 and Table 5, which show the maximum and minimum cost of chloride-TES based on Fe-based alloy as the main structural materials, respectively. According to the estimation, when Fe-based alloy is used as the main structural material of chloride-TES, the chloride-TES cost would be comparable to nitrate-TES. In addition, this estimation set a consistent heat storage capacity of chloride-TES with nitrate-TES (2703 MWh-th). However, for a commercial CSP with a fixed electricity-generation power of 100 MW, 2703 MWh thermal energy stored in nitrate-TES realizes 10 hours of electricity generation with ~40%

thermoelectrical conversion efficiency. For a Gen-3 CSP with the equivalent power of 100 MW_{-el} and 10-hour electricity generation, the heat storage capacity will be significantly reduced by 37.5 % to ~1690 MWh_{-th}, due to the thermoelectrical conversion efficiency increases from ~40% to ~55% with the operating temperature of 700 °C, combined with advanced power cycle. In other words, the total cost of chloride-TES can be further reduced significantly when the electrical output of CSP is set as a benchmark.

There are some shortcomings in this rough estimation. Firstly, this estimation is based on the cost of 2015 and does not take inflation into account. Secondly, it is difficult to obtain the exact costs of the main materials such as salt and steel, and their costs may vary considerably at different locations, in addition to inflation. Thirdly, the temperature difference may need to be adjusted to match the used power cycle (e.g. sCO_2 power cycle). Despite these limitations, this estimation predicts a competitive scenario for chloride-TES with Fe-based alloy. The use of Fe-based alloys in chloride-TES must be based on a precise corrosion control system. The cost estimation could be improved by considering the costs of the corrosion control system [49], further contact with steel supplier, and detailed design of mechanical structure characteristic for chloride-TES at high operating temperature.

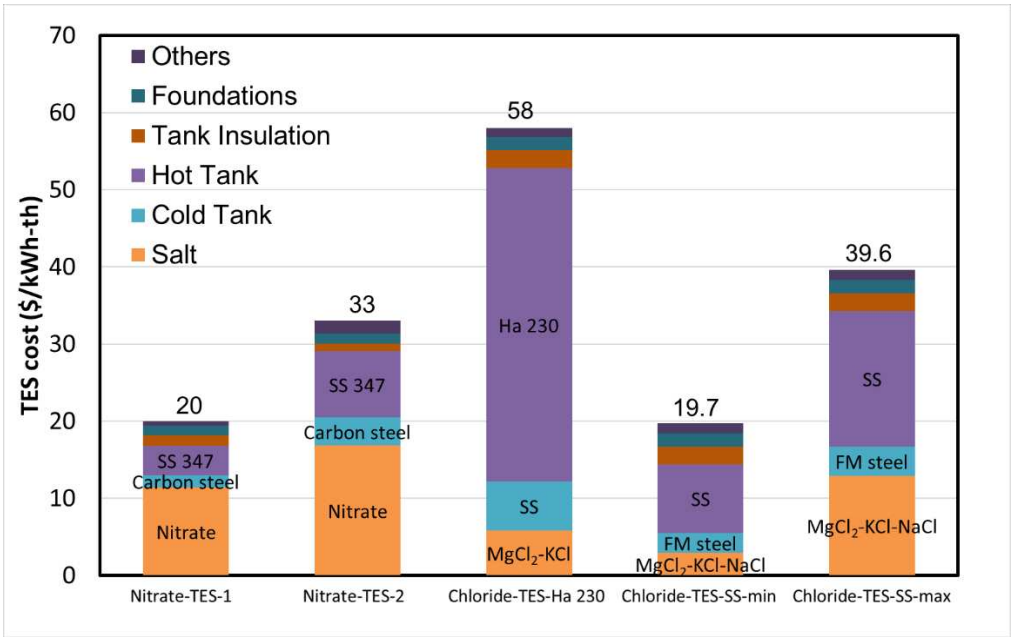

Fig. 15. A comparison of cost of commercial nitrate-TES with estimated chloride-TES. Costs of nitrate-TES and chloride-TES-Ha 230 are available in [1], while the costs of chloride-TES are estimated based on the same model of chloride-TES-Ha 230.

Table 4. Cost estimation of chloride-TES with 2703 MWh_{-th} - Maximum value. The heat storage capacity is consistent with nitrate-TES in Table 1.

	Material	Cost USD thousands	TES cost USD/kWh-t	Percentage
Hot tank	Austenitic steel	47581	17.60	44.5
Cold tank	Ferritic-martensitic steel	10269	3.80	9.6
Salt inventory	$MgCl_2$-KCl-NaCl	34934	12.92	32.6
Structural steel	Consisting with data in Ref. [1]	1117	0.41	1.0
Tank insulation		6243	2.31	5.8
Electrical		1161	0.43	1.1
Foundations		5113	1.89	4.8
Site work		581	0.21	0.5
Total		106999	39.6	100

Parameters:
TES capacity: 2703 MWh_{-th}; Salt cost: 0.7 USD/kg; Temperature difference: 200°C; Salt mass: 49905 tons.
F_1 of hot tank: 1.75; F_2 of hot tank: 1.5; F_3 of hot tank: 1.8.
F_1 of cold tank: 1.75; F_2 of cold tank: 1.5; F_3 of cold tank: 0.82.

Table 5. Cost estimation of chloride-TES with 2703 MWh_{-th} - Minimum value. The heat storage capacity is consistent with nitrate-TES in Table 1.

	Material	Cost USD thousands	TES cost USD/kWh-t	Percentage
Hot tank	Austenitic steel	24026	8.89	45.2
Cold tank	Ferritic-martensitic steel	7122	2.63	13.4
Salt inventory	$MgCl_2$-KCl-NaCl	7842	2.90	14.7
Structural steel		1117	0.41	2.1

Tank insulation	Consisting with data in Ref. [1]	6243	2.31	11.7
Electrical		1161	0.43	2.2
Foundations		5113	1.89	9.6
Site work		581	0.21	1.1
Total		53206	19.7	100

Parameters:
TES capacity: 2703 MWh-th; Salt cost: 0.22 USD/kg; Temperature difference: 300°C; Salt mass: 35647 tons.
F1 of hot tank: 1.33; F2 of hot tank: 1; F3 of hot tank: 1.8.
F1 of cold tank: 1.33; F2 of cold tank: 1.5; F3 of cold tank: 0.82.

4.2.2 Industrial process design of chloride-TES

In both paper II and paper III, it is clearly demonstrated that the CRs of selected Fe-based alloy in molten chloride salt can reach the ambitious target of 15 μm/year by thousand-hour isothermal exposure tests at 500 °C and 700 °C. The experimental design points to the final industrial process design, as shown in **Fig. 16**.

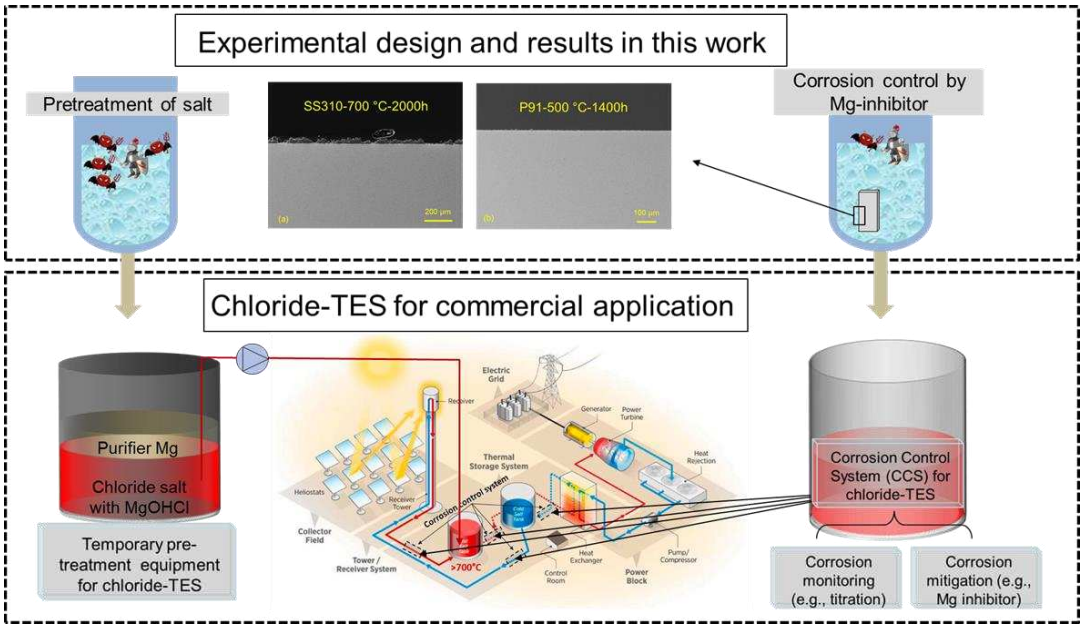

Fig. 16. Industrial procedure of chloride-TES for commercial application in CSP designed based on the experimental design.

First of all, the pre-treatment of molten chloride salt in a separated vessel is necessary which is comparable to initial melting of salt in nitrate-TES [22]. In addition to salt melting, excess purifier (e.g., liquid Mg metal) is recommended to add in the molten

chloride salt. Due to the density difference and poor affinity between liquid metal and molten chloride salt, liquid metal and molten salt can naturally stratify, consisting with the observation in liquid metal batteries [73]. In view of the large amount of corrosive impurities (e.g., MgOHCl and HCl) released by this process, the pre-treatment vessel can be made of a material with non-metallic in smaller scale than the tanks in TES. For high volume rate molten salt pre-treatment, consisting with the scale of up to ~50 000 tons shown in Table 4, a continuous process has been designed and been patented. More details can be found in [74].

Secondly, during the operating of chloride-TES, the corrosion monitoring, especially corrosivity measurement of molten salt, is significant. For monitoring MgOHCl, a direct titration method is developed and calibrated as shown in paper I. With this method, the measurement accuracy for corrosive MgOHCl in molten chloride improved by one to two order of magnitude compared to method published by NREL [55]. Before and after the immersion tests shown in paper II and III, the MgOHCl concentration can be measured in ten-of-ppm level. In addition, as shown in paper I, the CV measurement of MgOHCl is calibrated by the direct titration. It shows that even at the ten-of-ppm level, there is still a linear relationship between the current density of peak B in CV and the concentration of MgOHCl. However, the large difference of diffusion coefficients of MgOHCl calculated in paper I and other literature suggests that the CV tests in paper I may be subject to large errors. The error is probably due to passivation of the electrode. For long-duration and robust signal output, the electrodes need to be optimised in future work.

Thirdly, during the operating, the corrosion control system (CCS) with corrosion mitigation will be a necessary component. In the paper II and paper III, the excessive Mg metal plays a role of corrosion inhibitor. In practice, the Mg inhibitor existing in chloride-TES is not actionable. Mg has the melting point of ~650 °C, which means that Mg in hot part of chloride-TES is liquid while in cold part it is solid. In addition, the negative effect of liquid Mg on nickel-containing structural material (such as In 800H in paper II) has been observed during the immersion test and verified by other references [41,67,75], indicating that the liquid Mg as the corrosion inhibitor in the chloride-TES cannot have direct contact with the Ni-containing alloys. In contrast, the electrolysis method used in paper I at 500 °C is applicable for removing a small amount of MgOHCl during operating for corrosion control.

4.2.3 Future work

In the future, the technology readiness level (TRL) of chloride-TES technology at DLR will be attempted to upgrade from 3-4 to 5-6, i.e., the kg-level loop with corrosion control system will be built. Some future work is suggested as follows:

- A more stable and accurate in-situ MgOHCl measurement based on CV is suggested to be developed to solve the problem of electrode passivation.
- A large-scale salt purification technology is suggested to be built, tested, and optimised to reach the acceptable corrosive MgOHCl concentration in molten chloride salt before operating.
- The corrosion control system would be further investigated under a dynamic condition in the loop to achieve the acceptable of CRs of the selected Fe-based alloys.
- Some corrosion-sensitive specimens from the material processing (e.g., welding joints, 3D printed components) can be tested under corrosion control in molten chloride salt.

5 Summary and outlook

Chloride-TES is a promising molten salt TES technology developed for next-generation (Gen 3) CSP plant. With molten $MgCl_2$-KCl-NaCl salt as heat storage medium and heat transfer fluid, operating temperature of TES can be increased to ≥ 700 °C, significantly higher than commercial nitrate-TES. However, the corrosion issues hinder the application of molten chloride salt in two aspects.

- Without corrosion mitigation strategy, no Fe-Cr-Ni alloy can meet the corrosion rate target of 15 μm/year proposed for 30-year lifetime of structural material.
- With insufficient corrosion mitigation strategies, the Fe-based alloys (e.g., stainless steel, ferritic-martensitic steel) cannot meet the corrosion rate. The expensive nickel-based alloys (e.g., Haynes 230, C-276) may have to be selected as the structural material of the hot tank, resulting in a not affordable material cost for chloride-TES.

Main contributions of this work are summarized as follows:

- The main corrosive impurity MgOHCl is measured down to the tens of ppm O level by the a newly developed direct titration method. The error analysis of such titration shows that when the MgOHCl concentration in about 500 mg salt samples is 36 ppm O, the average error is +6.62 ppm O and the average standard deviation is 4.35 ppm O. The method of titration is one to two orders of magnitude more accuracy than other MgOHCl measurement methods [52,55].
- The obtained CV data (i.e., peak current density) for 500–700°C shows good linearity with the data on direct titration (i.e., MgOHCl concentration) in the range from 39 to 4211 ppm O. The slope of the concentration of MgOHCl vs. the peak current density in CV was 7.2 ± 2 (ppm O)/(mA/cm^2) in the temperature range of 500–700°C.
- This work experimentally proves that the CRs of selected Fe-based alloys in molten chloride salt can reach the target of 15 μm/year by thousand-hour isothermal exposure tests at 500 °C and 700 °C, when the salt is properly purified with Mg.

- According to the titration of the salt in the immersion tests, the acceptable concentration of MgOHCl in molten chloride salt is ~200 ppm O at 700 °C.
- Based on the corrosion results and the maximum allowable stress at high temperatures, a preliminary selection of structural materials (i.e., alloys) for the tanks of chloride-TES is completed.
- When austenitic stainless steel and ferritic-martensitic steel can be used as the primary structural materials of the hot and cold tanks, respectively, the cost of chloride-TES will be comparable to that of commercial nitrate-TES (20-40 USD/kWh$_{th}$ vs. 20-33 USD/kWh$_{th}$).

Generally, in this work, the trilemma of material selection for chloride-TES is broken by a proper corrosion control strategy. A cost-effective scenario of chloride-TES is described with the Fe-based alloys as the main structural materials. Indicators of molten chloride salt corrosion to Fe-based alloys, including the source and product of corrosion, are quantified and accurately analysed. In the isothermal static state, sufficient corrosion control data has been collected to be well prepared for the next scaling-up step.

6 References

1 Mehos, M. *et al.* Concentrating solar power Gen3 demonstration roadmap. (National Renewable Energy Lab.(NREL), Golden, CO (United States), United States, 2017). https://doi.org/10.2172/1338899

2 Ding, W. & Bauer, T. Progress in Research and Development of Molten Chloride Salt Technology for Next Generation Concentrated Solar Power Plants. *Engineering* (2021). https://doi.org/10.1016/j.eng.2020.06.027

3 Bauer, T., Odenthal, C. & Bonk, A. Molten Salt Storage for Power Generation. *Chemie Ingenieur Technik* **93**, 534-546 (2021). https://doi.org/10.1002/cite.202000137

4 Villada, C., Bonk, A., Bauer, T. & Bolívar, F. High-temperature stability of nitrate/nitrite molten salt mixtures under different atmospheres. *Applied Energy* **226**, 107-115 (2018). https://doi.org/10.1016/j.apenergy.2018.05.101

5 Bonk, A. *et al.* Advanced heat transfer fluids for direct molten salt line-focusing CSP plants. **67**, 69-87 (2018). https://doi.org/10.1016/j.pecs.2018.02.002

6 Zhao, Y. Molten Chloride Thermophysical Properties, Chemical Optimization, and Purification. (National Renewable Energy Lab.(NREL), Golden, CO (United States), 2020). https://www.osti.gov/biblio/1734652

7 Novotny, V., Basta, V., Smola, P. & Spale, J. Review of Carnot Battery Technology Commercial Development. *Energies* **15**, 647 (2022). 10.3390/en15020647

8 Pint, B. Progression to Compatibility Evaluations in Flowing Molten Salts. (Office of Scientific and Technical Information (OSTI), 2020). https://dx.doi.org/10.2172/1649281

9 Duan, L., Petroski, R., Wood, L. & Caldeira, K. Stylized least-cost analysis of flexible nuclear power in deeply decarbonized electricity systems considering wind and solar resources worldwide. *Nature Energy* (2022). 10.1038/s41560-022-00979-x

10 Ambrosek, J. W. *Molten chloride salts for heat transfer in nuclear systems* Ph.D. thesis, University of Wisconsin - Madison, (2011).

https://www.proquest.com/docview/885007950?parentSessionId=5Ny2J3Dfp0LfvlEPUHP6b3HyR2nnutVr4yPpB7p7OEY%3D

11 Villada, C., Ding, W., Bonk, A. & Bauer, T. Engineering molten MgCl2–KCl–NaCl salt for high-temperature thermal energy storage: Review on salt properties and corrosion control strategies. *Solar Energy Materials and Solar Cells* **232**, 111344 (2021). https://doi.org/10.1016/j.solmat.2021.111344

12 Ding, W., Bonk, A. & Bauer, T. Corrosion behavior of metallic alloys in molten chloride salts for thermal energy storage in concentrated solar power plants: A review. *Frontiers of Chemical Science Engineering* **12**, 564-576 (2018). https://doi.org/10.1007/s11705-018-1720-0

13 Ding, W. *et al.* Hot corrosion behavior of commercial alloys in thermal energy storage material of molten MgCl2/KCl/NaCl under inert atmosphere. *Solar Energy Materials and Solar Cells* **184**, 22-30 (2018). https://doi.org/10.1016/j.solmat.2018.04.025

14 Garcia-Diaz, B. L. *et al.* High temperature electrochemical engineering and clean energy systems. *Journal of the South Carolina Academy of Science* **14**, 4 (2016). https://scholarcommons.sc.edu/jscas/vol14/iss1/4

15 Raseman, C. J., Susskind, H., Farber, G., McNulty, W. E. & Salzano, F. J. ENGINEERING EXPERIENCE AT BROOKHAVEN NATIONAL LABORATORY IN HANDLING FUSED CHLORIDE SALTS. (Office of Scientific and Technical Information (OSTI), 1960). https://doi.org/10.2172/4068644

16 Susskind, H. *et al.* Corrosion studies for a fused salt-liquid metal extraction process for the liquid metal fuel reactor. (Brookhaven National Lab., Upton, NY, 1960). https://doi.org/10.2172/4023508

17 Ding, W. *et al.* Compatibility of 3D-Printed Oxide Ceramics with Molten Chloride Salts for High-Temperature Thermal Energy Storage in Next-Generation CSP Plants. **14**, 2599 (2021). https://doi.org/10.3390/en14092599

18 International Renewable Energy Agency: Abu Dhabi, U. IRENA Renewable Power Generation Costs in 2020. (2020).

19 Denholm, P., Clark, K. & O'Connell, M. On the Path to SunShot. Emerging Issues and Challenges in Integrating High Levels of Solar into the Electrical Generation and Transmission System. (Office of Scientific and Technical Information (OSTI), 2016). https://doi.org/10.2172/1253978

20 *China now has 30 CSP projects with thermal energy storage underway*, <https://www.solarpaces.org/china-now-has-30-csp-projects-with-thermal-energy-storage-underway/> (2022).

21 Geyer, M., Trieb, F. & Giuliano, S. Repurposing of existing coal-fired power plants into Thermal Storage Plants for renewable power in Chile. (2020).

22 Mehos, M. *et al.* Concentrating solar power best practices study. (National Renewable Energy Lab.(NREL), Golden, CO (United States), 2020). https://doi.org/10.2172/1665767

23 ASME. ASME Boiler And Pressure Vessel Code 2010. New York (2010).

24 Turchi, C. Concentrating solar power: current cost and future directions. *Oral Present* (2017).

25 Turchi, C. S., Vidal, J. & Bauer, M. Molten salt power towers operating at 600–650 C: Salt selection and cost benefits. *Solar Energy* **164**, 38-46 (2018). https://doi.org/10.1016/j.solener.2018.01.063

26 Gilardi, T. *et al.*Influence of material choice on cost estimation of some key components of the sulfur iodine thermochemical process. in *Proc. of 16th World Hydrogen Energy Conference (WHEC).* 13-16.

27 Villada, C., Ding, W., Bonk, A. & Bauer, T. Simulation-Assisted Determination of the Minimum Melting Temperature Composition of MgCl2–KCl–NaCl Salt Mixture for Next-Generation Molten Salt Thermal Energy Storage. *Frontiers in Energy Research* **10** (2022). https://doi.org/10.3389/fenrg.2022.809663

28 Mohan, G., Venkataraman, M., Gomez-Vidal, J. & Coventry, J. Assessment of a novel ternary eutectic chloride salt for next generation high-temperature sensible heat storage. *Energy Conversion and Management* **167**, 156-164 (2018). https://doi.org/10.1016/j.enconman.2018.04.100

29 Sun, H., Wang, J., Li, Z., Zhang, P. & Su, X. Corrosion behavior of 316SS and Ni-based alloys in a ternary NaCl-KCl-MgCl2 molten salt. *Solar Energy* **171**, 320-329 (2018). https://doi.org/10.1016/j.solener.2018.06.094

30 Sun, H., Zhang, P. & Wang, J. J. C. s. Effects of alloying elements on the corrosion behavior of Ni-based alloys in molten NaCl-KCl-MgCl2 salt at different temperatures. **143**, 187-199 (2018). https://doi.org/10.1016/j.corsci.2018.08.021

31 Ding, W. *et al.* Molten chloride salts for next generation concentrated solar power plants: Mitigation strategies against corrosion of structural materials. *Solar Energy Materials and Solar Cells* **193**, 298-313 (2019). https://doi.org/10.1016/j.solmat.2018.12.020

32 Kurley, J. M. *et al.* Enabling chloride salts for thermal energy storage: implications of salt purity. *RSC Advances* **9**, 25602-25608 (2019). https://doi.org/10.1039/C9RA03133B

33 Guo, L., Liu, Q., Yin, H., Pan, T. J. & Tang, Z. Excellent corrosion resistance of 316 stainless steel in purified NaCl-MgCl2 eutectic salt at high temperature. *Corrosion Science* **166**, 108473 (2020). https://doi.org/10.1016/j.corsci.2020.108473

34 Liu, Q. *et al.* Ni-Mo-Cr alloy corrosion in molten NaCl-KCl-MgCl2 salt and vapour. *Corrosion Science* **180**, 109183 (2021). https://doi.org/10.1016/j.corsci.2020.109183

35 Lai, G. Y. *High-temperature corrosion and materials applications*. (ASM international, 2007).

36 Mortazavi, A. *et al.* High-temperature corrosion of a nickel-based alloy in a molten chloride environment – The effect of thermal and chemical purifications. *Solar Energy Materials and Solar Cells* **236**, 111542 (2022). https://doi.org/10.1016/j.solmat.2021.111542

37 Choi, S. *et al.* Effect of Mg dissolution on cyclic voltammetry and open circuit potentiometry of molten MgCl2–KCl–NaCl candidate heat transfer fluid for concentrating solar power. *Solar Energy Materials and Solar Cells* **202**, 110087 (2019). https://doi.org/10.1016/j.solmat.2019.110087

38 Zhang, M., Ge, J., Yin, T. & Zhang, J. Redox potential measurements of Cr (II)/Cr Ni (II)/Ni and Mg (II)/Mg in molten MgCl2–KCl–NaCl mixture. *Journal of The Electrochemical Society* **167**, 116505 (2020). http://dx.doi.org/10.1149/1945-7111/aba15a

39 Grégoire, B., Oskay, C., Meißner, T. & Galetz, M. Corrosion mechanisms of ferritic-martensitic P91 steel and Inconel 600 nickel-based alloy in molten chlorides. Part I: NaCl–KCl binary system. *Solar Energy Materials and Solar Cells* **215**, 110659 (2020). https://doi.org/10.1016/j.solmat.2020.110659

40 Grégoire, B., Oskay, C., Meißner, T. & Galetz, M. Corrosion mechanisms of ferritic-martensitic P91 steel and Inconel 600 nickel-based alloy in molten chlorides. Part II: NaCl-KCl-MgCl2 ternary system. *Solar Energy Materials and Solar Cells* **216**, 110675 (2020). https://doi.org/10.1016/j.solmat.2020.110675

41 D'Souza, B., Zhuo, W., Yang, Q., Leong, A. & Zhang, J. Impurity driven corrosion behavior of HAYNES® 230® alloy in molten chloride Salt. *Corrosion Science* **187**, 109483 (2021). https://doi.org/10.1016/j.corsci.2021.109483

42 Lu, P., Liu, Q., Bao, H., Pan, T. J. & Tang, Z. Effect of FeCl3 in NaCl-MgCl2 molten salts on the corrosion behavior of 316 stainless steel at 600 °C. *Corrosion Science* **212**, 110961 (2023). https://doi.org/10.1016/j.corsci.2023.110961

43 Li, X. *et al.* Thermodynamic and kinetic corrosion behavior of alloys in molten MgCl2–NaCl eutectic: FPMD simulations and electrochemical technologies. *Solar Energy Materials and Solar Cells* **238**, 111624 (2022). https://doi.org/10.1016/j.solmat.2022.111624

44 Ding, W., Yang, F., Bonk, A. & Bauer, T. Molten chloride salts for high-temperature thermal energy storage: Continuous electrolytic salt purification with two Mg-electrodes and alternating voltage for corrosion control. *Solar Energy Materials and Solar Cells* **223**, 110979 (2021). https://doi.org/10.1016/j.solmat.2021.110979

45 Ding, W., Bonk, A., Gussone, J. & Bauer, T. Electrochemical measurement of corrosive impurities in molten chlorides for thermal energy storage. *Journal of Energy Storage* **15**, 408-414 (2018). https://doi.org/10.1016/j.est.2017.12.007

46 Zhao, Y. & Vidal, J. Potential scalability of a cost-effective purification method for MgCl2-Containing salts for next-generation concentrating solar power technologies. *Solar Energy Materials and Solar Cells* **215**, 110663 (2020). https://doi.org/10.1016/j.solmat.2020.110663

47 ASTM-G1-03. Standard Practice for Preparing, Cleaning, and Evaluating Corrosion Test Specimens. (1999).

48 Zhao, Y., Klammer, N. & Vidal, J. Purification strategy and effect of impurities on corrosivity of dehydrated carnallite for thermal solar applications. *RSC Advances* **9**, 41664-41671 (2019). https://doi.org/10.1039/C9RA09352D

49 Turchi, C. *et al.* CSP Gen3: Liquid-Phase Pathway to SunShot. (National Renewable Energy Lab.(NREL), Golden, CO (United States), 2021). https://doi.org/10.2172/1807668

50 Kashani-Nejad, S. *Oxides in the dehydration of magnesium chloride hexahydrate* Doctor of Philosophy thesis, McGill University, (2005). https://escholarship.mcgill.ca/concern/theses/ws859g01q

51 Kipouros, G. J. & Sadoway, D. R. A thermochemical analysis of the production of anhydrous MgCl2. *Journal of Light Metals* **1**, 111-117 (2001). https://doi.org/10.1016/S1471-5317(01)00004-9

52 Ding, W., Bonk, A., Gussone, J. & Bauer, T. Cyclic voltammetry for monitoring corrosive impurities in molten chlorides for thermal energy storage. *Energy Procedia* **135**, 82-91 (2017). https://doi.org/10.1016/j.egypro.2017.09.489

53 Skar, R. A. *Chemical and electrochemical characterisation of oxide/hydroxide impurities in the electrolyte for magnesium production* Ph.D thesis, Norwegian University of Science and Technology Fakultet for naturvitenskap og teknologi, (2001). http://hdl.handle.net/11250/244438

54 Eom, H.-C., Yoon, H.-S., Park, H.-K. & Kim, C.-J. Dehydration characteristics of Magnesium Chloride Hydrate. *Journal of the Korean Institute of Resources Recycling* **16**, 8-12 (2007).

55 Klammer, N., Engtrakul, C., Zhao, Y., Wu, Y. & Vidal, J. Method To Determine MgO and MgOHCl in Chloride Molten Salts. *Journal of Analytical chemistry* **92**, 3598-3604 (2020). https://10.1021/acs.analchem.9b04301

56 Kashani-Nejad, S., Ng, K.-W. & Harris, R. MgOHCl thermal decomposition kinetics. *Metallurgical Materials Transactions B* **36**, 153-157 (2005). https://doi.org/10.1007/s11663-005-0015-2

57 Guo, J., Hoyt, N. & Williamson, M. Multielectrode array sensors to enable long-duration corrosion monitoring and control of concentrating solar power systems. *Journal of Electroanalytical Chemistry* **884**, 115064 (2021). https://doi.org/10.1016/j.jelechem.2021.115064

58 Grégoire, B., Oskay, C., Meißner, T. M. & Galetz, M. C. Corrosion performance of slurry aluminide coatings in molten NaCl–KCl. *Solar Energy Materials and Solar Cells* **223**, 110974 (2021). https://doi.org/10.1016/j.solmat.2021.110974

59 Raiman, S. S., Mayes, R. T., Kurley, J. M., Parrish, R. & Vogli, E. Amorphous and partially-amorphous metal coatings for corrosion resistance in molten chloride salt. *Solar Energy Materials and Solar Cells* **201**, 110028 (2019). https://doi.org/10.1016/j.solmat.2019.110028

60 Abu Kassim, S., Thor, J. A., Abu Seman, A. & Abdullah, T. K. High temperature corrosion of Hastelloy C22 in molten alkali salts: The effect of pre-oxidation treatment. *Corrosion Science* **173**, 108761 (2020). https://doi.org/10.1016/j.corsci.2020.108761

61 Ding, W., Shi, Y., Kessel, F., Koch, D. & Bauer, T. Characterization of corrosion resistance of C/C–SiC composite in molten chloride mixture MgCl2/NaCl/KCl at 700 °C. *npj Materials Degradation* **3**, 42 (2019). https://doi.org/10.1038/s41529-019-0104-3

62 Gage, S. H. *et al.* Technical and economic feasibility of molten chloride salt thermal energy storage systems. *Solar Energy Materials and Solar Cells* **226**, 111099 (2021). https://doi.org/10.1016/j.solmat.2021.111099

63 Ding, W., Gomez-Vidal, J., Bonk, A. & Bauer, T. Molten chloride salts for next generation CSP plants: Electrolytical salt purification for reducing corrosive impurity level. *Solar Energy Materials and Solar Cells* **199**, 8-15 (2019). https://doi.org/10.1016/j.solmat.2019.04.021

64 Rippy, K., Witteman, L., Monestarial, A., Taylor, P. & Vidal, J. in *SolarPACES* (Online, 2021).

65 Sun, H., Wang, J.-Q., Tang, Z., Liu, Y. & Wang, C. Assessment of effects of Mg treatment on corrosivity of molten NaCl-KCl-MgCl2 salt with Raman and Infrared spectra. *Corrosion Science* **164**, 108350 (2020). https://doi.org/10.1016/j.corsci.2019.108350

66 Ren, S. *et al.* Corrosion behavior of carburized 316 stainless steel in molten chloride salts. *Solar Energy* **223**, 1-10 (2021). https://doi.org/10.1016/j.solener.2021.05.057

67 Hanson, K. *et al.* Effect of excess Mg to control corrosion in molten MgCl2 and KCl eutectic salt mixture. *Corrosion Science* **194**, 109914 (2022). https://doi.org/10.1016/j.corsci.2021.109914

68 Mayes, R. T. *et al.* Purification of Chloride Salts for Concentrated Solar Applications. (Office of Scientific and Technical Information (OSTI), 2018). https://dx.doi.org/10.2172/1506795

69 Maricle, D. L. & Hume, D. N. A new method for preparing hydroxide-free alkali chloride melts. (Massachusetts Inst. of Tech., Cambridge. Lab. for Nuclear Science, United States, 1959). https://www.osti.gov/biblio/4197980

70 Tomkins, R. P. T., Bansal, N. P., BANSAL, N. P. & SHINMEI, M. *Gases in molten salts*. Vol. 45/46 (Elsevier, 1991).

71 Ding, W., Bonk, A. & Bauer, T.Molten chloride salts for next generation CSP plants: Selection of promising chloride salts & study on corrosion of alloys in molten chloride salts. in *AIP Conference Proceedings.* 200014 (AIP Publishing LLC).

72 Alleima. *Sanicro® 25 Tube and pipe, seamless*, <https://www.alleima.com/en/technical-center/material-datasheets/tube-and-pipe-seamless/sanicro-25/> (2022).

73 Bradwell, D. J., Kim, H., Sirk, A. H. C. & Sadoway, D. R. Magnesium–Antimony Liquid Metal Battery for Stationary Energy Storage. *Journal of the American Chemical Society* **134**, 1895-1897 (2012). https://doi.org/10.1021/ja209759s

74 Ding, W., Gong, Q. & Bauer, T. Kontinuierliches Reinigungssystem für Halogensalze mit Mg-Additiv. Germany patent DE 10 2021 131 250.7 (2021).

75 Pint, B. A. *et al.* Re-establishing the paradigm for evaluating halide salt compatibility to study commercial chloride salts at 600°C–800°C. *Materials and Corrosion* **70**, 1439-1449 (2019). https://doi.org/10.1002/maco.201810638